IMAGERY

VISIBLE/INFRARED IMAGER/RADIOMETER SUITE ALGORITHM THEORETICAL BASIS DOCUMENT

Version 5: March 2002

Kenneth A. Jensen
Keith Hutchison
Richard Julian

Igor Appel (Phase I)
North Larsen (Phase I)
Wenli Yang (Phase I)
Duane Apling (Phase I)

RAYTHEON SYSTEMS COMPANY
Information Technology and Scientific Services
4400 Forbes Boulevard
Lanham, MD 20706

SBRS Document #: Y2466

EDRs: IMAGERY

Doc No: Y2466

Version: 5

Revision: 0

	Function	Name	Signature	Date
PREPARED BY	EDR DEVELOPER	K. JENSEN		
APPROVED BY	IMAGERY IPT LEAD	K. JENSEN		
APPROVED BY	REVIEWER	P. KEALY		
APPROVED BY	CHIEF SCIENTIST	S. MILLER		
RELEASED BY	ALGORITHM IPT LEAD	P. KEALY		

TABLE OF CONTENTS

Page

LIST OF FIGURES v

LIST OF TABLES viii

GLOSSARY OF ACRONYMS x

ABSTRACT xv

1.0 INTRODUCTION 1
- 1.1 PURPOSE 1
- 1.2 SCOPE 1
- 1.3 VIIRS DOCUMENTS 3
- 1.4 REVISIONS 4

2.0 EXPERIMENT OVERVIEW 7
- 2.1 EDR DEFINITION 7
- 2.2 EXPLICIT IMAGERY REQUIREMENTS 7
  - 2.2.1 Change in Specification of the Daytime Visible Imagery Band (I1) 9
  - 2.2.2 Operational Benefits 11
- 2.3 NEAR CONSTANT CONTRAST (NCC) VISIBLE IMAGERY 11
- 2.4 APPLICATION-RELATED REQUIREMENTS 12
  - 2.4.1 Requirements for Cloud Cover 12
  - 2.4.2 Requirements for Cloud Type: 13
  - 2.4.3 Operational Objectives of Manually-Generated Cloud Data 15
    - 2.4.3.1 Introduction 15
    - 2.4.3.2 Weakness in the Current QC System 15
    - 2.4.3.3 Manually-Generated Products During the NPOESS Era 16
  - 2.4.4 Requirements for Ice Edge Location 18
  - 2.4.5 Requirements for Ice Concentration 19
  - 2.4.6 Operational Objectives of Sea Ice Data 20
- 2.5 INSTRUMENT CHARACTERISTICS 22
  - 2.5.1 Daytime/Nighttime Visible Band (DNB) 24
  - 2.5.2 VIIRS Imagery Band Selection Process 25
  - 2.5.3 Daytime Visible Band (DV) 26
  - 2.5.4 Long-Wave Infrared Band (LWIR) 27

2.5.5 Mid-Wave Infrared Band (MWIR) 28
2.5.6 Imagery Assist Bands 29
2.6 RETRIEVAL STRATEGY 30
2.6.1 Explicit Imagery 30
2.6.2 Top-of-Atmosphere Radiances 30
2.6.2 Top-of-Atmosphere Reflectances 31
2.6.3 Equivalent Blackbody Temperatures 31
2.6.4 Near Constant Contrast (NCC) Visible Imagery 31
2.6.5 Manually-Generated Cloud Data 31
2.6.6 Sea Ice Data 31
3.0 ALGORITHM DESCRIPTION 33
3.1 OVERVIEW 33
3.2 EXPLICIT IMAGERY PRODUCTION 33
3.2.1 Processing Outline 33
3.2.2 Algorithm Input 33
3.2.2.1 VIIRS Data 33
3.2.2.2 Non-VIIRS Data 33
3.2.3 Theoretical Description 34
3.2.4 Archived Algorithm Output 34
3.2.5 Performance of Explicit Imagery 34
3.2.5.1 Daytime/Nighttime Visible Band 37
3.2.5.2 Other Imagery Bands 41
3.3 NCC VISIBLE IMAGERY PRODUCTION 42
3.3.1 Processing Outline 42
3.3.1.1 Baseline Approach - Gain Management Algorithm 42
3.3.1.2 Enhanced Algorithm Approach - Atmospheric Correction 45
3.3.2 Algorithm Input 46
3.3.2.1 VIIRS Data 46
3.3.2.2 Non-VIIRS Data 46
3.3.3 Theoretical Description 46
3.3.3.1 Physics of the Problem 46
3.3.3.2 Mathematical Description of the Algorithm 48
3.3.4 Archived Algorithm Output 49
3.3.5 Performance of NCC Visible Imagery 49
3.3.5.1 Baseline Algorithm 49
3.3.5.2 Atmospheric Correction Enhancement 50
3.3.6 Initialization and Validation 52
3.3.6.1 Initialization 52
3.3.6.2 Pre-Launch Characterization 52

3.3.6.3 Validation 52
3.3.7 Practical Considerations 52
3.3.7.1 Numerical Computation Considerations 52
3.3.7.2 Programming and Procedural Considerations 53
3.3.7.3 Configuration of Retrievals 53
3.3.7.4 Quality Assessment and Diagnostics 53
3.3.8 Algorithm Watch List 53
3.4 MANUAL CLOUD ANALYSIS PRODUCT DESCRIPTION 53
3.4.1 Processing Outline 53
3.4.2 Algorithm Input 54
3.4.2.1 VIIRS Data 55
3.4.2.2 Non-VIIRS Data 55
3.4.3 Theoretical Description 55
3.4.3.1 Physics of the Problem 55
3.4.3.2 Image Processes to Enhance Cloud Detection in Multispectral Imagery 58
3.4.3.3 Mathematical Description of the Algorithm 63
3.4.3.4 VIIRS Imagery and Imagery Assist Color Composites 64
3.4.3.5 VIIRS Cloud Mask for Imagery 74
3.4.4 Performance of Manually-Generated Cloud Data 78
3.4.4.1 Cloud Cover 80
3.4.4.2. Cloud Type 82
3.4.5 Initialization and Validation 84
3.5 SEA ICE DATA PRODUCT DESCRIPTION 85
3.5.1 Processing Outline 85
3.5.2 Algorithm Input 87
3.5.2.1 VIIRS Data 87
3.5.2.2 Non-VIIRS Data 90
3.5.3 Theoretical Description of the Retrieval 90
3.5.3.1 Physics of the Problem 90
3.5.3.2 Mathematical Description of the Sea Ice Algorithms 94
3.5.3.3 Archived Algorithm Output 98
3.5.3.4 Algorithm Watch List 98
3.5.4 Performance of Sea Ice Data 99
3.5.4.1 Stratification 99
3.5.4.2 Stratified Performance Analysis 101
3.5.4.3 Error Budgets 113
3.5.4.4 Limits of Applicability 115
3.5.5 Practical Considerations 116
3.5.5.1 Numerical Computation Considerations 116
3.5.5.2 Programming and Procedural Considerations 117
3.5.5.3 Configuration of Retrievals 117

3.5.5.4 Quality Assessment and Diagnostics 118
3.5.5.5 Exception Handling..... 118

3.6 ALGORITHM VALIDATION..... 118

4.0 ASSUMPTIONS AND LIMITATIONS 121

4.1 ASSUMPTIONS..... 121

4.2 LIMITATIONS..... 121

5.0 REFERENCES 123

APPENDIX A VIIRS USER'S GUIDE..... A-1

LIST OF FIGURES

Page

Figure 1. Comparison of the VIIRS band set for Imagery with OLS and AVHRR-3. 9

Figure 2. Reflectivity, absorptivity, and transmissivity of atmosphere, surface, and clouds in the Short Wave Infrared (SWIR) 25

Figure 3. Phenomenology of the VIIRS Daytime Visible (DV) Imagery band, centered at 640 nm. 26

Figure 4. Phenomenology of the VIIRS Long-Wave Infrared (LWIR) Imagery band, centered at 11.45 microns. 27

Figure 5. Phenomenology of the VIIRS Mid-Wave Infrared (MWIR) Imagery band, centered at 3.74 microns. 28

Figure 6. Summary of VIIRS design concepts and heritage 35

Figure 7. VIIRS detector footprint aggregation scheme for building Imagery "pixels" 36

Figure 8. Horizontal Sampling Interval (HSI) for imagery bands (aggregation in scan direction). 36

Figure 9. VIIRS aggregation and bow tie pixel reduction 37

Figure 10. Signal-to-noise performance of the Daytime/Nighttime Visible Imagery Band at nadir, for each of the three CCD gain stages. SNR performance over the specified measurement range (4.E-9 – 3.E-2 W/cm^2/sr) is 30 to 1000. SNR greater than 3 is achieved at a radiance as low as 3.2E-10 W/cm^2/sr. 38

Figure 11. Signal-to-noise performance of the Daytime/Nighttime Visible Imagery Band at edge of scan, for each of the three CCD gain stages. SNR performance over the specified measurement range (4.E-9 – 3.E-2 W/cm^2/sr) is 7 to 250. SNR greater than 3 is achieved at a radiance as low as 1.8E-9 W/cm^2/sr. 39

Figure 12. Spectral Response of the Daytime/Nighttime Visible Imagery band, compared with the lunar signal. 40

Figure 13. SNR Performance of the Daytime/Nighttime Visible Imagery under quarter-moon illumination conditions, as a function of scan angle. 41

Figure 14. Typical Gain Value Versus Scene Source Elevation (GVVSSE) Curve for OLS on board variable gain control. The curve is designed so that a source with an

albedo = 0.8 produces a 5 volt output signal from the L channel analog signal processor (Reference: OLS Technical Operating Report, March 1993)..... 43

Figure 15. Process flow for the NCC Imagery algorithm 45

Figure 16. F13 OLS Visible (HRD) image for the first terminator crossing of the July 20, 2001 1131 UT orbit 49

Figure 17. Input radiance image to the NCC algorithm..... 51

Figure 18. NCC Algorithm Output 51

Figure 19. NOAA-12 AVHRR Channel 1 and Channel 2 imagery collected over western U.S. at 1505 GMT on March 19, 1996..... 60

Figure 20. NOAA-12 AVHRR Channel 3 and Channel 5 imagery collected over western U.S. at 1505 GMT on March 19, 1996..... 61

Figure 21. NOAA-12 AVHRR Channel 1 and the derived 3.7-µm (albedo) data for the scene collected 1505 GMT on March 19, 1996..... 62

Figure 22. Color composite of NOAA-12 AVHRR imagery created by assigning Channels 1, 3, and 5 to the red, green and blue guns of a CRT. 62

Figure 23. Methodology illustrated in using MAS data to construct Color Composites using Imagery and Imagery Assist bands..... 65

Figure 24. RGB Composites of bands (0.64, 1.61, 10.8./11.45)..... 66

Figure 25. RGB Composites of bands RGB (1.38[1.88], 1.61,11.45)..... 67

Figure 26. RGB Composites of bands RGB (1.61, Invert BT8.6, 0.64)..... 68

Figure 27. Day/Night Composite #4 - RGB (BT11.45, BT8.6, BT3.75)..... 69

Figure 28. Color composite of MAS data collected over Denver, CO [RGB= (0.64 µm, 0.858 µm, 0.64 µm)]..... 70

Figure 29. Color composite of NOAA-15 AVHRR imagery created by assigning the 0.64 µm, 1.61 µm, 10.8 µm channels to the red, green and blue guns of a CRT..... 71

Figure 30 (a.) Color Composite of MAS imagery over Denver, CO [RGB (0.64, 1.61, 3.75 albedo] (b.) [RGB (3.75, 10.8,11.45)]..... 73

Figure 31. Depiction of the Nesting of the VIIRS Imagery (Fine) Resolution Bands within the VIIRS Moderate Resolution Bands 75

Figure 32. VIIRS sensing requirements were based upon a variety of surface classifications. 79

Figure 33. Measurement uncertainty based upon manually-generated cloud analysis of simulated VIIRS 12.0-µm imagery created for cirrus optical depth 0.03. 80

Figure 34. Process flow for the Imagery Sea Ice ARP algorithms. 85

Figure 35. Distribution of 640 nm reflectance for an ice/water scene. The ice/water threshold reflectance (0.336) and the water tie point (0.083) are indicated. 96

Figure 36. Distribution of 640 nm reflectance for a local search window centered on a single pixel of the scene. 96

Figure 37. Illustration of the ice concentration performance analysis methodology. The scene is from the FIRE-ACE campaign of the MODIS Airborne Simulator (ACE_65_3). 104

Figure 38. (a) Simulated VIIRS daytime visible band imagery of the Bering Sea scene AK74_14. (b) Retrieved ice reflectance tie points. (c) Ice thickness, derived from the reflectance tie points 106

Figure 39. Simulated VIIRS nighttime imagery of the Bering Sea scene AK74_14, for air temperatures of 0 degrees Celsius (a), -5 degrees Celsius (b), -10 degrees Celsius (c), and -20 degrees Celsius (d) 107

Figure 40. Illustration of ice edge location retrieval. The scene is from the FIRE-ACE campaign of the MODIS Airborne Simulator (ACE_65_3). 111

LIST OF TABLES

Page

Table 1. Imagery EDR Products 2

Table 2. Explicit Requirements for the VIIRS Imagery EDR 8

Table 3. Specifications for the VIIRS Cloud Cover Imagery ARP 13

Table 4. Specifications for the VIIRS Cloud Type Imagery ARP 14

Table 5. Specifications for the VIIRS Ice Edge Location Imagery ARP 19

Table 6. Specifications for the VIIRS Ice Concentration Imagery ARP 20

Table 7. Imagery EDR – Input Data Summary (Spatial) 23

Table 8. Imagery EDR – Input Data Summary (Radiometric) 23

Table 9. Ancillary data to augment manual cloud analysis. 54

Table 10. 64 Bit Intermediate Product output of the VIIRS Cloud Mask 76

Table 11. Cloud Cover Measurement Uncertainty 81

Table 12. Measurement Uncertainty versus HCS from manual analysis of cirrus with visible optical depth of 0.03 81

Table 13. Approach to the positive identification of cloud types by human analysts using VIIRS imagery and imagery assist bands. 83

Table 14. Imagery (Sea Ice Data) – Input Data Summary 87

Table 15. VIIRS data for the Imagery (Sea Ice Data) products 87

Table 16. Ice Concentration Measurement Uncertainty, Case 1 (Clear, Nadir, SZA=60 degrees) 108

Table 17. Ice Concentration Measurement Uncertainty, Case 2 (Clear, Nadir, Night, Air Temperature = -5 Celsius) 108

Table 18. Ice Concentration Measurement Uncertainty, Case 3 (Clear, Nadir, Night, Air Temperature = -10 Celsius) 108

Table 19. Ice Edge Location Measurement Uncertainty (km), Case 1 (Clear, Nadir, SZA=60 degrees) 112

Table 20. Ice Edge Location Measurement Uncertainty (km), Case 2 (Clear, Nadir, Night, Air Temperature = -5 Celsius) 112

Table 21. Ice Edge Location Measurement Uncertainty (km), Case 3 (Clear, Nadir, Night, Air Temperature = -10 Celsius) 112

Table 22. Error Budget for Ice Concentration 114

Table 23. Error Budget for Ice Edge Location (Nadir) 115

Table 24. Error Budget for Ice Edge Location (Edge of Scan) 115

GLOSSARY OF ACRONYMS

ADVCLD	Global cloud forecast model based upon trajectory scheme
AFWA	Air Force Weather Agency
ARP	Application-Related Product
ASGC	Along Scan Gain Control
ASP	Analog Signal Processor
ATBD	Algorithm Theoretical Basis Document
AVHRR	Advanced Very High Resolution Radiometer
AVIRIS	Airborne Visible/Infrared Imaging Spectrometer
BRDF	Bidirectional Reflectance Distribution Function
BT	Brightness Temperature
BTD	Brightness Temperature Difference
CCD	Charge Coupled Device
CDFS	Cloud Depiction and Forecast System
CDR	Critical Design Review
CGTA	Cloud Ground Truth Analysis
CI	Cirrus
CLAVR	Clouds from AVHRR
cm	centimeter
CMIS	Conical Scanning Microwave Imager/Sounder
CNC	Cloud-No Cloud
CRT	Cathode Ray Tube
CU	Cumulus
DMSP	Defense Meteorological Satellite Program
DN	Digital Number
DNB	Daytime Nighttime Band
DoD	Department of Defense
DV	Daytime Visible
EBBT	Equivalent Blackbody Temperature
EDC	EROS (Earth Resources Observation System) Data Center
EDR	Environmental Data Record
EOSDIS	Earth Observing System Data and Information System
FIRE-ACE	First ISCCP Regional Experiment – Arctic Cloud Experiment
FOV	Field of View
GIFOV	Ground Instantaneous Field of View
GLI	Global Imager
GMA	Gain Management Algorithm

GMT	Greenwich Meridian Time
GOES	Geostationary Operational Environmental Satellite
GSD	Ground Sample Distance
GTOPO30	Global Topographic 30 arc second map
HCS	Horizontal Cell Size
HRCP	High-Resolution Cloud Prognosis
HRD	High Rate Data; also High Resolution Diode
HRI	Horizontal Reporting Interval
HSI	Horizontal Sampling Interval
HSR	Horizontal Spatial Resolution
IDPS	Interface Data Processor Segment
IORD	Integrated Operational Requirements Document
IP	Intermediate Product
IPO	Integrated Program Office
IPT	Integrated Product Team
IR	Infrared
ISCCP	International Satellite Cloud Climatology Project
K	Kelvin
km	kilometer
LLLS	Low Level Light Sensor
LOS	Loss of Signal
LRD	Low Rate Data
LUT	Look Up Table
LUTGT	Look Up Table Generation Tool
LWIR	Long-Wave Infrared
m	meter
MAS	MODIS Airborne Simulator
MODIS	Moderate Resolution Imaging Spectroradiometer
MODTRAN	Moderate Resolution Atmospheric Radiance and Transmittance Model
MOSART	Moderate Spectral Atmospheric Radiance and Transmittance
MTF	Modulation Transfer Function
MWIR	Mid-Wave Infrared
NASA	National Aeronautics and Space Administration
NCC	Near Constant Contrast
NEdT	Noise Equivalent delta Temperature
NGDC	National Geophysical Data Center
NIC	National Ice Center
NIR	Near Infrared

NOAA	National Oceanic and Atmospheric Administration
NPOESS	National Polar-Orbiting Operational Environmental Satellite System
NPP	NPOESS Preparatory Project
OLS	Operational Linescan System
P^3I	Pre-Planned Product Improvement
PDR	Preliminary Design Review
QC	Quality Control
RDR	Raw Data Record
RGB	Red-Green-Blue
RMS	Root Mean Square
RMSE	Root Mean Square Error
RSS	Root Square Sum
RT	Radiation Transfer
RTNEPH	Real Time NEPH Analysis
SBIRS	Space-Based Infrared System
SBRS	Santa Barbara Remote Sensing
SDHS	Satellite Data Handling System
SDR	Sensor Data Record
SDSM	Solar Diffuser Stability Monitor
SeaWiFS	Sea-viewing, Wide-Field-of-View Sensor
SERCAA	Support of Environmental Requirements for Cloud Analysis and Archive
SNR	Signal-to-Noise Ratio
sr	steradian
SRD	Sensor Requirements Document
ST	Stratus
SWIR	Short Wave Infrared
SZA	Solar Zenith Angle
TBD	To Be Determined
TBR	To Be Reviewed
TBS	To Be Specified
TDI	Time Delay and Integration
TERCAT	Terrain Categorization
THEMIS	Thermal Emission Imaging System
TIM	Technical Interchange Meeting
TIROS	Television Infrared Observation Satellite
TOA	Top of Atmosphere
VCM	VIIRS Cloud Mask
VDGA	Variable Digital Gain Amplifier

VIIRS	Visible/Infrared Imager/Radiometer Suite
VIS	Visible
VMCD	VIIRS Manually-Generated Cloud Data
VNIR	Visible/Near Infrared
VOAT	VIIRS Operational Algorithm Team
W	Watts
WINCE	Winter Cloud Experiment

ABSTRACT

This Imagery Algorithm Theoretical Basis Document (ATBD) describes the background, theory, and analysis of the algorithmic process required to create Imagery Environmental Data Records (EDRs) from the sensor Raw Data Records (RDRs) of the National Polar-orbiting Operational Environmental Satellite System (NPOESS) Visible/Infrared Imager/Radiometer Suite (VIIRS). The process has been developed to satisfy the requirements of the VIIRS Sensor Requirements Document (SRD), Version 3, released by the Integrated Program Office (IPO). This document is version 5 of the Imagery ATBD. It is intended to completely supersede previous versions.

The document covers all VIIRS imagery processing. In particular, it describes algorithms for producing four imagery products: Explicit Imagery, Near Constant Contrast (NCC) Visible Imagery, Manually Generated Cloud Data, and Sea Ice Data.

Four imagery bands are specified. The Daytime/Nightime Visible Band (DNB), Daytime Visible Band (DV), and Long-Wave Infrared Band (LWIR) are explicitly required by the SRD. The Mid-Wave Infrared Band (MWIR) was added as a result of flowdown of the Imagery Application-Related requirements. For each spectral band for which imagery is provided, Explicit Imagery includes the following two data products, both generated by ground processing of VIIRS data:

(a) a two-dimensional array of locally averaged absolute in-band radiances at the top of the atmosphere, measured in the direction of the viewing instrument, and

(b) the corresponding array of equivalent blackbody temperatures (EBBT) if the band is primarily emissive, or the corresponding array of top-of-the-atmosphere (TOA) reflectances if the band is primarily reflective during daytime.

The VIIRS Imagery EDR benefits from true multispectral capability and compatibility with heritage from the Department of Defense (DoD) Defense Meteorological Satellite Program (DMSP) Operational Linescan System (OLS). The radiometric performance of the bands exceeds the specification for Measurement Uncertainty with margins that allow the performance of the Application-Related Products (ARPs) to meet or approach objective requirements.

The Explicit Imagery is computed from the VIIRS RDRs in the Build-SDR module, which applies geo-location, Earth gridding, and calibration to the RDRs. The functionality of the Build-SDR module will allow it to produce Sensor Data Records (SDRs) that fully meet the explicit imagery requirements. All Imagery products shall be calibrated, geolocated, and reported for a set of earth locations forming an approximately rectangular lattice. The lattice spacing will be 742 meters +/- 5% for the DNB, and approximately equivalent to the Horizontal Spatial Resolution (HSR) for the other imagery bands.

DNB data are obtained from a sensitive, very-wide-dynamic range Charge-Coupled Device (CCD) detector in the main VIIRS Sensor. To encompass the extreme radiometric dynamic range of day and night scenes, the DNB CCD includes four regions of light-sensitive photosites with three different sensitivities. The three regions are designed so that before a more sensitive region saturates, the next less sensitive region will have received a signal sufficient to produce an

acceptable signal-to-noise ratio (SNR). Analog signals from all three regions are converted into digital form and processed digitally to select the signal from the region offering the best SNR for each pixel. The CCD design allows any number of subpixel elements to be aggregated into single pixels as they are read from the CCD. In the VIIRS sensor this capability will be used to generate pixels with near-rectangular sample spacing on the ground. At nadir, SNR performance of the DNB over the specified measurement range (4.E-9 – 3.E-2 Watts/cm^2/sr) is 30 to 1000. SNR greater than 3 is achieved at a radiance as low as 3.2E-10 Watts/cm^2/sr. At edge of scan, SNR performance of the DNB over the specified measurement range (4.E-9 – 3.E-2 Watts/cm^2/sr) is 7 to 250. SNR greater than 3 is achieved at a radiance as low as 1.8E-9 Watts/cm^2/sr. SNR greater than 10 is achieved at the minimum radiance for almost the entire scan.

NCC Visible Imagery is derived from the broad day/night band near the terminator region. Due to the significant change in solar irradiance across the terminator, a three-stage CCD sensor is designed to record the radiance in this region. The individual detectors in the three portions of the CCD are used to record daytime, day/night crossing time, and nighttime radiance, respectively. The SDR for this band consists of a single set of data that contains all three stages in all illumination conditions. The radiance values cover a very large dynamic range, from 4E-9 to 3E-2 Watts/cm^2/sr. Due to the switch of gain across the terminator, the digital numbers present artificial boundaries. DNB calibration will remove the boundaries and provide calibrated TOA radiance over the entire dynamic range. The NCC algorithm converts the TOA radiance to albedo by modeling the solar and lunar source radiance for each pixel. The algorithm preserves heritage from the OLS Gain Management Algorithm (GMA) through the use of look up tables (LUTs) designed to mimic the GMA. An enhanced NCC algorithm removes path radiance and normalizes the path-removed radiance values according to an empirical function between the TOA radiance and solar/lunar angles for a model atmosphere and a reference surface with constant albedo. The enhancement will require an improved radiative transfer model, as the latest version of MODTRAN is not accurate at the terminator. The enhancement will be implemented when and if its superior performance is validated with NPP/VIIRS data.

Manual cloud analysis is based upon the contrast, measured in brightness temperatures or albedo, between the cloud and the surrounding cloud-free background. In infrared (IR) imagery, cloud detection is enhanced not only by temperature contrasts between the features but also by observing the features in spectral bands where their emissivity contrasts exist. In visible and near-infrared imagery, cloud detection relies on contrasts in the reflectivities of the features while at mid-infrared wavelengths, e.g. 3-5 microns, both temperature and reflected solar energy can be exploited in the manual cloud analysis process. Image enhancement techniques such as histogram equalization and thresholding enable the analyst to delineate individual features. False-colored compositing of multispectral images facilitates manual interpretation of the clouds and background features by assigning colors to those pixels with different multispectral responses. Using these tools, the analyst can systematically and quickly identify and classify the various clouds in the imagery. A User's Guide has been developed for the training of VIIRS Imagery analysts. The first version of the User's Guide is included as an appendix to this ATBD.

The VIIRS SRD requires that the content and quality of the Imagery EDR be adequate to allow for specified requirements on sea ice edge location and sea ice concentration to be met. Sea ice

data may be generated interactively by a trained analyst viewing unprocessed or processed imagery at a computer workstation, or automatically via an algorithm. The requirements for sea ice data products cannot be achieved by manual analysis. Our approach for sea ice can be used to develop operational algorithms to retrieve sea ice data products automatically on a global basis. This capability will be of great value to operational ice centers in the NPOESS era.

Ice concentration is defined as the fraction of a given area of sea water covered by ice. It is typically derived from imagery and reported on ice charts for areas between contours generated by an analyst. But for the purpose of verifying the measurement uncertainty requirement, ice concentration is reported as a gridded product for areas of size limited by the Horizontal Cell Size (HCS) requirement and separation limited by the Horizontal Reporting Interval (HRI) requirement. We retrieve ice concentration operationally from an automated algorithm. The algorithm includes the derivation of ice fraction for imagery pixels, using tie point analysis of surface temperature and surface reflectance. The surface temperatures and surface reflectances are acquired operationally from VIIRS Intermediate Products (IPs). Operational capability is achieved by the use of local search windows to derive ice and water tie points and by automated cloud masking. Ice concentration is reported at imagery resolution with measurement uncertainty better than 0.1 in most cases. Optimized parameters of a search window and band weight reduce tie point errors and provide a seamless day/night transition.

The sea ice edge is defined as the boundary between ice-covered sea water (ice concentration > 0.1) and sea water not covered by ice (ice concentration ≤ 0.1). An automated algorithm produces ice edge location as a binary edge/no edge map at the imagery pixel resolution and also as a set of latitude/longitude edge coordinates. The coordinates are determined at subpixel resolution by interpolation of the ice concentration map in the vicinity of the ice edge. The ice edge is located in most cases with a measurement uncertainty of less than 0.3 km at nadir. This estimate of algorithm quality performance corresponds to the case of compacted ice edge. The ice edge location and ice concentration retrieved by our automated algorithms will be archived as a part of the VIIRS Imagery EDR product, for use by analysts at national ice centers.

1.0 INTRODUCTION

1.1 PURPOSE

This Visible/Infrared Imager/Radiometer Suite (VIIRS) Imagery Algorithm Theoretical Basis Document (ATBD) describes the processing steps required to transform all VIIRS Imagery Raw Data Records (RDR) generated by the VIIRS sensor into Imagery Environmental Data Records (EDRs) and Imagery Application-Related Products (ARPs).

The NPOESS VIIRS Sensor Requirements Document (SRD) identifies three classes of imagery:

(a) Explicit imagery requirements, which includes at least one daytime visible, one nighttime visible, and one infrared imagery channel

(b) Application-related imagery requirements, which are imagery channels needed to satisfy threshold requirements for Manually-Generated Cloud Data and Sea Ice Data, and

(c) Derived imagery requirements, which are contractor-derived and based on requirements for other EDRs supported by the imagery.

The Imagery algorithm consists of four major processing functions:

(1) Generation of the Explicit Imagery from the imagery resolution (EV_375M) and Day/Night Band (EV_DNB) Sensor Data Records (SDRs).

(2) Creation of Near Constant Contrast (NCC) visible imagery from the daytime/nighttime visible imagery SDR (EV_DNB).

(3) Manual generation of cloud data products (Cloud ARPs)

(4) Generation of sea ice data products (Sea Ice ARPs) by an automated algorithm.

1.2 SCOPE

All aspects of VIIRS imagery processing are described in this ATBD, including the Explicit Imagery, the NCC Visible Imagery, the Cloud ARPs, and the Sea Ice ARPs.

This section of the ATBD introduces the Imagery algorithm. Section 2 provides an overview of the Imagery EDR requirement, specifications, and retrieval strategy. Section 3 describes the algorithm's functions in detail, including the process flow, input data, theoretical basis, mathematical description, performance analysis, practical considerations, initialization, and validation. Section 4 states the assumption and limitations on which the algorithm is based, and Section 5 provides references for the publications cited in this document. A User's Guide for VIIRS Cloud Imagery products in included as an Appendix.

Our specification and performance for the VIIRS Imagery EDR and Application-Related Requirements based on Imagery are achieved with the 9 EDR products listed in Table 1.

Table 1. Imagery EDR Products

Imagery EDR Product	VIIRS Band(s)	Wavelength (μm)	Horizontal Resolution Nadir / At 3000 km swath
* Daytime Visible (DV), TOA Radiance, TOA Reflectance	I1	0.60 - 0.68	0.4 km / 0.8 km
* Daytime/Nighttime Visible (DNB), TOA Radiance, TOA Reflectance	DNB	0.5 – 0.9	0.74 km **
* NCC Visible Imagery	DNB	0.5 – 0.9	0.74 km **
* Mid Wave IR (MWIR), TOA Radiance, Equivalent Blackbody Temperature	I4	3.55 – 3.93	0.4 km / 0.8 km
* Long Wave IR (LWIR), TOA Radiance, Equivalent Blackbody Temperature	I5	10.5 – 12.4	0.4 km / 0.8 km
*** Manually Generated Cloud Cover	I1, I4, I5	N/A	1.2 km / 2.4 km
*** Manually Generated Cloud Type	I1, I4, I5	N/A	1.2 km / 2.4 km
*** Sea Ice Concentration	I1, I5	N/A	0.4 km / 0.8 km
*** Sea Ice Edge Location	I1, I5	N/A	0.4 km / 0.8 km

* Explicit Imagery EDR Requirement
** Constant to within 5% in both directions within a swath
*** Imagery Application-Related Product

1.3 VIIRS DOCUMENTS

This document contains references to other Raytheon VIIRS documents, designated by a document number, which is given in italicized brackets. The VIIRS documents cited in this document are:

[SS 154640-001] - VIIRS System Specification

[PS 154640-101] - VIIRS Sensor Specification

[TP 154640-001] - VIIRS System Verification and Validation Plan Document

[TP 154640-118] - VIIRS Radiometric Calibration and Validation Plan

[Y2400] - VIIRS Vegetation Index ATBD

[Y2401] - VIIRS Snow Cover ATBD

[Y2404] - VIIRS Fresh Water Ice ATBD

[Y2405] - VIIRS Ice Surface Temperature ATBD

[Y2409] - VIIRS Sea Ice Age/Edge Motion ATBD

[Y2411] - VIIRS Surface Reflectance ATBD

[Y2412] - VIIRS Cloud Mask ATBD

[Y2468] - VIIRS Operations Concept document

[Y2469] - VIIRS Context Level Software Architecture

[Y2470] - VIIRS Interface Control Document

[Y2471] - VIIRS Aerosol Module Level Software Architecture

[Y2472] - VIIRS Cloud Module Level Software Architecture

[Y2477] - VIIRS Snow Ice Module Level Software Architecture

[Y2478] - VIIRS Build-RDR Module Level Software Architecture Document

[Y2479] - VIIRS Build SDR Module Level Software Architecture

[Y2506] - VIIRS Ice Edge Location Unit Level Detailed Design Document

[Y3235] - VIIRS Ice Concentration Unit Level Detailed Design Document

[Y3236] - VIIRS Software Integration and Test Plan

[Y3237] - VIIRS Algorithm Verification and Validation Plan

[Y3258] - VIIRS Geolocation ATBD

[Y3261] - VIIRS Radiometric Calibration ATBD

[Y3270] - VIIRS System Verification and Validation Plan

[Y3273] - VIIRS Imagery Unit Level Detailed Design Document

[Y3277] - VIIRS Aerosol Module Level Interface Control Document

[Y3278] - VIIRS Cloud Module Level Interface Control Document

[Y4963] - VIIRS Imagery TIM, March 8, 2000

[Y10810] - VIIRS Look up Table Generation Tool (LUTGT) Detailed Design Document

[Y10880] – VIIRS Surface Temperature IP Unit Level Detailed Design Document

[Y11649] – VIIRS Ice Quality Unit Level Detailed Design Document

1.4 REVISIONS

This is the fifth version of this document, dated March 2002. Version 5.0 is released as part of the Raytheon NPOESS/VIIRS Critical Design Review (CDR) package. The first two versions were developed in response to VIIRS Sensor Requirements Document (SRD), revision 1, dated August 3, 1998. The first version was dated October 1998. The second version was dated June 1999. The third version, dated May 2000, was developed in response to VIIRS Sensor Requirements Document (SRD), Version 2, Revision a, dated 04 November 1999 and was submitted as part of the Raytheon NPOESS/VIIRS Preliminary Design Review (PDR) and Proposal packages.

Changes for version 3 were largely in response to revisions in the new SRD. They included:

- Modification of the process flow
- Addition of an algorithm for producing the NCC imagery
- Performance summary for meeting manual cloud detection thresholds and objectives
- Identification of cloud type classifications that meet system level thresholds and objectives
- Plans for developing a VIIRS users guide for manual cloud identification and typing
- Development of scene-specific tie point analysis of reflectance and/or surface temperature for the automated sea ice concentration algorithm
- Development of an automated algorithm to retrieve ice edge location
- Reporting of ice edge location as an ice edge map and a set of latitude/longitude coordinates
- Additional sea ice test results, from an expanded test data set
- A revised sea ice specification, with supporting error analysis and error budget

The primary purpose of version 4 was to respond to VIIRS Algorithm Watch List items generated by the VIIRS Operational Algorithm Team (VOAT). An additional purpose is to incorporate minor revisions generated by an internal Raytheon review since the VIIRS PDR. Changes since version 3 included:

- A new baseline algorithm for NCC Imagery, adapted from the OLS on-board algorithm

- Expanded description of input data
- Revision and enhancement of the process flow description
- Responses to relevant VOAT Watch List Items

This document, version 5.0, incorporates the post-PDR developments in software architecture and detailed design that bring the algorithm to a CDR level of maturity. Changes since version 4 include:

- A change to the specification for the Daytime Visible band (I1)
- A modification of the high rate data (HRD) stream, implementing bow tie deletion
- Additional development of the algorithm for NCC Imagery, with a detailed process flow and a detailed description of the LUTs.
- Development of the User's Manual for VIIRS Cloud Imagery
- Additional development of the algorithm for the Sea Ice ARPs, with a detailed process flow and a detailed description of the LUTs.
- Detailed development of quality flags for all of the Imagery EDR automated products

2.0 EXPERIMENT OVERVIEW

2.1 EDR DEFINITION

Imagery requirements fall into three classes:

(a) Explicit requirements on the EDR content, quality, reporting frequency, and timeliness.

(b) Requirements to be derived based on specific applications utilizing the imagery EDR, such as manual generation of cloud and sea ice data.

(c) Requirements to be derived from requirements for other EDRs supported by the imagery.

2.2 EXPLICIT IMAGERY REQUIREMENTS

For each spectral band for which imagery is provided, the Imagery EDR includes the following two data products, both generated by ground processing of VIIRS data:

1. A two-dimensional array of locally averaged absolute in-band radiances at the top of the atmosphere, measured in the direction of the viewing instrument, and

2. The corresponding array of equivalent blackbody temperatures (EBBTs) if the band is primarily emissive, or the corresponding array of top-of-the-atmosphere (TOA) reflectances if the band is primarily reflective during daytime.

The radiances, EBBTs, and reflectances are reported for a set of earth locations forming an approximately rectangular lattice, with the spacing between locations constrained by the Horizontal Reporting Interval (HRI) requirement. The form of the spatial weighting function that determines the local averaging of the absolute TOA radiance is constrained by the Horizontal Spatial Resolution (HSR) requirement. The number of spectral bands, band limit values, measurement ranges, and measurement uncertainty (or accuracy and precision) requirements are to be derived based on the application-related requirements and on the requirements of other EDRs supported by the imagery.

The Imagery EDR must satisfy the following additional requirements:

1) Every spectral band deemed to be essential to meet the application-related threshold requirements shall meet all of the explicit imagery requirements. Spectral bands used to improve performance toward objective levels need not meet the explicit imagery requirements.

2) At a minimum, at least one daytime visible, one daytime/nighttime visible, and one IR channel shall meet the explicit imagery requirements.

3) Every spectral band essential to meeting the application-related threshold requirements shall have the same nominal pixel HSR and HSI design values, or better than nominal values by an integral factor, and pixels in any two of these bands shall be co-registered to within 20% of the nominal pixel HSR. This requirement does not apply to the daytime/nighttime visible band.

The explicit requirements and specifications are summarized in Table 2.

Table 2. Explicit Requirements for the VIIRS Imagery EDR

Para. No	Parameter	Thresholds	Objectives	Specification Value
	a. Horizontal Spatial Resolution (HSR)			
V40.2.3.1-2	1. At nadir	0.4 km	(TBD**)	0.4 km
V40.2.3.1-3	2. Worst case	0.8 km	0.1 km	0.8 km
V40.2.3.1-6	5. Daytime/Nighttime Visible, worst case	2.6 km	0.65 km	0.74 km
V40.2.3.1-7	b. Horizontal Reporting Interval	Derived (gapless or near gapless coverage required)	Derived (gapless or near gapless coverage required)	Imagery HSR *
	c. Horizontal Coverage	Global	Global	Global
	d. Measurement Range			
V40.2.3.1-11	1. Daytime/Nighttime visible	4E-9 – 3E-2 Watts/(cm2-sr) in 0.4-1.0 um band, or equivalent in another band	Includes threshold range	4E-9 – 3E-2 Watts/(cm2-sr)
V40.2.3.1-12	2. Other bands			
	Daytime Visible	Derived	Derived	5 to 718 Watts/(m2-sr-µm)
	Mid-Wave Infrared	Derived	Derived	210 K to 353 K
	Long-Wave Infrared	Derived	Derived	210 K to 340 K
V40.2.3.1-13	Measurement Uncertainty			
	Daytime/Nighttime Visible	Derived	Derived	6.5E-10 Watts/(cm2-sr) @ L = 4.E-09 Watts/(cm2-sr) (edge of scan)
	Daytime Visible	Derived	Derived	SNR = 119 @ Ltyp = 23 Watts/(m2-sr-µm) (edge of scan)
	Mid-Wave Infrared	Derived	Derived	NEdT**** = 2.5 K @ Ttyp = 270K (edge of scan)
	Long-Wave Infrared	Derived	Derived	NEdT**** = 1.5 K @ Ttyp = 210K (edge of scan)
	f. Mapping Uncertainty			
V40.2.3.1-14	1. At nadir	3 km	1 km (TBD**)	
V40.2.3.1-15	2. Worst case	4 km	1 km (TBD**)	
V40.2.3.1-16	Minimum Swath Width (All other EDR thresholds met)	3000 km (TBR*** = 3000 km)	3000 km (TBD**)	3000 km

* For Daytime/Nighttime Visible Band, HRI = 742 m., constant to within 5% in both directions within a swath
** To Be Determined *** To Be Reviewed **** Noise Equivalent delta Temperature

A schematic comparison of the VIIRS bands listed in Table 2 with the OLS and the National Oceanic and Atmospheric Administration (NOAA) Advanced Very High Resolution Radiometer (AVHRR) band sets is shown as Figure 1.

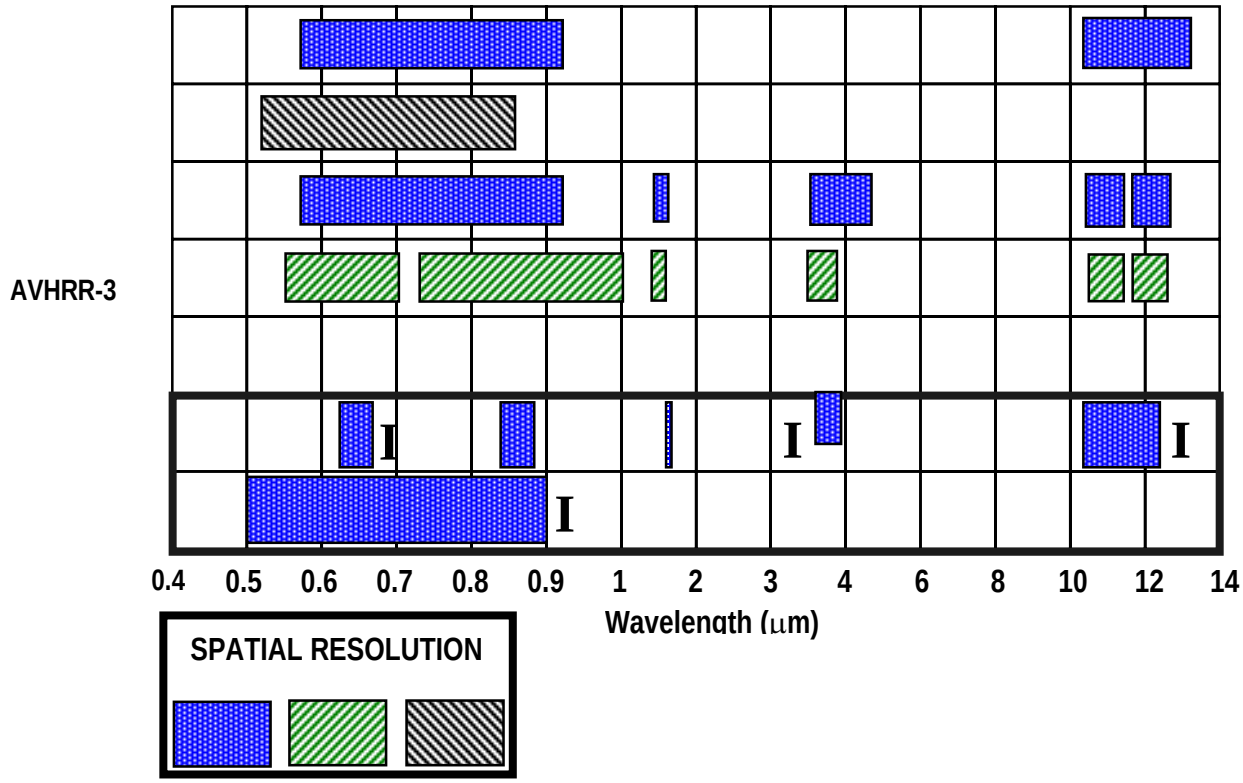

Figure 1. Comparison of the VIIRS band set for Imagery with OLS and AVHRR-3.

VIIRS bands marked "I" are required to meet the Imagery EDR threshold requirements. The legend indicates the spatial resolution of the band sets. OLS PMT channel bands are at coarse resolution (gray). AVHRR-3 bands are at moderate resolution (green). The other band sets are at imagery resolution (blue). The VIIRS Imagery EDR benefits from true multispectral capability and compatibility with OLS heritage.

2.2.1 Change in Specification of the Daytime Visible Imagery Band (I1)

On June 27, 2001, Raytheon submitted ICSR # G1062701, proposing a change to the spectral characteristics of VIIRS band I1.

Early in Phase II, Raytheon began a systematic review of saturation characteristics in the VIIRS reflective bands. It was determined that the maximum spectral radiance (Lmax) in band I1 is not sufficient for cloud applications. I1 is the primary visible band for the Imagery EDR during daytime. This band must therefore provide sufficient dynamic range to maximize the capability of VIIRS for the Cloud Type application related requirement (Section 2.4.2). The original specification for Lmax in I1 was 468 Wm-2sr-1μm-1. For an overhead sun reflecting off a

Lambertian surface, this is equivalent to a reflectance of 92%. This reflectance level is often substantially exceeded for deep convective clouds. In fact, the anisotropic reflectance of cloud tops and cloud sides is such that certain combinations of solar and viewing geometry will lead to reflectances on the order of 130%. This is evidenced most recently in MODIS data, where the reflectance in band 1 (spectrally equivalent to the original specification for I1) has an Lmax specification of 685 (134% reflectance), and the entire dynamic range is covered by a significant number of MODIS observations. Based on the initial feedback from MODIS data users, and based also on our own investigations of MODIS imagery, Raytheon determined that I1 should reach an equivalent reflectance of 134%, to continue the heritage in MODIS high-resolution cloud imagery capability in a manner that will give maximum benefit to operational imagery analysis at the Air Force Weather Agency (AFWA).

The difficulty in making this change to the Lmax in I1 is that signal to noise ratio (SNR) is degraded. Raising Lmax to 685 Wm-2sr-1m-1 would entirely eliminate the margin between the SNR specification and expected SNR performance. In order to raise Lmax in I1 at low risk, it is necessary to compensate with some other adjustment to preserve an acceptable level of SNR margin. The trade space for such adjustments is actually quite small. Time delayed integration (TDI) is not a low-risk option at this stage of the design and fabrication effort, would require a significant increase in associated processing electronics, and complicate the already tight band-to-band registration requirements. Dual gain cannot be implemented in the imagery bands due to insufficient readout time. MTF cannot be relaxed without increasing risk to the HSR requirements for I1. Consequently, the most viable option is to widen the band spectrally, increasing the number of photons incident on the detector for a given observation.

Raytheon determined that if VIIRS band I1 were to adopt the AVHRR/3 heritage for visible remote sensing (580-680 nm), causing an increase in both Lmax and Ltyp by moving closer to the maximum in spectral solar irradiance, 40% margin would be preserved against the translated SNR requirement. The band would still be narrower than the equivalent OLS band, and would offer comparable or better SNR at the output than was specified for the OLS prior to quantization. This change would preserve the requirement that VIIRS offer comparable or improved performance compared to current operational sensors, either AVHRR or OLS.

The benefits to Imagery applications by making this change are clear. The only significant impact on other VIIRS EDRs is to the Vegetation Index EDR. The reflectance properties of vegetation make the NDVI sensitive to the width of the visible band used for the NDVI *[Y2400]*. Therefore, widening the I1 band degrades the contrast in NDVI between vegetated and non-vegetated surfaces, and breaks continuity with the MODIS NDVI. To mitigate these adverse effects on the NDVI, the IPO and VOAT recommended that the band widening be limited to 80nm, with a band center shifted from 645 nm to 640 nm. For this band width, Lmax of 718 Wm-2sr-1um is equivalent to Lmax of 685 Wm-2sr-1um in the 620-670 nm band. On September 5, 2001, the NPOESS Integrated Program Office (IPO) Configuration Control Board approved a change to the VIIRS Sensor Performance Specification for the I1 imagery band spectral characteristics. The revised specification, incorporated into Tables 2, 7, and 8, is:

Band Center = 640 nm +/- 6nm

Band Width = 80 nm +/- 6 nm
Lmax = 718 Wm-2sr-1um
Ltyp = 23 Wm-2sr-1m-1
SNR @ Ltyp = 119 (specification)
SNR @ Ltyp = 159 (performance)

SNR margin has been reduced from 40% to 33%. This is considered to be an acceptable risk by Raytheon.

2.2.2 Operational Benefits

Important operational benefits of Visible-Infrared imagery are outlined by Mannen (1996) and in the NPOESS Integrated Operational Requirements Document (IORD). These include general forecasting, ice/ocean analysis, weapons systems support, safety of operations, hazard identification/warnings, and navigation/trafficability. The operational objectives of the Imagery EDR are discussed in Sections 2.4.3 (Clouds) and 2.4.6 (Sea Ice).

2.3 NEAR CONSTANT CONTRAST (NCC) VISIBLE IMAGERY

The Imagery EDR includes a daytime/nighttime visible imagery product that maintains apparent contrast under daytime, nighttime, and terminator region illumination conditions. This product, referred to as the Near Constant Contrast (NCC) visible imagery, is to be derived from the daytime/nighttime visible band (DNB) in addition to the calibrated DNB radiances and reflectances. Data from the daytime/nighttime band will be transmitted in the real-time Low Rate Data (LRD) stream, and the NCC visible imagery will be made available to users in near real time following the ground processing needed for its generation. In addition to derived requirements for this product, NCC visible imagery is subject to the following five explicit requirements:

1) The NCC visible imagery shall minimize the apparent transition across the terminator when it is viewed on a graphical display system. This means, in particular, that from the perspective of a human analyst viewing the imagery, the apparent image contrast is maintained across the imagery, and that there are no spatial or other artifacts which adversely affect the utility of the imagery.

2) The HSR of the NCC visible imagery shall meet the HSR requirement of the daytime/nighttime visible band.

3) The HRI of the NCC visible imagery shall be constant to within 5% of its nominal value in both the in-track and cross-track directions within a swath. This requirement does not apply to the horizontal sampling performed by the VIIRS instrument, and may be met by resampling the measured data.

4) The nominal value of the HRI of the NCC visible imagery shall provide gapless or near gapless coverage based on the minimum HSR in either the in-track or cross-track directions across the imagery swath.

5) The NCC visible imagery shall be geolocated by ground processing to meet the mapping uncertainty requirement.

2.4 APPLICATION-RELATED REQUIREMENTS

The content and quality of the imagery shall be adequate to allow certain application-related requirements to be met. These requirements determine the derived requirements of Horizontal Reporting Interval, Measurement Range, and Measurement Uncertainty for the VIIRS imagery bands.

The content of the application-related data products (ARPs) is not part of the content of the imagery EDR, and there is no system requirement to develop algorithms to produce them. However, there was a need for requirements flowdown to explicit imagery requirements that was best met by the development of algorithms to simulate the system performance in producing the ARPs. As a result, we are able to document the theoretical basis and performance of these algorithms as an added benefit of our system solution to the VIIRS requirements.

The application-related requirements apply to manually generated cloud data and to sea ice data

Manually generated cloud data are estimates of cloud cover and cloud type generated by a trained human analyst viewing the unprocessed and/or processed imagery derived from the unprocessed imagery, e.g., by data fusion, spatial rescaling, image enhancement, etc. Data products include cloud cover and cloud type.

Sea ice data may be generated interactively by a trained human analyst viewing unprocessed or processed imagery at a computer workstation, or automatically via an algorithm. Data products include ice edge location and ice concentration. In addition, analysts will attempt to determine the thickness and size of leads and polynyas based on the imagery.

2.4.1 Requirements for Cloud Cover

Cloud cover is defined as the fraction of a given area, i.e., of a horizontal cell, on the Earth's surface for which a locally normal line segment, extending between two given altitudes, intersects a detectable cloud. A detectable cloud is defined in the SRD Glossary as "an aqueous aerosol having a vertical extinction optical depth exceeding 0.03 (TBR) in the visible or a contrast with the background exceeding 0.02 (TBR) in the visible." For manual analyses, cloud cover is estimated for a single atmospheric layer. Specifically, the minimum and maximum altitudes of this layer are defined to be the surface of the Earth and the altitude where the pressure is 0.1 mb. Haze, smoke, dust, and rain are not to be considered clouds. For the purpose of validating this requirement, cloud cover estimates are to be generated by a trained human analyst viewing unprocessed and/or processed imagery for contiguous square areas having side length equal to the horizontal cell size specified below.

The SRD requirements for manual analysis of cloud cover are summarized in Table 3.

Table 3. Specifications for the VIIRS Cloud Cover Imagery ARP

Para. No.		Thresholds	Objectives	Specification Value
V40.2.3.2-1.1-6	a. Horizontal Cell Size	3 (TBR) times the Imagery HSR	2 times the Imagery HSR	3 times the Imagery HSR
V40.2.3.2-1.1-3	b. Horizontal Reporting Interval	Horizontal Cell Size	Horizontal Cell Size	Horizontal Cell Size
V40.2.3.2-1.1-4	c. Measurement Range	0 – 1, 0.1 increments	0 – 1, 0.1 increments	0 – 1, 0.1 increments
V40.2.3.2-1.1-5	d. Measurement Uncertainty	0.1	0.1	0.1

2.4.2 Requirements for Cloud Type:

Cloud types are defined as follows:

(1) Altocumulus (AC)

(2) Altocumulus Castellanus (ACCAS)

(3) Altocumulus (Standing lenticular) (ACSL)

(4) Altostratus (AS)

(5) Cirrocumulus (CC)

(6) Cirrocumulus (Standing lenticular) (CCSL)

(7) Cirrostratus (CS)

(8) Cirrus (CI)

(9) Cumulonimbus (CB)

(10) Cumulus (CU)

(11) Cumulus Fractus (CUFRA)

(12) Towering Cumulus (TCU)

(13) Stratus Fractus (STFRA)

(14) Nimbostratus (NS)

(15) Stratocumulus (SC)

(16) Stratocumulus (Standing lenticular) (SCSL)

(17) Stratus (ST)

The Cumulonimbus mama (Mammatocumulus) (CBMAM) cloud type requirement has been deleted from the SRD. Cloud typing not only entails a capability to distinguish between clouds of different type, but also a capability to distinguish clouds from other features, such as snow, cold water, cold land, haze, smoke, dust, etc. Therefore, the following additional types are defined:

(18) Obscured/not cloudy

(19) Clear

A given area is classified as "obscured/not cloudy" if there are no detectable clouds within the atmosphere overlying the area and if the average vertical loss of signal (LOS) extinction optical thickness of the atmosphere overlying the area is > = 0.03 in the 0.4-0.7 µm band. A given area is classified as "clear" if there are no detectable clouds, as defined above, overlying the area and if the average vertical LOS extinction optical thickness of the atmosphere overlying the area is < 0.03) in the 0.4-0.7 µm band. Note that other EDRs require the type of non-cloud obscuration to be discerned and identified, e.g., smoke, dust, sand, ash, etc.

For the purpose of validating this requirement, typing is to be performed by a trained human analyst viewing unprocessed and/or processed imagery for contiguous square areas having side length equal to the horizontal cell size specified below. The probability of correct typing is defined as the probability that a cell reported as being of type x is in fact of type x, where x is any of the types specified above.

The SRD requirements for manual analysis of cloud type are summarized in Table 4.

Table 4. Specifications for the VIIRS Cloud Type Imagery ARP

Para. No.		Thresholds	Objectives	Specification Value
V40.2.3.2.1.2-7	a. Horizontal Cell Size	(TBD) times Imagery HSR	(TBD) times Imagery HSR	3 times Imagery HSR
V40.2.3.2.1.2-3	b. Horizontal Reporting Interval	Horizontal Cell Size	Horizontal Cell Size	Horizontal Cell Size
V40.2.3.2.1.2-4	c. Measurement Range	Clear, Obscured/not cloudy, ST,CU,CI	Clear,obscured/not cloudy, all 17 cloud types	Clear, obscured/not cloudy, ST,CU, CI , plus 10 additional cloud types*
V40.2.3.2.1.2-8	d. Probability of Correct Typing	85% at (TBS**) % confidence level	90% at (TBS**) % confidence level	85%

* Altocumulus (AC), Altocumulus (Standing Lenticular) (ACSL), Altostratus (AS), Cirrocumulus (CC), Cirrocumulus (Standing lenticular) (CCSL), Cirrostratus (CS), Cumulonimbus (CB), Towering cumulus (TCU), Stratocumulus (SC), Stratocumulus (Standing lenticular) (SCSL)

** To Be Specified

2.4.3 Operational Objectives of Manually-Generated Cloud Data

2.4.3.1 Introduction

Historically, imagery-based cloud cover analysis at the Air Force Weather Agency (AFWA) supported Air Force Precedence 1-1 Programs. The required cloud analyses had to be performed upon receipt of Defense Meteorological Satellite Program (DMSP) data in minimum time. The sequence of steps in the cloud analysis and forecast process included:

1) Data ingestion functions:
    a) Processing imagery by the satellite processing mainframe computer
    b) Processing the imagery into the Satellite Data Handling System (SDHS)

Generation of Automated Cloud Analysis

    c) Generation of cloud analysis by the Automated Real Time NEPH analysis (RTNEPH) Model
    d) Manual Quality Control (QC) of the RTNEPH analyses (called “RTNEPH Bogus”)

2) Generation of Automated Cloud Forecasts
    e) ADVCLD (Five-Layer) long range forecast model (+03 to +33 hours)
    f) HRCP (High-Resolution Cloud Prognosis) short range cloud forecast model
    g) Manual QC of Forecast Products (called “Forecast Bogus”)

The entire process was nominally accomplished within a 55 minute timeline. The clock was started when the DMSP spacecraft reached a command readout site and began replaying recorded data. Data ingestion typically required 2-3 minutes. Automated cloud analysis was accomplished in another 5 minutes. Preparation for the RTNEPH Bogus occasionally began prior to data readout (e.g., pre-mapping grid coordinates to satellite image space). The manual QC (Bogus) process was allocated 15 minutes, with generally two quarter orbits of data being processed in parallel. At Bogus completion, approximately +22 minutes, RTNEPH edits were sent to the satellite processing mainframe to update the RTNEPH database. This database was used to initialize the various forecast models. Output cloud cover forecasts were displayed on the SDHS over the DMSP imagery alongside ancillary forecast aids (e.g., height, temperature, and moisture fields) and reviewed for correctness by forecasters. Forecast edits were retransmitted to the satellite processing mainframe for database update and final forecast product generation.

2.4.3.2 The Current QC System

The RTNEPH Bogus on the SDHS is still accomplished by displaying only two DMSP channels of smooth (1.5 nautical miles) broadband infrared and visual imagery for a quarter-orbit of data simultaneously on two monitors at 1024x1024 resolution in the nominal satellite projection. As many as four sets of these displays are ‘scanned’ in sequence from the northernmost to the southernmost sections of the quarter-orbit. A third monitor displays a 4:1 reduced view of the entire quarter orbit to provide the analyst with an overview of the entire scene. On the high resolution monitors, digits are displayed over the imagery at RTNEPH grid point locations to

represent the automated cloud cover analysis. Only total cloud amount, in eighths, is displayed. All other parameters are currently ignored. Cloud cover of zero eighths is not displayed to emphasize distinctiveness of clear-cloud regions. Because digits are spaced closely in image space (typically no more than 16 pixels from center to center), a special character set is used to display digits with a minimum number of pixels. Additionally, the capability to toggle digits on or off rapidly is available.

Analysts use a multiple monitor slaved draw mode with a digitizing tablet to circumscribe cloud edits around sets of digits which are deemed unrepresentative of the true cloud field. Each single cloud edit label takes the form of a closed curve and may include up to three pairs of cloud amount and cloud type; one each for low, middle and/or high clouds. For example, one Bogus label might include 3 eighths of cumulus, 5 eighths of altocumulus, and 6 eighths of cirrus. More typical an edit label involves only a single cloud layer. Analysts generally estimate lower altitude cloud amounts based on their meteorological understanding of the situation. The RTNEPH bogus edit post-processor uses cloud type labels to assign default cloud base and top altitudes.

The imagery is pre-processed to maximize the dynamic range of pixel brightness using local histogram frequency equalization. This technique allows analysts to discriminate clouds from the known (learned by experience and through studying detailed maps) physiographic background. For example, using only DMSP data, low cloud at night are readily discriminated from cold background terrain (so called black-stratus) by the obscuration of terrain features such as low ridgelines, valleys, and rivers. However, the value of these precise cloud edge specifications is generally lost when analyses are ingested into the lower (25 nm) resolution RTNEPH grid.

After a review of the displayed 1024x1024 frame for the quarter orbit is complete, another analyst performs a “quick” review of the edits; then, QC of the next frame of the quarter orbit begins. The QC time schedule only allows the analyst approximately 2-3 minutes per 1024x1024 frame to ensure that a single quarter-orbit is processed within the required timeline. At the end of the allotted time or when the quarter orbit is completely reviewed, all edits are concatenated and shipped to the satellite processing mainframe to update the database. A hardcopy of the edits is generated and filed for subsequent review. Given the typical 15 minute time budget to review and correct a quarter orbit cloud analysis, the analysts typically are reviewing and correcting 1.5 million square kilometers per minute.

2.4.3.3 Manually-Generated Products During the NPOESS Era

The integration of NPOESS data in general, and VIIRS data in particular, will significantly improve the cloud analysis and forecast system at AFWA. While no attempt is made, at this point, to define an architecture for using these data in AFWA or any other Government facility, there are obvious benefits from using VIIRS in the automated cloud analysis and forecast system at AFWA. These enhancements include:

1. The use of VIIRS imagery will significantly improve the quality of automated cloud analyses, resulting in fewer operations being needed to perform the QC, Bogus function. Earlier studies quantified the accuracy of the cloud forecast system at AFWA and

recommended further improvements in the cloud analysis and forecast system (Hutchison and Janota, 1989; Hutchison et al., 1990). Recommended enhancements were made to the cloud forecast models and subsequently the time required to perform QC on the automated cloud forecasts became negligible. These studies also stated that "After the recommended enhancements to cloud forecast models were made, the next major step necessary to improve the cloud forecast accuracy was to upgrade the cloud analysis model." Subsequently, the Support of Environmental Requirements for Cloud Analysis and Archive (SERCAA) Program was undertaken to improve automated cloud analyses; however, these algorithms must continue to rely upon existing meteorological satellite DMSP, Television Infrared Observation Satellite (TIROS), and Geostationary Operational Environmental Satellite (GOES) data which have inadequate spectral data for generating highly accurate, global cloud analyses. Therefore, significant improvement in cloud detection accuracy will be possible with the added spectral data acquired by VIIRS, as discussed in the VIIRS Cloud Mask ATBD *[Y2412]*, and improved automated cloud analyses will result after the cloud forecast system in AFWA is upgraded to process these NPOESS data.

2. The use of VIIRS imagery and imagery assist channels will provide analysts with the capability to more readily distinguish between clouds and cloud-free surfaces, using color composites, which will significantly improve the speed and the accuracy of the QC, Bogus process. As noted earlier, RTNEPH Bogus on the SDHS is accomplished by displaying only two AVHRR channels simultaneously on two monitors to view clouds in a gray-scale image. During the NPOESS era, at a minimum, it is recommended that all current SDHS terminals be upgraded to display VIIRS imagery as color composites (i.e. different VIIRS imagery channels, imagery assist channels, channel differences, and/or channel ratios assigned to each gun of a color display) to exploit the unique spectral signatures of cloud and backgrounds and enhance the analysts capability to quickly and accurately perform the QC process on automated cloud analyses. As experience is gained in using and interpreting these color composites, it may be possible to automate the cloud analysis specification to the point that only occasional manual tunings will be required. Examples of VIIRS color composite are shown in Section 3.4.

3. During the NPOESS era, it is recommended that enhanced software be provided to avoid the need for analysts to estimate lower altitude cloud amounts based solely on their meteorological understanding of the situation. This should be readily achieved using VIIRS automated cloud products, such as the improved Cloud Top Height EDR, Cloud Base Height EDR, and Raytheon's multi-layered cloud EDR with physiographic maps available in SDHS-type terminals. These maps should also include VIIRS-derived land classification (forests, deserts, grasslands, etc.), terrain elevation, all land/water boundaries (rivers, in-land lakes, etc), and major roadways.

4. During the NPOESS era, significant improvements will be realized in the retrieval of atmospheric profiles. While it is uncertain how these profiles might be used in weather centrals, (e.g. where numerical weather prediction models generate fields which may be used in the automated cloud analysis), these profiles will have value for automated cloud analyses at locations that do not run numerical models, e.g. field sites.

5. The quality of manually generated cloud products will always depend on the ability of the analyst. Our flowdown of requirements and assessment of performance has been made under the assumption that the analysts in the NPOESS era will have the benefit of training that includes VIIRS-specific instruction. The current DMSP OLS and TIROS AVHRR sensors have limited spectral content compared to the VIIRS sensor designed by Raytheon. While the National Aeronautics and Space Administration's (NASA) Moderate Resolution Imaging Spectroradiometer (MODIS) will provide the research community with a significantly enhanced capability, the operational community will not fully realize the value of these data until the launch of the NPOESS VIIRS sensor. In the interim, research scientists will continue to improve the algorithm technology and MODIS-derived environmental data products (EDRs). Thus, it becomes essential that the algorithm technology and user knowledge be brought forward together in order to fully realize the value of true multispectral VIIRS measurements. We have included an outline of a suggested VIIRS User's Guide for cloud analysts as an Appendix to this document.

Stratus/fog/snow discrimination is an important operational benefit of manual cloud analysis (Mannen, 1996; IORD-I). Stratus detection, a threshold requirement for Cloud Type, is discussed in Section 3.4.3.4. Stratus/snow discrimination is also discussed in Section 3.4.3.4. Fog detection is not a VIIRS requirement, so we do not have a specification or performance analysis for it. However, fog is physically equivalent to a low-lying stratus cloud. An analyst can discriminate fog from stratus with the assistance of the VIIRS cloud top EDRs (Cloud Top Temperature, Cloud Top Pressure, Cloud Top Height), which can be available as VIIRS ancillary data for the VIIRS Imagery Cloud Data.

2.4.4 Requirements for Ice Edge Location

An ice edge is defined as the boundary between ice-covered sea water (ice concentration > 0.1) and sea water not covered by ice (ice concentration < 0.1). The ice edge generally occurs between the ice free ocean and the contiguous pack ice, although complex patterns of ice concentration may be found, defying such simple interpretations. The advance and retreat of the ice edge during the annual cycle creates a seasonally migrating marginal zone between the open ocean and the contiguous pack ice. This zone influences atmospheric and oceanic circulation, affecting the development of local and regional weather patterns. In addition, the ice edge can move tens of kilometers per day, significantly disrupting operational activities on the sea surface. Ice edge boundaries are used for navigational planning, and so must be available in a short time. The value of an automated retrieval is indicated by the fact that changes in boundaries are typically on short time scales.

An ice edge is typically provided as a contour on a map or in digital form as a set of latitude/longitude coordinates. The ice edge location error is defined as the distance between the estimated location of an ice edge and the nearest location of a true ice edge.

Our automated algorithm produces ice edge location as a binary edge/no edge map at the imagery pixel resolution and also as a set of latitude/longitude edge coordinates. The coordinates are derived at subpixel resolution from interpolation of the ice concentration map.

The requirements for sea ice edge location are summarized in Table 5.

Table 5. Specifications for the VIIRS Ice Edge Location Imagery ARP

Para. No		Thresholds	Objectives	Specification Value
V40.2.3.2.2.1-1	a. Horizontal Coverage	North of 36 deg north latitude, south of 50 deg south latitude for sea ice.	North of 36 deg north latitude, south of 50 deg south latitude for sea ice.	North of 36 deg north latitude, south of 50 deg south latitude for sea ice.
V40.2.3.2.2.1-2	b. Measurement Range	Any latitude, longitude within coverage domain	Any latitude, longitude within coverage domain	Any latitude, longitude within coverage domain
V40.2.3.2.2.1-3	Measurement Uncertainty	(TBD)	(TBD)	0.4 km at nadir, 1.0 km worst case

Ice edge locations from passive microwave have uncertainties of approximately 10 km. VIIRS imagery retrieval of ice edge location represents a significant improvement over passive microwave.

2.4.5 Requirements for Ice Concentration

Ice concentration is defined as the fraction of a given area of sea water covered by ice. It is typically derived from imagery and reported on ocean geographical charts for areas between contours generated by an analyst. For the purpose of verifying the measurement uncertainty requirement, ice concentration is reported as a gridded product for areas of size limited by the HCS requirement and separation limited by the HRI requirement. Ice concentration is reported at imagery resolution with measurement uncertainty better than 0.1 in most cases. Optimized parameters of a search window and band weight reduce tie point errors and provide a seamless day/night transition.

The various sea ice centers produce ice concentration products. The advent of a series of visible-infrared sensors with automated cloud masking capability, including AVHRR-3, MODIS, and Global Imager (GLI), is raising expectations in the sea ice operational community.

The ice concentration Measurement Uncertainty requirement, included in the Version Two, revision a of the Sensor Requirements Document, cannot be met if sea ice data are manually generated by ice analysts. We have developed algorithms that can be used in an operational environment to retrieve sea ice data automatically.

In the expectation that automated ice concentration retrievals from visible-infrared radiometry will be a developing capability over the next decade, we are providing an automated algorithm to retrieve ice concentration from VIIRS imagery bands.

The algorithm includes the derivation of ice fraction for imagery pixels, using tie point analysis of ice surface temperature and/or surface reflectance. Ice concentration is retrieved as a gridded product at imagery resolution with measurement uncertainty better than 0.1 in most cases. The algorithm is described in Section 3.5.

The SRD requirements for sea ice concentration are summarized in Table 6.

Table 6. Specifications for the VIIRS Ice Concentration Imagery ARP

Para. No		Thresholds	Objectives	Specification Value
V40.2.3.2.2.2-4	d. Horizontal Cell Size (at nadir)	2 km	1 km	0.8 km
V40.2.3.2.2.2-5	e. Horizontal Reporting Interval	(TBD)	(TBD)	Imagery HSR (0.4 km at nadir, 0.8 km worst case)
V40.2.3.2.2.2-1	a. Horizontal Coverage	North of 36 deg north latitude, south of 50 deg south latitude for sea ice	North of 36 deg north latitude, south of 50 deg south latitude for sea ice	North of 36 deg north latitude, south of 50 deg south latitude for sea ice
V40.2.3.2.2.2-2	b. Measurement Range	0 – 1, 0.1 increments	0 – 1, 0.1 increments	0 – 1 full continuous range
V40.2.3.2.2.2-3	c. Measurement Uncertainty	0.1	0.1	0.1

2.4.6 Operational Objectives of Sea Ice Data

We use automated algorithms, described in Section 3.5 of this document, to derive sea ice edge location and sea ice concentration. Analysts at ice centers will be able to use our sea ice retrieval, either as a standalone product, or as a time-saving starting point for manual analysis. Both options are intended to allow for the processing of larger amounts of data, by relieving the load on the analysts. The development of fully automated algorithms is critical to the plans of operational ice centers in the NPOESS era. For example, the National Ice Center (NIC) will be responsible for the development of a global, daily strategic ice product. During an IPO sponsored visit to NIC, we were told that the role of automated algorithms in the creation of this product will be “huge”. We envision an operational process whereby analysts assimilate our ice product with other data sources at ice centers.

Operational sea ice products are needed for surface and sub-surface navigation in polar regions, and for commercial navigation in coastal zones and fisheries during ice seasons.

The polar oceans comprise approximately 6.5 percent of the Earth’s surface, and are covered by sea ice at some time during the course of the annual cycle. At its maximum extent, sea ice blankets ~19 x 10^6 km^2 of the Southern Hemisphere and ~14 x 10^6 km^2 of the Northern Hemisphere. In the Arctic, nearly half of the late-winter maximum of sea ice cover survives the summer melt season and is classified as Old ice. The net export of Multi-year sea ice through the Fram Strait is balanced by production of Multi-year ice in the Arctic basin. In the Antarctic, more than 90 percent of the sea ice found at the time of maximum extent in the late austral winter is

formed, grows, and completely melts during the annual cycle, and as such is classified as First Year ice.

Remote sensing of long-term trends in the extent of the polar sea ice pack can be a valuable indicator of global climate change. This is particularly true for polar regions, which are believed to be sensitive to global warming, and are too remote for comprehensive *in situ* monitoring.

Linear discontinuities in ice cover (leads, cracks) are typical features of its structure in winter. These features are important, influencing thermodynamic and dynamic processes in ice cover as well as tactical operations of vessels and submarines. In particular, a system of leads can be used for effective navigation in high latitudes. In addition, information on discontinuities in ice cover can be used to verify numerical models of ice cover. Operational preparation of ice charts with information on lead distribution are of scientific and operational interest. Although they are smaller than polynyas, leads are usually more important in the energy balance of polar regions, because they are much more numerous.

The formation of each individual discontinuity, its size, and its location, is random. But all discontinuities together as a statistical ensemble are not random and can be described mathematically. A statistical description of leads incorporates the following set of characteristics:

- relative area (lead fraction)
- distribution of orientation
- distribution of length
- distribution of width
- distribution of distance between leads

The density of leads and their orientation are closely related with characteristics of large-scale deformations in ice cover, caused by wind and coastline effects. The process of lead formation and evolution can be described mathematically. A combination of observed lead characteristics with simulations of a mathematical model is a good prospect for NPOESS operational work.

Lead characteristics can be retrieved by trained analysts viewing Imagery with sufficiently good HSR and SNR. The HSR requirement is driven by the distribution of lead width. Sensors with better HSR invariably detect more leads, suggesting that the number of leads increases with decreasing width.

Our specification for Imagery HSR (c.f. Table 2) is an advance over AVHRR capability, and is roughly comparable to OLS capability and MODIS capability.

Polynyas also play an important role in the energy balance of polar regions. Polynyas are readily detectable by a human analyst as regions of contrast in either visible or thermal bands. Contrast in visible bands is caused by differences in surface reflectance between the pack ice and the polynya. Contrast in thermal bands is primarily due to differences in surface temperature between the pack ice and the polynya. Detection of polynyas is much easier than detection of

leads, and places no special demand on either the ice concentration measurement uncertainty or the HSR of the Imagery bands.

2.5 INSTRUMENT CHARACTERISTICS

The VIIRS instrument can be pictured as a convergence of three existing sensors, two of which have seen extensive operational use at this writing.

The Operational Linescan System (OLS) is the operational visible/infrared scanner for the Department of Defense (DoD). Its unique strengths are controlled growth in spatial resolution through rotation of the ground instantaneous field of view (GIFOV) and the existence of a low-level light sensor (LLLS) capable of detecting visible radiation at night. OLS has primarily served as a data source for manual analysis of imagery. The Advanced Very High Resolution Radiometer (AVHRR) is the operational visible/infrared sensor flown on the National Oceanic and Atmospheric Administration (NOAA) Television Infrared Observation Satellite (TIROS-N) series of satellites (Planet, 1988). Its unique strengths are low operational and production cost and the presence of five spectral channels that can be used in a wide number of combinations to produce operational and research products. In December 1999, the National Aeronautics and Space Administration (NASA) launched the Earth Observing System (EOS) morning satellite, *Terra*, which includes the Moderate Resolution Imaging Spectroradiometer (MODIS). This sensor possesses an unprecedented array of thirty-two spectral bands at resolutions ranging from 250 m to 1 km at nadir, allowing for unparalleled accuracy in a wide range of satellite-based environmental measurements.

VIIRS will reside on a platform of the National Polar-orbiting Operational Environmental Satellite System (NPOESS) series of satellites. It is intended to be the product of a convergence between DoD, NOAA and NASA in the form of a single visible/infrared sensor capable of satisfying the needs of all three communities, as well as the research community beyond. As such, VIIRS will require three key attributes: high spatial resolution with controlled growth off nadir, minimal production and operational cost, and a large number of spectral bands to satisfy the requirements for generating accurate operational and scientific products. A description of the design concept, scanning method, and pixel formation is given in Section 3.2.5.

The VIIRS sensor specification is based on the sensor requirements of the National Polar-orbiting Operational Environmental Satellite System (NPOESS) and on EDR thresholds and objectives. These system-level requirements have been flowed down into a fundamental set of "sensing" requirements that form the basis for the VIIRS imagery (Hutchison, 1998). The Imagery algorithm takes as input Raw Data Records (RDRs) generated from the VIIRS Imagery bands *[Y2478]*. The RDRs will be geolocated and calibrated to produce TOA radiance Sensor Data Records (SDRs), as discussed in Sections 2.6.1 and 3.2.5**.** The Explicit Imagery is obtained from these SDRs and stored in the Imagery EDR. The performance characteristics of the imagery and imagery-assist bands, listed in Table 7 and Table 8, are obtained from the VIIRS Sensor Specification Document *[PS 154640-101]* and the VIIRS Radiometric Calibration ATBD *[Y3261]*.

Table 7. Imagery EDR – Input Data Summary (Spatial)

λ(μm)	Δλ(μm)	GSD* (m) at Nadir (Track x Scan)	HSR (m) at Nadir (Track x Scan)	GSD *(m) at Edge of Scan (Track x Scan)	HSR (m) at Edge of Scan (Track x Scan)
0.7**	0.40	742 x 742	742 x 742	742 x 742	742 x 742
0.412****	0.020	742 x 262	742 x 786	1600 x 1600	1600 x 1600
0.640**	0.080	371 x 131	371 x 393	800 x 800	800 x 800
0.865****	0.039	371 x 131	371 x 393	800 x 800	800 x 800
1.61****	0.06	371 x 131	371 x 393	800 x 800	800 x 800
3.74***	0.38	371 x 131	371 x 393	800 x 800	800 x 800
11.45**	1.90	371 x 131	371 x 393	800 x 800	800 x 800

* Ground Sample Distance
** Explicitly required bands
***Additional band required to meet Imagery application-related threshold requirements
****Bands used to enhancement performance of application-related products

Table 8. Imagery EDR – Input Data Summary (Radiometric)

λ(μm)	Δλ(μm)	Ltyp (Watts/m2-sr-um) or Ttyp	SNR / NEdT (Nadir)	SNR / NEdT (Edge of Scan)
0.7*	0.4	4.E-9 Watts/cm2/sr (night), 1.E-2 Watts/cm2/sr (day)	30 (night), 600 (day)	7 (night), 200 (day)
0.410***	0.020	44.9	843	487
0.640*	0.080	23.0	275	159
0.865***	0.039	25.0	389	225
1.61***	0.06	7.3	135	78
3.74**	0.38	270 K	0.53 K	0.92 K
11.45*	1.90	210 K	0.40 K	0.69 K

* Explicitly required bands
** Additional band required to meet Imagery application-related threshold requirements
*** Bands used to enhancement performance of application-related products

The radiometric performance of the bands exceeds the specification for Measurement Uncertainty (c.f. Table 2) with margins that allow the performance of the Application-Related Products to meet or approach objective requirements (c.f. Sections 3.4.4 and 3.5.4).

2.5.1 Daytime/Nighttime Visible Band (DNB)

The Daytime/Nighttime Visible band (DNB) is explicitly required by the VIIRS SRD.

DNB data is taken by a sensitive, very-wide-dynamic range Charge-Coupled Device (CCD) detector in the main VIIRS Sensor. The CCD is located adjacent to the Visible/Near Infrared (VNIR) detector chip on the Warm Focal Plane. It is positioned so that as the sensor scans the image of the Earth across the focal plane, a particular point on earth will be imaged first by the VNIR chip and then by the DNB CCD.

The detective elements of the DNB CCD are 15.4 micrometer by 24.2 micrometer photosites. In the VIIRS sensor each of these photosites images an angle that corresponds to approximately 17 x 11 meters on the ground at nadir. The signals from many of these photosites are combined on the CCD chip to create the analog signals corresponding to entire ground pixels.

To encompass the extreme radiometric dynamic range of day and night scenes, the DNB CCD includes four regions of light-sensitive photosites with three different sensitivities:

Most Sensitive Regions: The CCD includes 2 identical regions incorporating 250 subpixel detectors operated in Time Delay Integration (TDI) mode. TDI gives a total effective integration period 250 times longer than the integration period of a single subpixel detector, and thus increases sensitivity by nearly 250 times. In normal circumstances the signals from these two identical maximum-sensitivity detector regions are added together for further improvement in SNR. However, if radiation should compromise the value of a pixel measurement made by one of the two segments, the corresponding pixel signal from the other segment would be used.

Medium-sensitivity region: A second detecting region on the CCD chip utilizes three subpixel detectors in TDI. This region also has a lower amplifier gain to give it a net radiometric gain that is approximately 200 times less than the gain of the most sensitive regions.

Lowest-sensitivity region: The CCD also incorporates a detecting region which does not incorporate multiple detectors in TDI. In addition, this region incorporates a 35:1 neutral-density filter and reduced amplifier gain, resulting in a radiometric gain approximately 1/475 of the medium-sensitivity region's gain.

The three regions are designed so that before a more sensitive region saturates, the next less sensitive region will have received a signal sufficient to produce an acceptable SNR. Analog signals from all three regions are converted into digital form and processed digitally to select the signal from the region offering the best SNR for each pixel.

The CCD design allows any number of subpixel elements to be aggregated into single pixels as they are read from the CCD. In the VIIRS sensor this capability will be used to generate pixels with near-rectangular sample spacing on the ground. To accomplish this, many different aggregation modes will be used during the course of the crosstrack sensor scan. Since the subpixel aggregation is an additive process, the total number of subpixels aggregated to create each pixel appears as a factor in the radiometric gain of the pixel.

2.5.2 VIIRS Imagery Band Selection Process

Bands selection for the Raytheon VIIRS sensor design is based upon the strength (strong and/or weak) of three components that make up the signatures of each feature. These component are: (a) surface radiance which includes temperature and emissivity or solar reflectivity, (b) cloud absorptivity or reflectivity, and atmospheric transmissivity. Examples of these features in several VIIRS channels are shown in Figure 2.

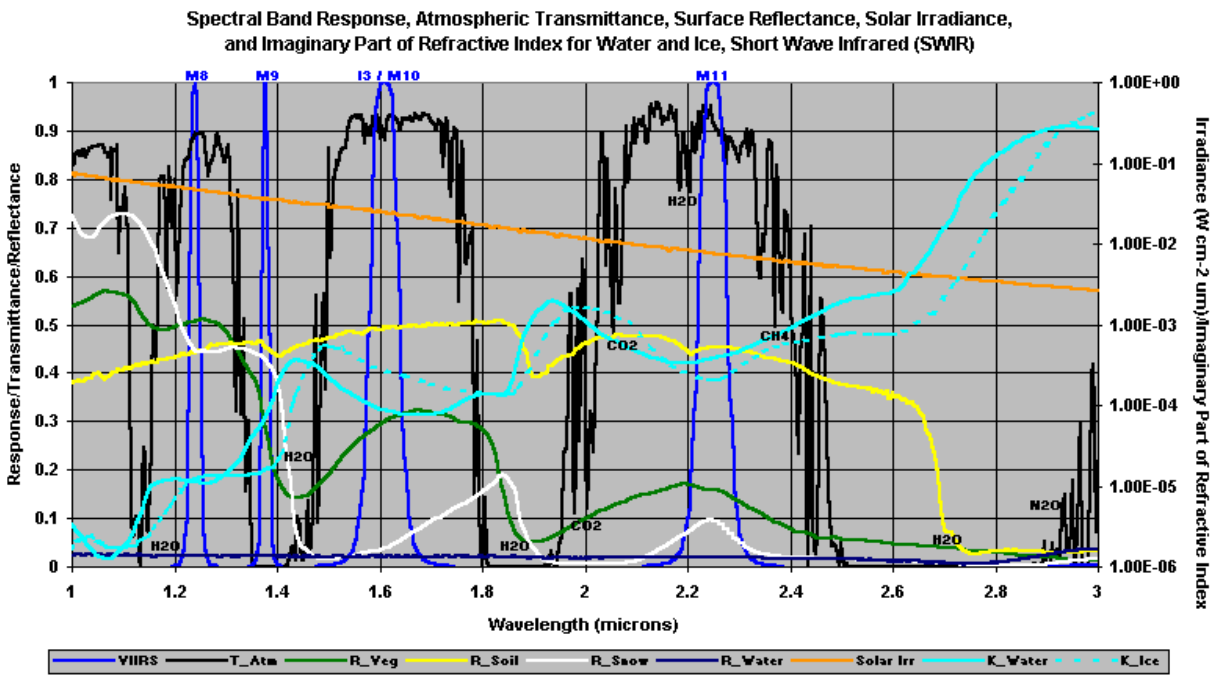

Figure 2. Reflectivity, absorptivity, and transmissivity of atmosphere, surface, and clouds in the Short-Wave Infrared (SWIR).

Figure 2 shows the band positions for VIIRS channels M8, M9, I3/M10, and M11 (---) along with atmospheric transmissivity (---), reflectivity of vegetated (---) and bare soil (---) ice (white) and water surfaces (---), solar irradiance (gold), and imaginary components of the index of refraction for water (---) and ice (---).

The positive identification of clouds in multispectral imagery requires that the analyst understand and exploit the properties of water droplets and ice crystals, along with the spectral characteristics of different backgrounds in VIIRS imagery and imagery-assist bands. A discussion of the phenomenology associated with the features follows along with the definition of bands selected to meet VIIRS threshold and objective requirements for the application-related products.

2.5.3 Daytime Visible Band (DV)

The Daytime Visible band (DV) is explicitly required by the VIIRS SRD. Unlike the DNB, the Measurement Range and Measurement Uncertainty requirements are determined by the application-related requirements on manually generated cloud data and sea ice data. Flowdown of application-related requirements to DV band requirements was performed to establish the spectral response and noise requirements for the DV band (Hutchison, 1998).

The Raytheon daytime visible imagery band (I1) is centered at 0.64 microns. The justification for this selection is shown in Figure 3.

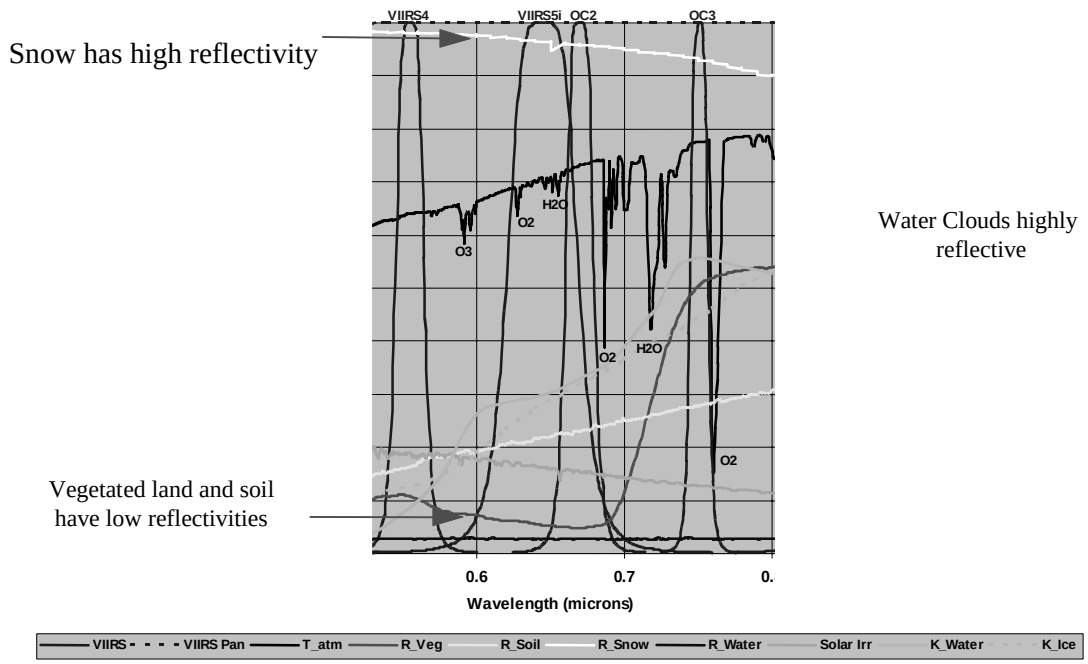

Figure 3. Phenomenology of the VIIRS Daytime Visible (DV) Imagery band, centered at 640 nm.

Figure 3 shows the location and spectral response function for the daytime visible band (I1), along with the characteristics of the Earth-atmosphere system. The band is identified in the figure by its old designation (VIIRS 5i). It is clear that the reflectivity of vegetated land is very small in this band but it begins to increase quite rapidly at ~ 0.7 microns. By limiting the long wave reponse of the band to < 0.7 microns, we also avoid the water vapor absorption lines in the 0.7-0.8 micron region which could cause variations in cloud and land signatures. The reflectivity of water surfaces is even lower. On the other hand, the reflectivity of clouds is much larger which means this band is particularly valuable for discriminating between clouds and vegetated land and ocean surfaces. Additionally, the reflectivity of snow is very high. Therefore, this channel is not good for differentiating between snow and clouds nor is it particularly useful for identifying boundaries between land and ocean surfaces.

2.5.4 Long-Wave Infrared Band (LWIR)

An infrared band is explicitly required by the VIIRS SRD. We have interpreted the requirement to be for a thermal infrared band, free of solar contamination, which we designate as the Long-Wave Infrared (LWIR). This interpretation is most consistent with OLS heritage. Unlike the DNB, the Measurement Range and Measurement Uncertainty requirements are determined by the application-related requirements on manually generated cloud data and sea ice data. Flowdown of application-related requirements to LWIR band requirements was performed to establish the spectral response and noise requirements for the LWIR band (Hutchison, 1998). The phenomenology of the 12 micron band used for flowdown is spectrally analogous to the 11.45 micron phenomenology. Therefore, the conclusions of our flowdown can be applied to the VIIRS LWIR imagery band at 11.45 microns.

The LWIR is explicitly required by the VIIRS SRD. Unlike the DNB, the Measurement Range and Measurement Uncertainty requirements are determined by the application-related requirements on manually generated cloud data and sea ice data. Flowdown of application-related requirements to LWIR band requirements was performed to establish the spectral response and noise requirements for the LWIR band (Hutchison, 1998).

Figure 4 shows the location and spectral response function for the VIIRS LWIR band (I5), along with the characteristics of the Earth-atmosphere system.

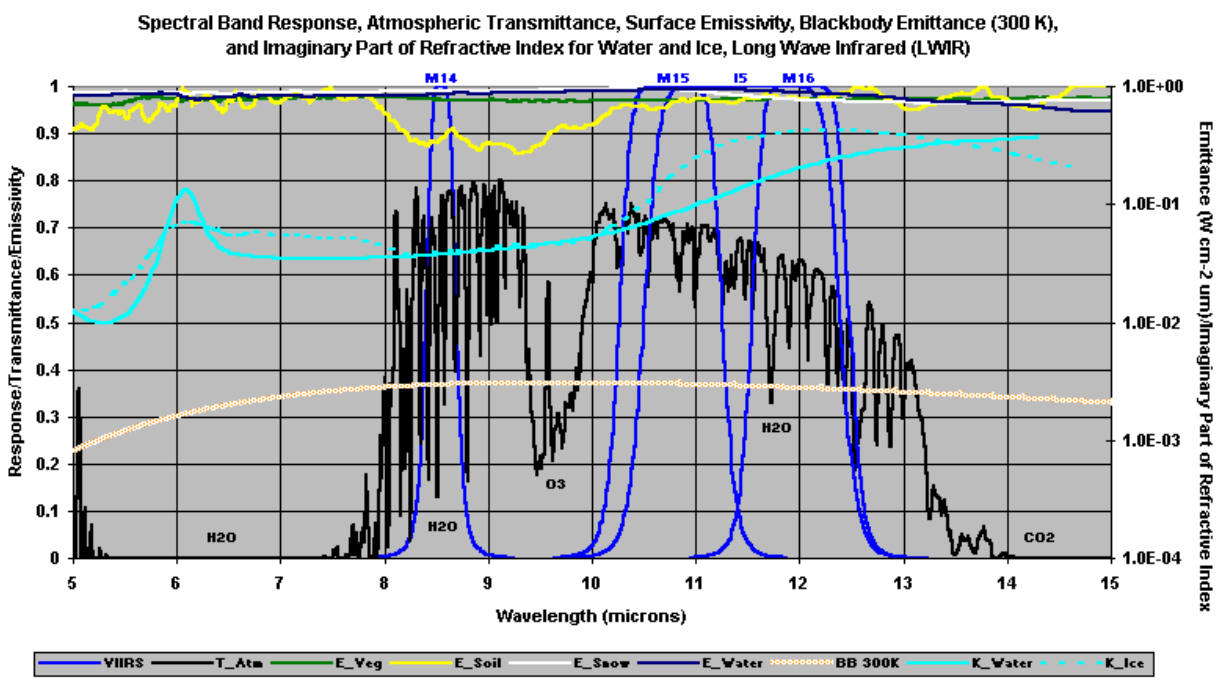

Figure 4. Phenomenology of the VIIRS Long-Wave Infrared (LWIR) Imagery band, centered at 11.45 microns.

Figure 4 shows the water vapor absorption across the LWIR band. The band is valuable for estimating the true radiating temperatures of objects in the band after correcting for atmospheric water vapor attenuation, which makes the measured cloud top temperature slightly colder than its true radiating temperature. In addition, due to the high absorptivity of ice at these wavelengths, thin cirrus is often easily detected in nighttime conditions, when VIIRS data in the 1.378 micron band are not available.

2.5.5 Mid-Wave Infrared Band (MWIR)

Flowdown of application-related requirements has resulted in the specification of an additional imagery band in the Mid-Wave Infrared (MWIR), at 3.74 microns. The band, shown in Figure 5, is needed to meet the threshold requirement for the Cloud ARPs.

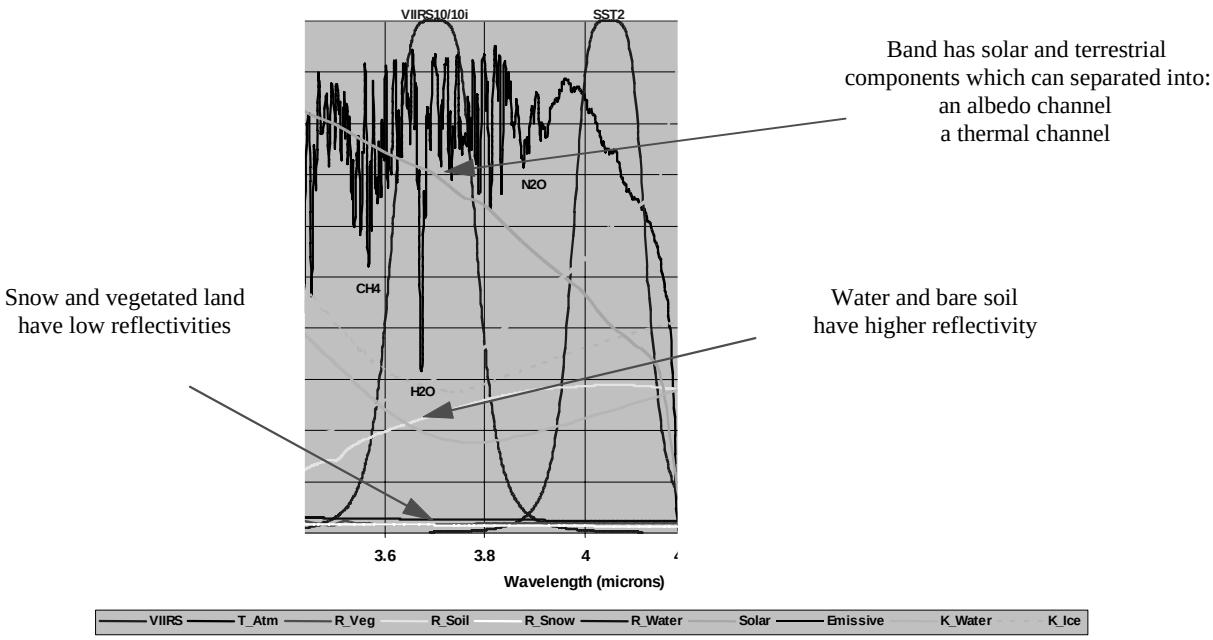

Figure 5. Phenomenology of the VIIRS Mid-Wave Infrared (MWIR) Imagery band, centered at 3.74 microns.

Figure 5 shows water vapor absorption lines in the VIIRS MWIR band (I4). The band is identified in the figure by its old designation (VIIRS 10i). The figure also shows that the reflectivity of snow is very low while that of clouds is much larger. It also shows that considerable solar irradiance is present while the reflectivity of bare soil is relatively large compared to snow and clouds. Therefore, the MWIR band could be useful for differentiating between snow and clouds as well as clouds and vegetated land. However, distinction between cloud and bare soil appears difficult and the presence of terrestrial energy complicates the contrast between snow and clouds.

The VIIRS sensor requirements for the Cloud ARPs were established using a series of simulations for the following cases.

Case 1: Stratus at Night

Case 2: Daytime and Nighttime Cirrus

Case 3: Cloud Typing (Stratus versus Cirrus)

Case 4: Cumulus

Case 5: Daytime Obscurations

The simulations assumed the minimum of number of imagery bands as required by the VIIRS SRD, i.e. one for daytime visible, one nighttime visible, and one infrared imagery band. While completing the initial set of simulations, it was determined that differentiating between nighttime stratus and cirrus clouds was not possible without the MWIR band, i.e. Case 3 results did not meet specifications. Thus, the MWIR band was added to the minimum "sensing" requirement for VIIRS imagery. With the MWIR band added, Case 1 and Case 2 were re-analyzed using the brightness temperature differences (BTD) between the MWIR and LWIR imagery bands. The addition of the bi-spectral signatures of these clouds in the BTD imagery reduced the Raytheon VIIRS sensor noise model specifications necessary to meet threshold requirements. In addition, in Case 4, the daytime MWIR imagery was broken into thermal and albedo components as described in the literature (Hutchison et al., 1997) and used to differentiate between cumulus and snow fields along with stratocumulus over deserts conditions. Cumulus clouds over other backgrounds is trivial. Finally, the simulations were completed for Case 5 to establish that an optical depth of aerosol greater than 1 is required for detection with the LWIR imagery band.

While the daytime MWIR imagery channel contains both solar and thermal energy, the capability has been demonstrated to separate this single channel into two channels and thus improve the discrimination between features in the spectral band. This process has been described in the literature (Hutchison et al., 1997). Use of the derived albedo channel significantly enhances the contrast between snow and water clouds. In fact the procedure also sufficiently enhances the contrast between snow and cirrus (ice) clouds so that snow can be observed through overcast cirrus cloudy conditions. Furthermore, the VIIRS flowdown process demonstrated that the thermal channel proves highly effective at differentiating between water clouds and bare soil. Finally, the nighttime MWIR band image can be widely used for detection and identification of nighttime stratus, especially when coupled with the VIIRS LWIR band.

2.5.6 Imagery Assist Bands

The VIIRS SRD specifies that the spectral bandpasses required to meet the threshold requirements for the manually-generated Cloud ARPs must be at the "imagery" resolution. The flowdown of these requirements determined that only three spectral bands were required to meet the threshold requirements (Hutchison, 1998). However, the Raytheon Cloud and Imagery

Integrated Product Teams (IPTs) also demonstrated the use of imagery bands with imagery-assist data, collected at a more coarse resolution, to advance toward meeting objective requirements, especially for the Cloud Type ARP. Therefore, this section begins with a discussion of the phenomenology associated with the selection of the VIIRS imagery channels in the Raytheon design. Subsequently, the phenomenology associated with non-imagery channels is presented for the bands that provide useful information for the manual detection of clouds and their classification by type.

The near infrared (NIR) band (I2) is available at the resolution of the Imagery bands, because of non-Imagery EDR requirements. It is useful to improve performance of the sea ice data application-related products (c.f. Section 3.5.4).

The short wave infrared (SWIR) band (I3) is available at the resolution of the Imagery bands, because of non-Imagery EDR requirements. It is useful as a snow-ice/cloud discriminator.

A number of VIIRS bands are useful for Red-Green-Blue (RGB) color composite cloud analysis (c.f. Section 3.4.3.4). These include the imagery resolution bands at 0.865 µm and 1.61 µm, and the moderate resolution bands at 0.41 µm, 1.38 µm, 4.05 µm, 8.55 µm, and 10.76 µm,

2.6 RETRIEVAL STRATEGY

2.6.1 Explicit Imagery

The VIIRS EV_375M and EV_DNB SDRs will be produced from the VIIRS RDRs by an RDR to SDR conversion. They will be produced as image pixels separated by the Horizontal Reporting Interval (HRI). A process of sampling and aggregation will achieve an HRI roughly equivalent to the Horizontal Spatial Resolution (HSR).

Details of this process are found in the VIIRS Sensor Specification Document *[PS 154640-101]* and the VIIRS Build SDR Module Level Software Architecture document *[Y2479]*, and will be further discussed in Section 3.2.5.

2.6.2 Top-of-Atmosphere Radiances

Calibrated top-of-atmosphere (TOA) radiances for all imagery bands will be produced in the Build-SDR module, following the system standards for VIIRS SDRs. An overview of the process is given in Section 3.2.1. A full description of the process is documented in the VIIRS Radiometric Calibration ATBD *[Y3261]*, the VIIRS Build SDR Module Level Software Architecture Document *[Y2479]* and the VIIRS Radiometric Calibration and Validation Plan *[TP 154640-118]*.

2.6.3 Top-of-Atmosphere Reflectances

Digital numbers (DNs) in the daytime visible (DV) and daytime/nighttime visible (DNB) imagery band RDRs will be converted to top-of-atmosphere reflectances, as described in the VIIRS Radiometric Calibration ATBD *[Y3261]*.

2.6.4 Equivalent Blackbody Temperatures

DNs in the Mid-Wave Infrared (MWIR) and Long-Wave Infrared (LWIR) imagery band RDRs will be converted to equivalent blackbody temperatures, as described in the VIIRS Radiometric Calibration ATBD *[Y3261]*.

2.6.5 Near Constant Contrast (NCC) Visible Imagery

The NCC visible imagery EDR will be generated from Daytime/Nighttime Visible Band (also called Day/Night Band or DNB) data. Calibrated top-of-atmosphere radiances in the 0.5-0.9μm band will be taken and converted to albedo to produce the NCC imagery. A description of the algorithm will be given in Section 3.3.

2.6.6 Manually-Generated Cloud Data

Our system solution produces radiances, reflectances, and equivalent blackbody temperatures that are sufficient for an analyst to generate the cloud data products.

2.6.7 Sea Ice Data

Automated algorithms will be used to derive ice edge location and ice concentration. The algorithms will function in the Snow/Ice Module, as an integral part of the software architecture for producing Snow/Ice EDRs as well as Imagery Sea Ice ARPs *[Y2477]*. The processing outline is described in Section 3.5.1.

Although ice edge location and ice concentration are ARPs of the Imagery EDR, similar algorithms and input data are used for the Fresh Water Ice and Sea Ice Age/Edge Motion EDRs. There is a large degree of commonality between the algorithm theoretical basis for Imagery Sea Ice ARPs and that for Fresh Water Ice *[Y2404]*. Also, the Imagery Sea Ice ARPs are required as input data to the algorithm for the retrieval of Sea Ice Age/Edge Motion EDR products *[Y2409]*.

A description of the algorithm and its data flows will be given in section 3.5.

3.0 ALGORITHM DESCRIPTION

3.1 OVERVIEW

The imagery algorithm consists of four major processing functions:

1. The Explicit Imagery process
2. The NCC imagery product process
3. The manual cloud analysis product process
4. The sea ice data product process.

3.2 EXPLICIT IMAGERY PRODUCTION

3.2.1 Processing Outline

VIIRS SDRs are computed from the VIIRS RDRs, as part of the Build-SDR module, which applies geolocation, gridding, and calibration to the RDRs. The functionality of the Build-SDR module will allow it to produce SDRs which fully meet the explicit imagery requirements. The VIIRS EV_375M SDR contains the TOA radiances for bands I1, I4, and I5, the TOA reflectances for band I1, and EBBTs for bands I4, and I5, with associated geolocation and band quality flags. The Imagery algorithm obtains this data, and writes it to an output Imagery EDR file. The VIIRS EV_DNB SDR contains the TOA radiances and TOA reflectances for the DNB. The Imagery algorithm obtains this data, and writes it to the Imagery EDR file. The process is documented in the Build-SDR Module Level Software Architecture Document *[Y2479]*, the VIIRS Radiometric Calibration ATBD *[Y3261]*, and the VIIRS Imagery Unit Level Detailed design Document *[Y3273]*.

3.2.2 Algorithm Input

The SDR algorithm requires the VIIRS RDRs for each imagery band. These RDRs are created by the ingest function of the NPOESS Interface Data Processor Segment (IDPS). The process is described in the Build-RDR Module Level Software Architecture Document *[Y2478]*. The Explicit Imagery algorithm requires the VIIRS SDRs for imagery resolution data (EV_375M) and DNB data (EV_DNB).

3.2.2.1 VIIRS Data

The required VIIRS data are the VIIRS RDRs, which contain the basic DNs to be converted into radiance or reflectance by applying calibration coefficients. The calibration coefficients themselves are stored in calibration LUTs *([Y2490], [Y3261])*.

3.2.2.2 Non-VIIRS Data

No non-VIIRS data are required for the generation of Explicit Imagery.

3.2.3 Theoretical Description

The production of TOA radiances from application of calibration coefficients, TOA reflectances, and equivalent blackbody temperatures is discussed in the VIIRS Radiometric Calibration ATBD *[Y3261]*.

3.2.4 Archived Algorithm Output

The RDR to SDR process creates TOA radiances in all imagery bands, TOA reflectances in the daytime visible and daytime/nighttime visible bands, and equivalent blackbody temperatures for the Mid Wave IR band and the Long Wave IR band. The Imagery algorithm stores these as fields in an Imagery EDR HDF file. All Explicit Imagery products shall be calibrated, geolocated, and reported for a set of earth locations forming an approximately rectangular lattice. The lattice spacing will be 742 meters +/- 5% for the DNB, and approximately equivalent to the HSR for the other imagery bands.

3.2.5 Performance of Explicit Imagery

The Explicit Imagery is obtained from the VIIRS EV_375M SDR and the VIIRS EV_DNB SDR. The SDRs are obtained from VIIRS RDRs by an RDR to SDR process. The RDRs are obtained by a rotating telescope scanning mechanism that minimizes the effects of solar impingement and scattered light. Figure 6 illustrates the design concept for VIIRS, designed and built by Raytheon Santa Barbara Remote Sensing (SBRS). VIIRS is essentially a combination of SeaWiFS foreoptics and an all-reflective modification of MODIS/THEMIS aft-optics. Calibration is performed onboard using a solar diffuser for short wavelengths and a blackbody source and deep space view for thermal wavelengths. A solar diffuser stability monitor (SDSM) is also included to track the performance of the solar diffuser. The VIIRS scan will extend to 56 degrees on either side of nadir, providing a swath of 3000 km for the nominal satellite altitude of 833 km.

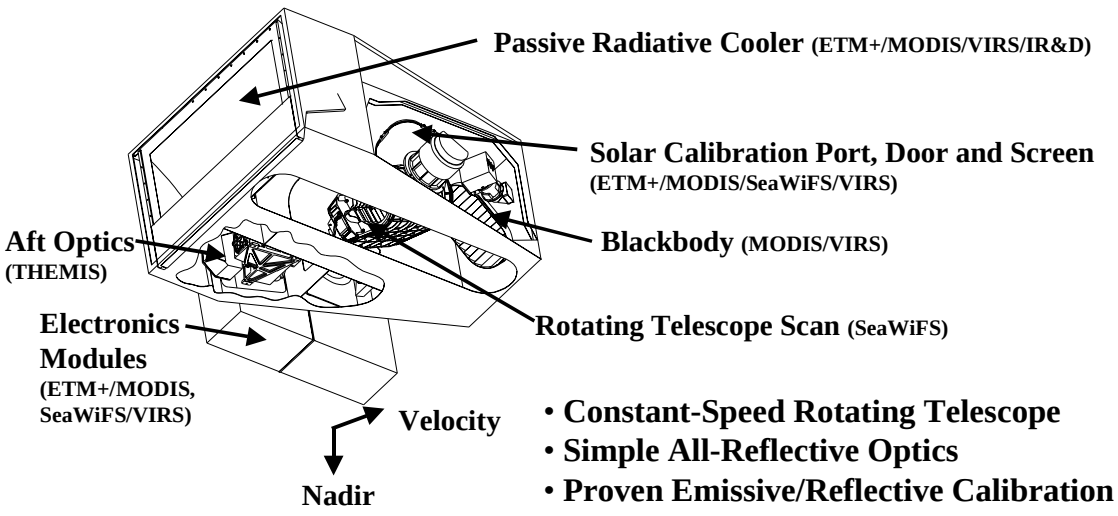

Figure 6. Summary of VIIRS design concepts and heritage.

The VIIRS SRD places explicit requirements on spatial resolution for the Imagery EDR. Specifically, the horizontal spatial resolution (HSR) of bands used to meet threshold Imagery EDR requirements must be no greater than 400 m at nadir and 800 m at the edge of the scan. This led to the development of a unique scanning approach which optimizes both spatial resolution and signal to noise ratio (SNR) across the scan. The concept is summarized in Figure 7 for the imagery (fine resolution) bands. The VIIRS detectors are rectangular, with the smaller dimension along the scan. At nadir, three detector footprints are aggregated to form a single VIIRS "pixel." Moving along the scan away from nadir, the detector footprints become larger both along track and along scan, due to geometric effects and the curvature of the Earth. The effects are much larger along scan. At 31.59 degrees in scan angle, the aggregation scheme is changed from 3x1 to 2x1. A similar switch from 2x1 to 1x1 aggregation occurs at 44.68 degrees. The VIIRS scan consequently exhibits a pixel growth factor of only 2 both along track and along scan, compared with a growth factor of 6 along scan which would be realized without the use of the aggregation scheme. This scanning approach allows VIIRS to provide imagery at 800-m resolution or finer globally, with 375-m resolution at nadir. Additionally, due to the imagery requirements for VIIRS and the "sliver" detector design, MTF performance will be extremely sharp (0.5 at Nyquist).

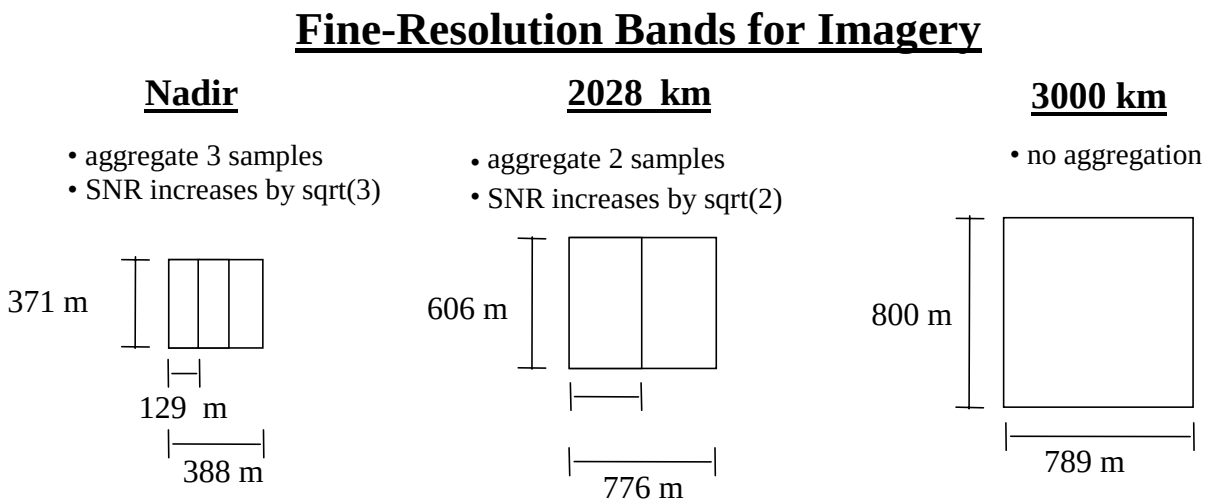

Figure 7. VIIRS detector footprint aggregation scheme for building Imagery "pixels".

Figure 8, showing the Horizontal Sampling Interval (HSI) that results from the combination scan/aggregation scheme, illustrates the benefits of the aggregation scheme for spatial resolution.

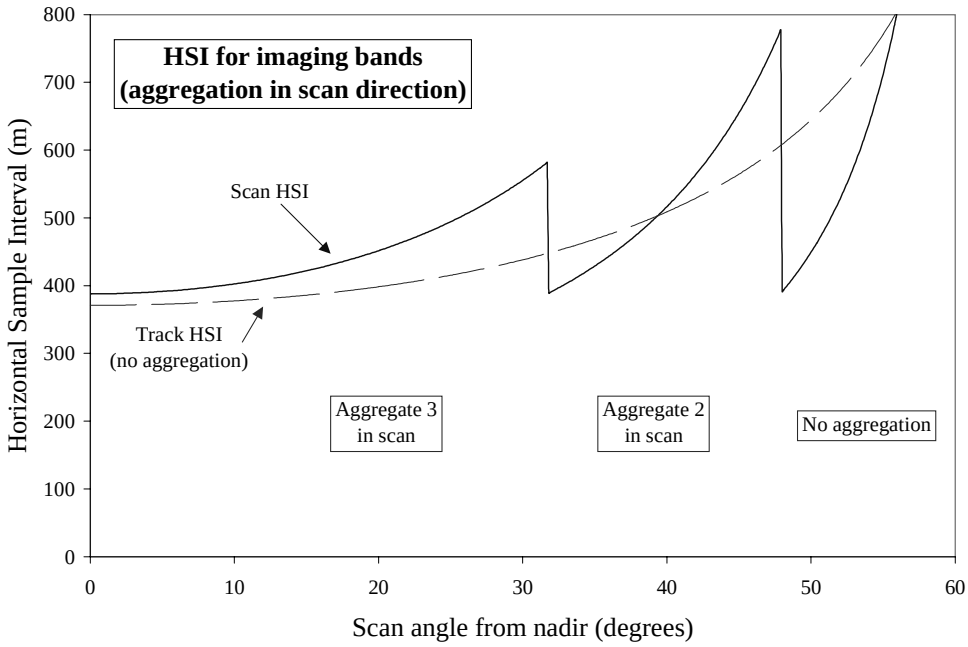

Figure 8. Horizontal Sampling Interval (HSI) for imagery bands (aggregation in scan direction).

The HRI of the Daytime Visible (DV), Long-Wave Infrared (LWIR) and Mid-Wave Infrared (MWIR) imagery will be the HSI. The Modulation Transfer Function (MTF) specification is 0.5 at the sampling Nyquist frequency, resulting in HSR equal to HSI. Therefore, the specification for HRI is equivalent to the imagery HSR specification.

Even though the aggregation scheme greatly reduces the growth in HSI across the scan, there is still a factor of 2 growth resulting in a residual "bow tie" effect. We achieve an additional reduction in the bow tie by deleting 4 of the 32 detectors from the output data steam for the middle (Aggregate 2) part of the scan and 8 of the 32 detectors for the edge (No aggregation) part of the scan. Figure 9 illustrates the resultant additional bow tie deletion.

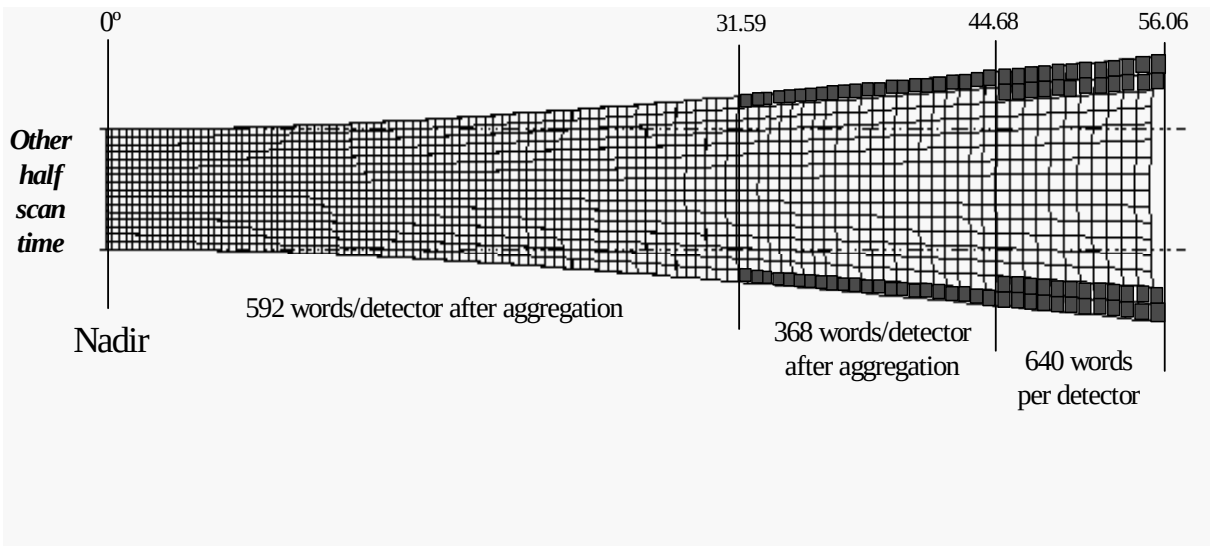

Figure 9. VIIRS aggregation and bow tie pixel reduction.

The sensitivity performance of the VIIRS imagery bands (c.f. Table 8 in Section 2.5) exceeds the Measurement Uncertainty specifications listed in Table 2 with margins > 30%.

3.2.5.1 Daytime/Nighttime Visible Band

The TOA radiances and TOA reflectances are produced over the entire operating range of the DNB.

The SNR performance of the DNB at nadir is shown in Figure 10. The performance at edge of scan is shown in Figure 11.

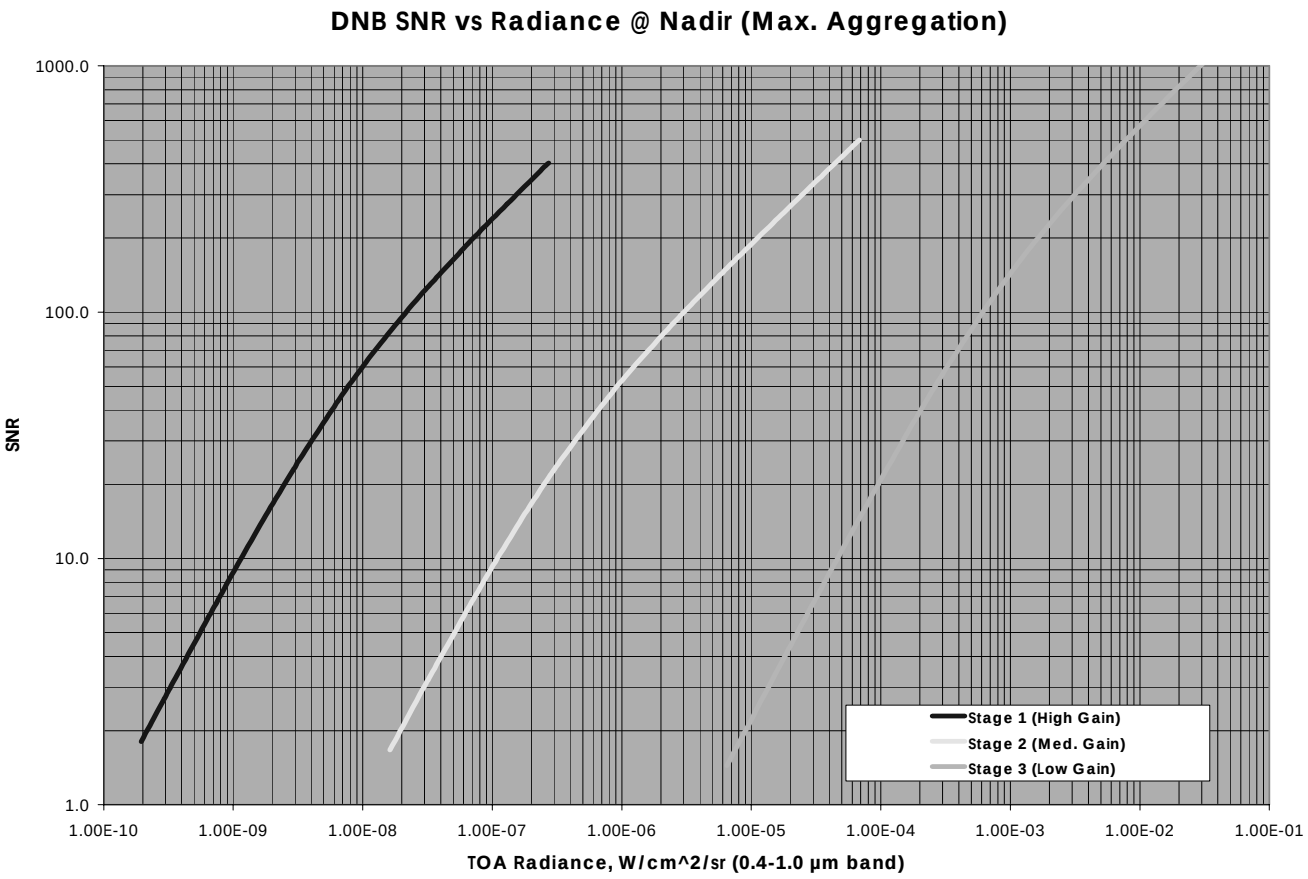

Figure 10. Signal-to-noise performance of the Daytime/Nighttime Visible Imagery Band at nadir, for each of the three CCD gain stages. SNR performance over the specified measurement range (4.E-9 – 3.E-2 W/cm^2/sr) is 30 to 1000. SNR greater than 3 is achieved at a radiance as low as 3.2E-10 W/cm^2/sr.

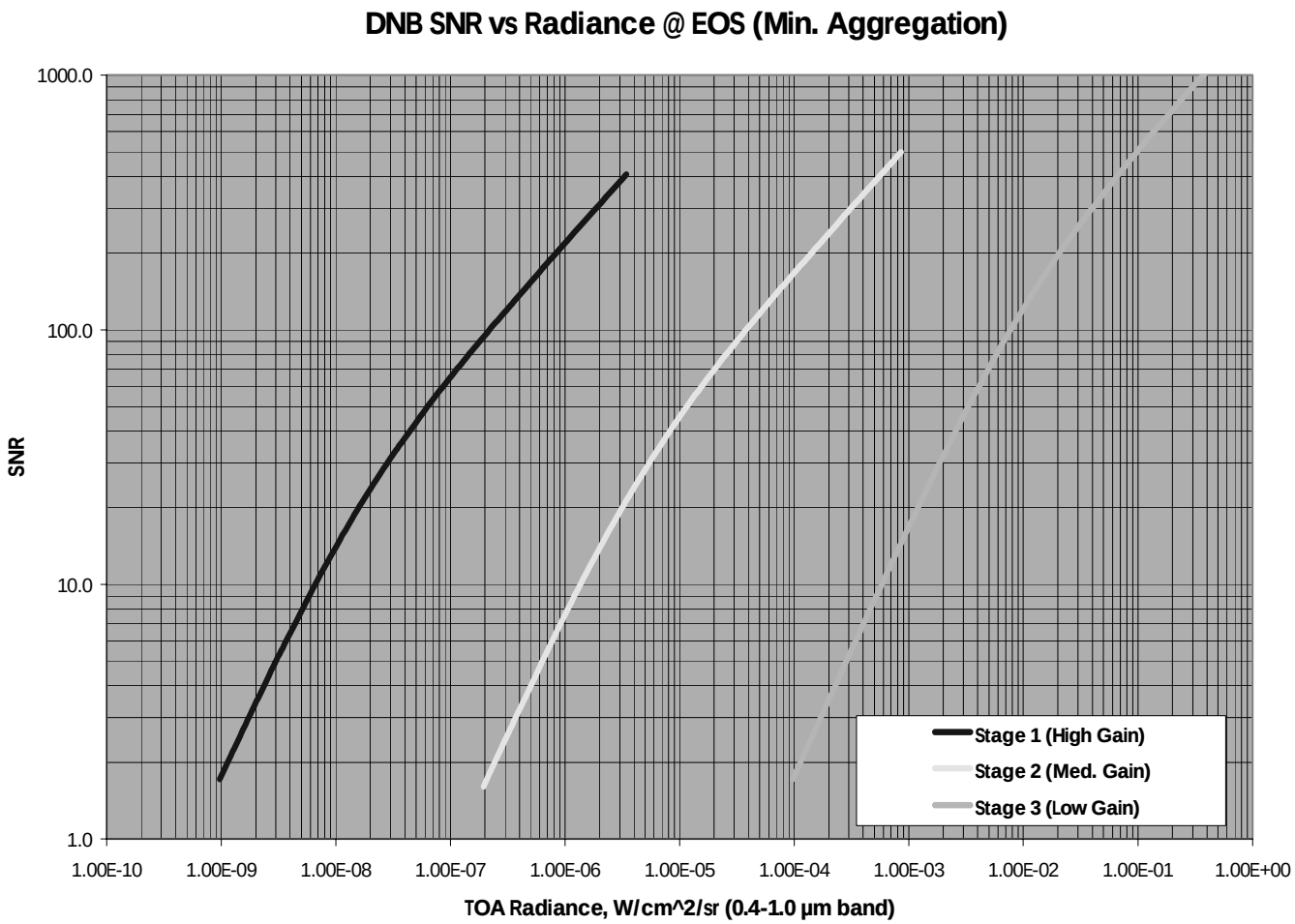

Figure 11. Signal-to-noise performance of the Daytime/Nighttime Visible Imagery Band at edge of scan, for each of the three CCD gain stages. SNR performance over the specified measurement range (4.E-9 – 3.E-2 W/cm^2/sr) is 7 to 250. SNR greater than 3 is achieved at a radiance as low as 1.8E-9 W/cm^2/sr.

The spectral response of the DNB has been designed to operate efficiently under lunar illumination conditions, as shown in Figure 12.

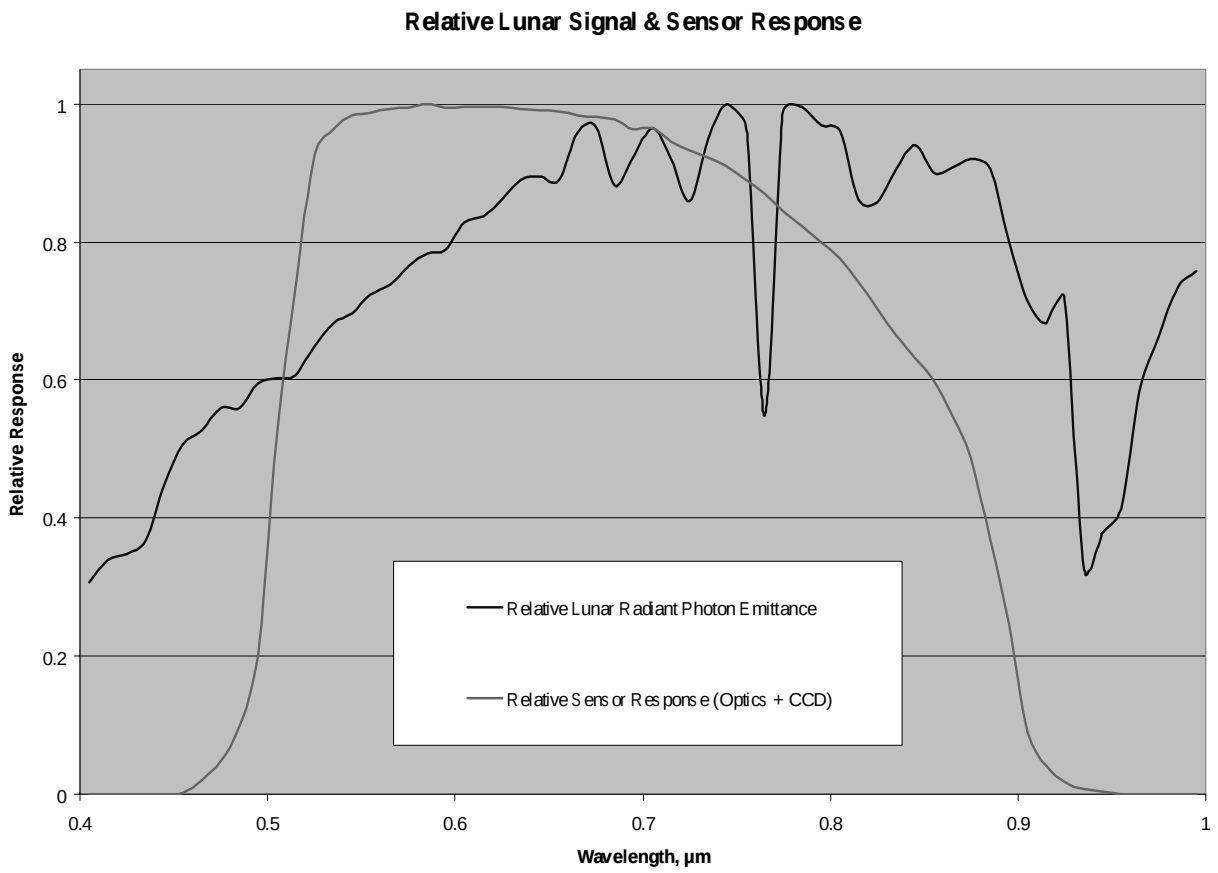

Figure 12. Spectral Response of the Daytime/Nighttime Visible Imagery band, compared with the lunar signal.

The spectral response of the DNB is designed to decline sharply at 0.5 microns, as can be seen in Figure 12. The purpose of the short-wave cut-off is to reduce contamination by atmospheric path radiance, which is more pronounced at shorter wave lengths. The design is compatible with OLS heritage.

SNR performance at night will vary with lunar phase, lunar elevation angle, and scan angle. An example for quarter moon phase is shown in Figure 13.

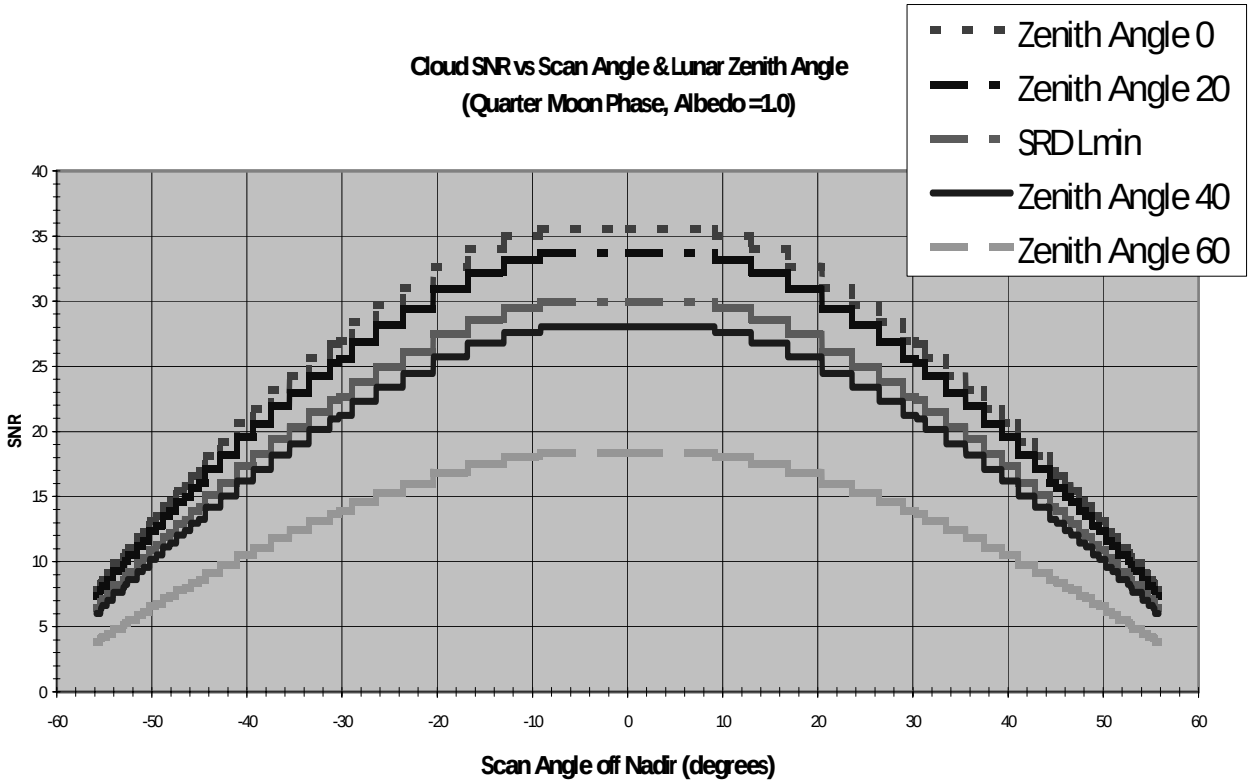

Figure 13. SNR Performance of the Daytime/Nighttime Visible Imagery under quarter-moon illumination conditions, as a function of scan angle.

The top two curves and bottom two curves represent lunar zenith angles of 0, 20, 40, and 60 degrees respectively. The middle curve corresponds to the minimum measurement range of 4E-9 W/cm2/sr. SNR greater than 10 is achieved at the minimum radiance for almost the entire scan. SNR as high as 30 is achieved at the minimum radiance for a nadir view.

3.2.5.2 Other Imagery Bands

Performance characteristics for the Daytime Visible (DV), Long-Wave Infrared (LWIR), and Mid-Wave Infrared (MWIR) imagery bands meet specifications with comfortable margin (c.f. Figure 9, Table 7, and Table 8).

3.3 NCC VISIBLE IMAGERY PRODUCTION

3.3.1 Processing Outline

This section describes the NCC Imagery EDR ground processing, which is executed only on data generated during periods of Terminator mode operation. The NCC algorithm takes calibrated and geolocated radiance as input. Thus, before the algorithm can be executed, a preprocessing step must be taken to convert the RDR to SDR *[Y3261]*.

3.3.1.1 Baseline Approach – Gain Management Algorithm

Our baseline approach is to adapt the OLS processing algorithm for terminator imagery. We have chosen this approach to ensure operational continuity between the DMSP and NPOESS missions.

The OLS terminator imagery is produced by a Gain Management Algorithm (GMA). The algorithm has been in use since the early 1980s. It is implemented by the OLS on-board analog signal processor (ASP). The function of the GMA is to adjust the on-board analog gain to compensate for the variable source signal radiance. The variable digital gain amplifier (VDGA) operates in the ASP. A detailed description of the process can be found in the OLS Technical Operating Report (Westinghouse, 1993). Summarizing from the report:

"During active scan, the along scan gain control (ASGC) software controls the gain value presented to the VDGA. The computations performed for this control depend upon the spacecraft elevation, azimuth, and altitude, and the OLS scan angle. This computation produces the scene source elevation angle used to obtain a gain value from the gain value versus scene source elevation (GVVSSE) table. Thus, the software will cause the VDGA gain to follow the GVVSSE curve as defined by the GVVSSE table values."

Figure 14, created from data in the OLS Technical Operating Report, illustrates a typical GVVSSE curve.

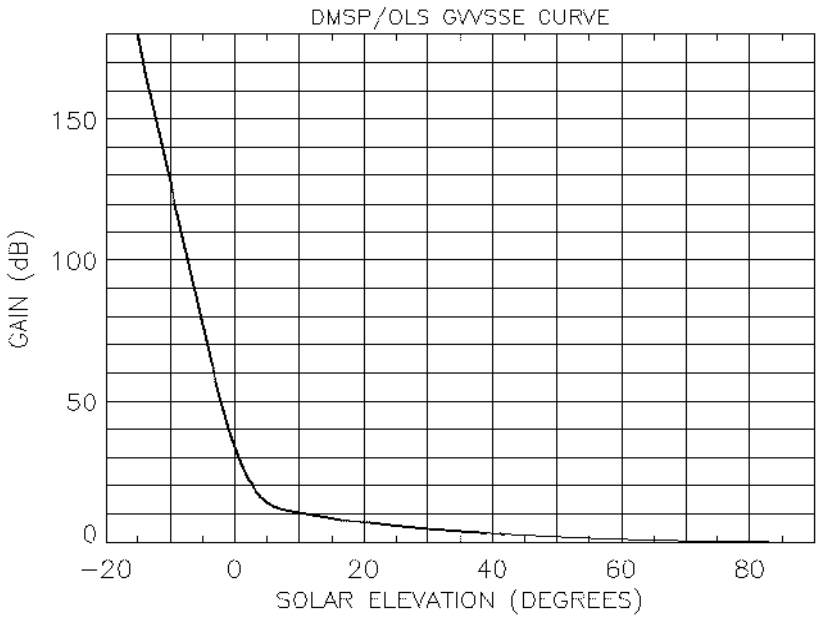

Figure 14 – Typical Gain Value Versus Scene Source Elevation (GVVSSE) Curve for OLS on board variable gain control. The curve is designed so that a source with an albedo = 0.8 produces a 5 volt output signal from the L channel analog signal processor (Reference: OLS Technical Operating Report, March 1993).

BRDF corrections are applied as adjustments of the elevation angle in the GVVSSE table. There is a comparable table (GVVSLE) for a lunar source signal. Lunar BRDF and lunar phase corrections are applied as adjustments of the elevation angle in the GVVSLE table. The function of the GMA is to adjust the ASP gain so that a signal from a reflecting surface (cloud or ground) with an albedo of 0.8 and the modeled BRDF will produce a 5 volt output signal from the L channel ASP. The GMA was designed to accommodate the capabilities of late 1970s processors. The implementation of the VIIRS NCC algorithm will occur on the ground, within the NPOESS IDPS, though the OLS implementation is on board. This approach will provide the flexibility to make algorithm and LUT modifications easily via ground software changes, and will take advantage of the superior computational capability of the IDPS. Our approach will preserve the OLS heritage by using LUTs that capture the gain and BRDF corrections applied on board the OLS.

The algorithm operates as follows:

1) Read the 5 pre-constructed LUTs into memory. These are the GVVSSE LUT, the Solar BRDF LUT, the GVVSLE LUT, the Lunar BRDF LUT, and the Aerosol Correction LUT. Detailed descriptions of the LUTs can be found in *[Y3273]*.

2) Obtain DNB TOA radiances from the VIIRS EV_DNB SDR. The TOA radiances are stored as a 2-d array corresponding to each DNB pixel.

3) Obtain latitude/longitude, solar, lunar, and viewing angles, and lunar phase from the SDR.

4) For pixels where the solar source radiance is sufficient (determined by solar zenith angle), compute solar source radiance, using information in the GVVSSE and Solar BRDF LUTs.

5) For pixels where the lunar source radiance is sufficient (determined by lunar zenith angle), compute lunar source radiance, using information in the GVVSLE and Lunar BRDF LUTs.

6) If selected by a pre-set switch contained in the Aerosol Correction LUT, compute the expected path radiance at each pixel, using the Aerosol Optical Thickness IP and the Aerosol Correction LUT as input data. This step will require improved radiative transfer modeling, and is deferred to future development.

7) Convert the observed TOA radiance at each pixel to albedo, using the solar source radiance, the lunar source radiance, and optionally the path radiance.

8) Write the albedo to the Imagery EDR file, along with quality flags.

The process flow for the algorithm is illustrated in Figure 15. The process flow operates on each DNB pixel.

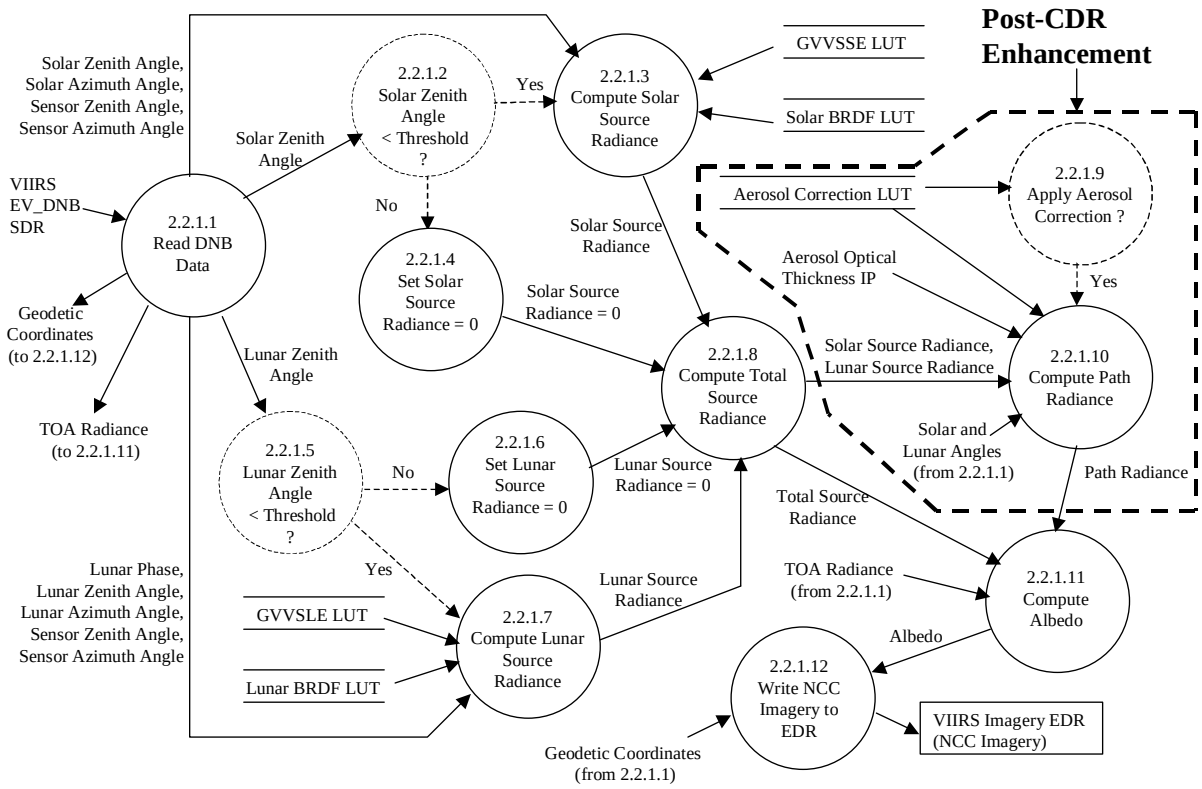

Figure 15. Process flow for the NCC Imagery algorithm.

3.3.1.2 Enhanced Algorithm Approach - Atmospheric Correction

As there are no explicit performance metrics for the NCC Imagery EDR, there is no requirement to provide NCC imagery that exceeds the performance of the OLS approach. However, there is value to the operational community in providing an NCC product superior to the terminator imagery currently provided by OLS. During Phase I, we developed an alternative NCC algorithm that promises to provide a superior NCC product. During Phase II, we have integrated the alternative algorithm with the OLS-based approach by adding step 6 to the common process flow. Implementation of steps 1-5 and 7 constitutes the OLS-based approach. Implementation of step 6 constitutes a post-CDR pre-planned product improvement (P^3I). Implementation of all 7 steps constitutes the alternative approach of Phase I, as documented in the version 3 ATBD. The version 5 algorithm for NCC Imagery therefore preserves the OLS operational heritage and

provides a framework for future implementation of an atmospheric correction enhancement, when this is made feasible by improvements in radiative transfer models. When solar zenith angle is greater than 89.0 degrees, MODTRAN simulation (including version 4.0 and all previous versions) does not produce accurate TOA radiance. That is, the radiances calculated from MODTRAN are all the same for any surface conditions (i.e., from black surface with zero albedo to complete reflective surface with 1.0 albedo) and clouds. Thus, there is no cloud or surface signal in the simulated TOA radiance. A better RT model for the solar zenith angle range between 90 to 105 degrees is required for full implementation of the atmospheric correction enhancement to the algorithm. Although the OLS gain tables include zenith angles as large as 105 degrees, the solar signal will be smaller than the minimum of the DNB measurement range for solar zenith angle greater than 100 degrees. In practice, therefore, it is sufficient for the RT model to be accurate out to angles of 100 degrees.

3.3.2 Algorithm Input

3.3.2.1 VIIRS data

The algorithm requires the calibrated and geolocated day/night band radiance and the corresponding view/illumination geometry data. These are all supplied by the VIIRS EV_DNB SDR. The optional atmospheric correction step also requires aerosol optical thickness, supplied by the VIIRS Aerosol Optical Thickness IP.

3.3.2.2 Non VIIRS data

The algorithm requires five pre-constructed LUTs, described in *[Y3273]*. The GVVSSE LUT will contain a solar gain function for a range of solar zenith angles (c.f. Figure 14). The GVVSLE LUT will contain a lunar gain function for a range of lunar zenith angles, similar to the GVVSSE function. The Solar BRDF LUT and Lunar BRDF LUT will contain BRDF correction factors, binned by zenith angle, viewing angle, and relative azimuth angle. The Aerosol Correction LUT will contain an atmospheric correction on/off switch and model path radiances, binned by AOT, source zenith angle, viewing angle, and relative azimuth angle. The Aerosol Correction LUT will be filled in the future, when feasible. The LUTs will be generated by the VIIRS Look up Table Generation Tool (LUTGT) *[Y10810]*.

3.3.3 Theoretical Description

3.3.3.1 Physics of the Problem

For decades, merged images (or “photo-mosaics”) were produced manually by “cut and paste” methods and by photo-manipulation. More recently, automated methods have been developed that compute the merged image. These methods typically create a new image on a line by line basis. Each line may take data from one image up to a given point; beyond that point, data comes from the second image. The region adjacent to the switchover point is called the “seam”.

An unintended feature of photo-mosaicing is the presence of visual artifacts that result from inherent differences between the two images that compose the merged image. The visual artifacts not only introduce potential confusion for the human analyst but can mask features of interest in the original images such as cloud type indicators or ice edge features. If one simply lines up two photos of the same scene taken at different times of day from the same vantage point and then cuts through the pair and tapes the opposite segments from the separate images together, one will immediately notice several artifacts. For example, if the contrast in one image does not match the contrast in the second or one is uniformly darker than the other (histogram mismatch), the analyst will notice an apparent edge at the seam joining the two halves. This seam is difficult to ignore since the eye responds preferentially to long straight features (e.g., edges, day/night texture changes, etc.).

Generically, artifacts can result from a number of inter-images differences. Some of these are content-related e.g., due to images taken at different times; some are sensor related, e.g., differences in dynamic range; some are platform-related, e.g., misregistration errors; and some result from a combination of content and platform e.g., uncorrected parallax errors. The algorithm must accomplish the seam-finding and image combination in such a way so as to minimize the introduction of artifacts and subsequently must minimize their visual impact.

A further occasion for artifacts occurs due to the special processing required for pixels lying within the solar terminator. For the purposes of this ATBD, we identify the terminator region as the zone that is neither astronomical night nor standard daytime. These pixels may be saturated in the high gain CCD stage while not being fully illuminated in the low gain stage. The choice of grayscale value for the image therefore must maintain available contrast without introducing confusing artifacts or false contrasts.

The NCC EDR does not correspond to a single consistent physical characteristic of the natural environment. The resultant data product is used to provide the analyst an image for visual interpretation. The product is derived from the DNB, which has a separate algorithmic production process that must conform to the system requirements. The requirements that pertain to the NCC EDR instead relate to its usability for manual interpretation.

The NCC EDR must adequately represent the surface and atmospheric (specifically, cloud) conditions across the terminator region to be analyzed without artifacts due to the significant radiance difference (on the order of 1.e06 to 1.e07).

Image quality in the terminator region is also degraded by atmospheric scattering. Because of the low sun angle, the radiation transmitted downward to a reflecting surface (cloud or ground) travels longer path lengths, thereby increasing the amount of path radiance relative to reflected radiance. This is undesirable, since the primary purpose of image analysis is to detect the reflecting sources. Excessive path radiance washes out the image. An example of this effect can be seen in Figure 16. In principle, atmospheric correction can remove the path radiance, thereby recovering the contrast between various reflecting surfaces. In practice, current RT models (e.g. MODTRAN 4.0) are not capable of achieving satisfactory path radiance removal in the terminator region (c.f. Section 3.3.1.2).

3.3.3.2 Mathematical Description of the Algorithm

The alternative algorithm of Phase I includes all of the planned processing steps, and therefore provides the most complete mathematical description.

The general procedures of the alternative algorithm can be expressed using the following:

a) In the terminator region, the radiance of the day/night band (retrieved from the digital number using the calibration coefficients) is resultant from both solar and lunar illumination. Other sources of radiance (e.g. city lights) are not considered here. The combined radiance can then be expressed as the following:

$$L = L_{sun} + L_{moon} \qquad (3.3.3.2.1)$$

b) The radiance components can be decomposed to those from atmospheric path and those from the target (surface or clouds):

$$L = L_{sun_p} + L_{moon_p} + L_{sun_t} + L_{moon_t} \qquad (3.3.3.2.2)$$

c) The path radiance reduction procedure is to remove the path radiance from the total radiance, i.e., subtract the total radiance by the path radiance simulated from model atmosphere. The resultant radiance becomes:

$$L' = L_{sun_t} + L_{moon_t} \qquad (3.3.3.2.3)$$

d) The normalization procedure is to divide this new radiance by the reference radiance of a reference surface, which is derived from model atmospheres with the sun and the moon as illumination sources and path radiance removed:

$$L_{norm}=L'/Lref=(L_{sun_t} + L_{moon_t})/(Lref_{sun_t} + Lref_{moon_t}) \qquad (3.3.3.2.4)$$

If there is no other illumination source than the sun and the moon, and if the model atmosphere matches the real atmosphere, the L_{norm} value is the same as the ratio of the target albedo to the reference surface albedo. In actuality, the radiance resultant from sources other than the sun and the moon is very small in most circumstances and is negligible as compared to those from solar/lunar irradiance. In addition, the real atmosphere will not match exactly to the model atmosphere used in the pre-constructed LUT. Therefore, the L_{norm} value is approximately but not exactly proportional to the ratio of the target albedo to the reference surface albedo. The significant radiance difference across the terminator due to illumination irradiance difference is normalized in L_{norm} and the resultant image product will present near constant contrast across the scene.

3.3.4 Archived Algorithm Output

The NCC algorithm output is a visible image at the resolution of the DNB Horizontal Reporting Interval of 742 meters +/- 5%. It will be stored in the Imagery EDR as a field in the Imagery HDF file, along with associated quality flags.

3.3.5 Performance of NCC Visible Imagery

3.3.5.1 Baseline Algorithm

Our baseline algorithm is designed to capture the on board OLS GMA within the data processing architecture of the VIIRS Ground Segment. We therefore expect baseline performance to be comparable to that of the OLS process. Figure 16 is an example of typical OLS terminator imagery.

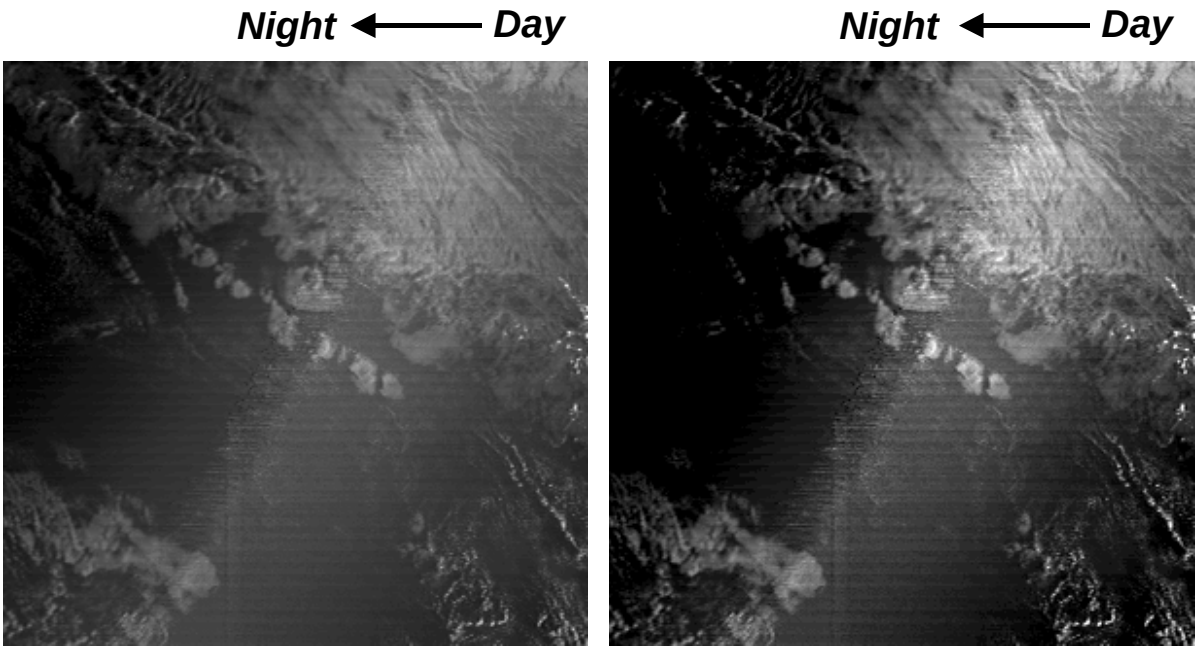

Figure 16 – F13 OLS Visible (HRD) image for the first terminator crossing of the July 20, 2001 1131 UT orbit.

The image in Figure 16 displays 300 SDS scan lines for a scan angle range of $24^0 – 47^0$. The daytime/nighttime sides are indicated. The full dynamic range is displayed in the LEFT image. The RIGHT image is contrast-enhanced to highlight the terminator crossing effects (e.g., path radiance from atmospheric scattering). Figure 16 demonstrates how well the OLS algorithm works. Because the image processing occurs on board, we have no pre-processed image with which to compare it. The image shown in Figure 17 is a good indicator of how Figure 16 would appear if the OLS analog signal was not processed by the OLS GMA.

3.3.5.2 Atmospheric Correction Enhancement

The atmospheric correction algorithm is designed to improve the NCC imagery by removing the path radiance caused by atmospheric scattering. The analysis of algorithm performance performed during Phase I was based on MODTRAN 4.0 simulation. When the SZA is greater than 89.0 degrees, MODTRAN simulation (including version 4.0 and all previous versions) does not produce accurate TOA radiance. That is, the radiance calculated from MODTRAN is the same for any surface or cloud albedo. Thus, there is no cloud and surface signal in the simulated TOA radiance except for the path radiance which only changes with illumination and viewing geometry at given atmosphere.

For a noise-free simulation, the path radiance is 100% removed using the LUT because the simulated image and the LUT were generated using the same MODTRAN model. Therefore, when the SZA is greater than 89 degrees, the solar (path) radiance is completely removed and the retrieved image preserves the cloud and surface contrast. In a real situation, because the solar path radiance cannot be completely removed, the algorithm's performance in the region where SZA ranges from 89 to 100 degrees will of course not be as good as a simulated noise-free result.

An improved radiation transfer (RT) model for the SZA range between 90 and 100 degrees is required to test algorithm performance on real sensor data. We discuss this matter further in the section on algorithm initialization and validation (Section 3.3.6.3).

Figure 17 is a simulated radiance image at the terminator area using the Amazon TERCAT scene provided by the IPO. Due to the significant irradiance change across the terminator, features in the nighttime side of the scene are not visible. Figure 18 shows the output from a prototype of the NCC alternative algorithm given the inputs from Figure 17, for an ideal noise-free sensor input and ideal atmosphere / BRDF correction. It is included as an example of the quality of NCC imagery that we aspire to achieve with our algorithm.

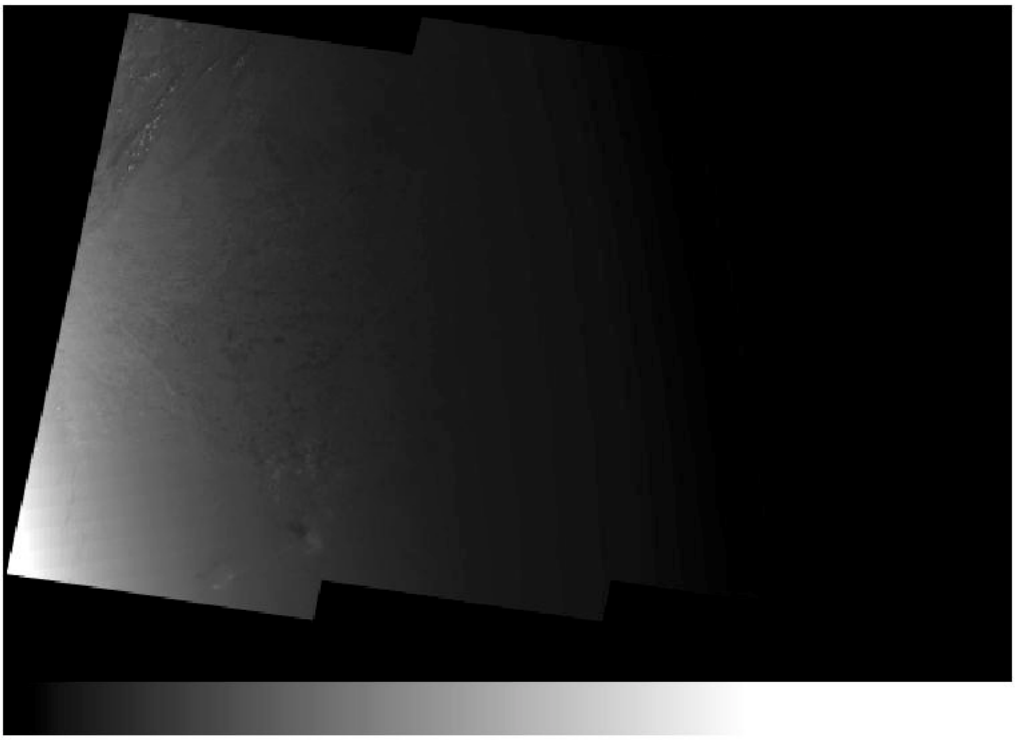

Figure 17. Input radiance image to the NCC algorithm

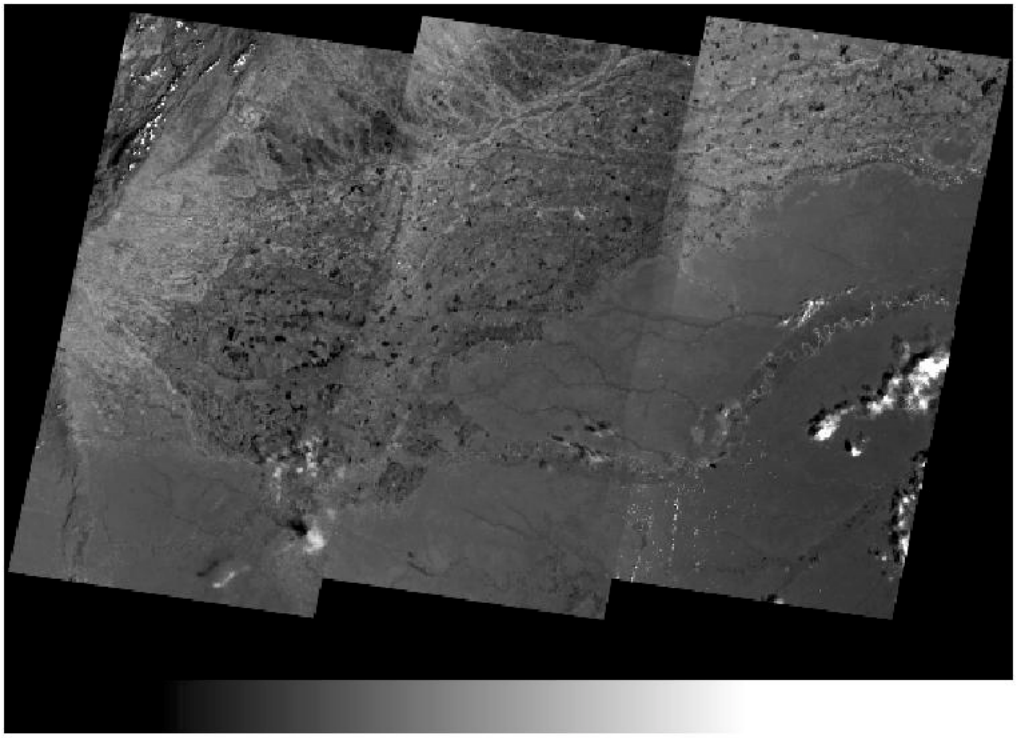

Figure 18. NCC Algorithm Output

3.3.6 Initialization and Validation

3.3.6.1 Initialization

The baseline algorithm is based on proven OLS heritage. The LUTs used by the algorithm will be generated offline by the LUTGT, using OLS gain and BRDF values to preserve continuity. The atmospheric correction LUT will also be generated by the LUTGT, using the best available forward model.

3.3.6.2 Pre-Launch Characterization

Our pre-launch plan is to test both the baseline algorithm and the enhancement algorithm on OLS imagery obtained from the National Geophysical Data Center (NGDC), and make any algorithm adjustments that improve the terminator imagery. Algorithm run time performance will be assessed with regard to the requirement to produce NCC Visible imagery in near real time at field terminals. The algorithm uses standard, straightforward interpolation of relatively simple LUTs. Therefore, we do not anticipate run time problems (c.f. Section 3.3.7.1).

3.3.6.3 Validation

Following NPP launch, NCC algorithm performance will be tested on VIIRS DNB terminator imagery. Validation will be by manual inspection of the NCC processed terminator imagery. Trained analysts can readily determine whether the imagery provides a near constant contrast across the terminator. The baseline algorithm, adapted from the heritage OLS technique, will be used operationally unless and until it is determined that the atmospheric correction enhancement produces a superior product. If atmospheric correction LUTs are developed prior to NPP launch, we can re-process the identical granule off-line with the atmospheric correction applied. Trained analysts can compare both sets of NCC imagery to determine whether atmospheric correction produces a superior product.

3.3.7 Practical Considerations

3.3.7.1 Numerical Computation Considerations

The baseline algorithm is already operational on the DMSP, and poses no numerical computation problems. The solar and lunar gain values are obtained from direct interpolation of 1-d LUT arrays, with no inversion, iteration, or search window functions. The BRDF values are also obtained from direct interpolation of LUT arrays. Though these are multi-dimensional, their size will be kept small enough to allow rapid processing.

The atmospheric correction algorithm should run as quickly, since it involves a similar process of acquiring values from a pre-set LUT for each pixel. The size of the path radiance LUT depends on the numbers of geometry nodes and atmospheric models. The actual computation for each output pixel is relatively simple and the total computation time is largely dependent on the size of the input LUT. As with the BRDF LUTs, the size of the path radiance array will be kept small enough to allow rapid processing.

3.3.7.2 Programming and Procedural Considerations

All procedures are automatic, to perform in the operational environment. All LUTs will be generated off-line.

3.3.7.3 Configuration of Retrievals

The NCC algorithm requires the VIIRS day/night band SDR, the VIIRS Aerosol Optical Thickness IP, and five VIIRS LUTs as input. The output of this algorithm is for analyst manual interpretation and does not serve as quantitative input to any other EDRs. The NPOESS processing configuration is designed to satisfy these expectations.

3.3.7.4 Quality Assessment and Diagnostics

In general, the NCC image should resemble its constituent imagery products. If these products are insufficient to support manual analysis, then the NCC product is unlikely to serve the analyst any better. Thus, if there is little moonlight, contrast at the terminator and on the dark side will be poor. Sun glint will also impair manual analysis. If helpful to analysts, it is possible to flag imagery that might show sun or moon glint. The algorithm software is designed to set NCC quality flags for each DNB pixel. The flags are set if there is a processing problem with the solar gain, solar BRDF, lunar gain, lunar BRDF, and/or path radiance derivations. If either the observed DNB TOA radiance or the computed source radiance for a given pixel is less than a minimum threshold (currently set as the measurement range minimum of 4. e-9 W/cm^2/sr), a low radiance quality flag will be set for that pixel.

3.3.8 Algorithm Watch List

Following its review of the Version 3 ATBDs, the VIIRS Operational Algorithm Team (VOAT) has produced a list of items requiring attention. One of these, item 13: NCC Algorithm Products, directly affects the NCC Imagery EDR.

During discussions with the VOAT, it was clear that the reason for this item was the concern over the alternative algorithm. Following our clarification that the baseline algorithm would be adapted from the current OLS algorithm, this item was cancelled. Our NCC algorithm development plan, as described in Sections 3.3.1 and 3.3.6, is now low risk. We will continue to work with the IPO and the VOAT to ensure a low risk implementation of the NCC algorithm.

3.4 MANUAL CLOUD ANALYSIS PRODUCT DESCRIPTION

3.4.1 Processing Outline

Manual cloud analysis products are not produced by the VIIRS operational system. They are expected to be produced at various locations by trained analysts, using the VIIRS Imagery as input data. Different analysts may wish to use different techniques. Our specifications for the VIIRS sensor have been developed by analysis using the techniques described below, which we refer to as the VIIRS Manually-Generated Cloud Data algorithm (VMCD). The first version of a

User's Guide to assist an analyst in implementing the techniques is included as an Appendix to this document.

3.4.2 Algorithm Input

Ancillary data, both VIIRS and non-VIIRS, are useful for manual cloud analysis. We have assessed the relative importance of the various sources of ancillary data. A prioritized list is presented as Table 9.

Table 9. Ancillary data to augment manual cloud analysis.

Prioritized Item	Application	Utility assessment
1) Cloud mask/ Cloud Cover	Used to speed manual analysis by providing a mostly-correct first guess	Crucial. Manual analysis cannot be accomplished without this. Analysis timelines do not permit analyst to determine the cloud state of every pixel or even horizontal cell individually.
2) Geographic/ physio- graphic data, oceanic currents	Identifies clear-scene structural and textural details for comparison	Very important, but difficult to assess contribution. Analysts have varying degrees of initial geographic knowledge
3) Raw Vis/Day-Night Vis/IR imagery (contrast enhanced)	Presents a less processed view of the scene. Processing artifacts, pseudo-colors, etc., are removed, allowing analysts to make an independent assessment of the scene.	Important but difficult to assess contribution. Perform manual cloud analysis with and without these data using different teams of analysts; compare results to ground truth [Manual comparison method]
4) Cloud Mask diagnostics (TBR)	Flags that indicate whether ambiguous results occurred from the several cloud tests. Manual attention concentrates on these locations	Will be important but difficult to assess contribution. Perform manual cloud analysis w/ and w/o, compare results to ground truth
5) Snow/Ice fields	Draws analyst attention to suspect snow/ice areas for confirmation.	Important. Manual comparison method
6) Conventional Surface observer cloud reports from nearest hourly/synoptic time	Provides independent on-the-spot assessment of cloud conditions	Less important. Manual comparison method
7) Aerosols	Analyst can judge whether imagery effects are from clouds or aerosols	Less important. Manual comparison method
8) Cloud Top T, p, z	Could be of use but is likely to overload an already stressed analyst. Would be better to design one product that would roll this and the next three items together and ideally merge with cloud mask.	Given a reliable product this could take on greater importance.
9) Optical depth, Effective Particle Size	See Cloud Top T, p, z	See Cloud Top T, p, z
10) CMIS* soundings	See Cloud Top T, p, z	See Cloud Top T, p, z

* Conical Scanning Microwave Imager/Sounder

It is important to not overwhelm an analyst with an abundance of information. Manual cloud analysis accuracy is not the bottleneck. Decreasing the amount of time required to review and correct the automated analysis to a given level of accuracy is more important than further increasing accuracy, once the objective performance level is met. Additional information can greatly decrease manual analysis throughput. Cloud analysts are generally mass producers, not craftsmen or artisans.

Given that, we could focus our thoughts on a "new" product that would synthesize many of the items presented in the table into one product that could be easily used by an analyst to improve his analysis.

3.4.2.1 VIIRS Data

The VMCD algorithm requires SDRs for each VIIRS imagery channel and several imagery assist channels. The Imagery channels include the daytime/nighttime visible band, the 0.64 µm daytime visible band, the 3.74 µm band, and the 11.45 µm band. The imagery assist channels include the 0.412 µm, 0.858 µm, 1.38 µm, 1.61 µm, 4.05 µm, 8.55 µm, and the 10.8 µm bands. It is assumed that these data are accurately calibrated, earth-located, and co-registered.

3.4.2.2 Non-VIIRS Data

AFWA has two major functions that use VIIRS capabilities to generate cloud data (1) QC, Bogus of the cloud data base, discussed in Section 2.3.1, and (2) contingency support, e.g. understanding the contents of a scene – e.g. Kosovo. Ancillary data requirements for both functions include:

a. Automated cloud analyses (cloud cover, cloud top height, etc.)

b. Surface type maps (geography) of area covered by imagery

c. Surface elevation and terrain maps

d. Conventional weather observations as available (surface reports, aircraft reports, and radiosonde observations)

3.4.3 Theoretical Description

3.4.3.1 Physics of the Problem

The ability to manually identify clouds in any given spectral band is based upon the contrast, measured in radiance, between the cloud and the surrounding cloud-free background. More precisely:

$$C = I_v(0)_{cloud} \ / \ I_v(0)_{background} \qquad (3.4.3.1.1)$$

The measured or satellite observed radiance, $I_\nu(0)$, may be composed of reflected solar radiation and resultant albedos, thermal radiation emitted by or brightness temperatures of the terrestrial feature, or both when observations are made in the 3-5 micron wavelength interval.

The monochromatic, upwelling infrared radiance measured at the sensor aperture in a cloud-free atmospohere is given by (Liou, 1980, p. 247):

$$I_\nu(0) = \varepsilon_\nu B_\nu[T_s] T_\nu(p_s) + \int_{p_s}^{0} B_\nu[T(p)] \frac{\partial T_\nu(p)}{\partial p} dp + (1-\varepsilon_\nu) \int_{0}^{p_s} B_\nu[T(p)] \frac{\partial T_\nu(p)}{\partial p} dp \qquad (3.4.3.1.2)$$

where: ν = wavenumber of emission

$B_\nu[T(p)]$ = Planck function at wavenumber (ν) for temperature (T)

ε_ν = emissivity of surface at wavenumber (ν)

$T_\nu(p_s)$ = atmospheric transmittance between pressure level (p_S) and space

$I_\nu(0)$ = monochromatic radiance arriving at satellite.

P_s = surface pressure

T_s = surface temperature

For imaging sensors, the atmospheric transmittance between pressure levels and space is very small and Equation 3.4.3.1.2 is closely approximated by Equation 3.4.3.1.3, which shows that the radiance arriving at the satellite sensor is a function of the emissivity of the surface, the surface temperature, and the transmission from the surface to the sensor:

$$I_\nu(0) = \varepsilon_\nu B_\nu[T_s] T_\nu(p_s) \qquad (3.4.3.1.3)$$

Thus, the capability to manually detect a cloud in infrared imagery is enhanced not only by temperature contrasts between the features but also by observing the features in spectral bands where there emissivity contrasts exist or in bandpasses which effect atmospheric transmissivity as is the case with the 1.378 micron channel which suppresses the signatures of low-level features, including clouds and cloud-free surface thus enhancing the signatures of higher level clouds.

The amount of solar radiation reflected by the Earth-atmosphere system into the sensor aperture is given by (Liou, 1980, p. 25):

$$I(0;\mu,) = I(\tau_{1;\mu,}\phi)^{-\tau_1/\mu} + \int_0^{\tau_1} J(\tau';\mu,\phi) e^{-\tau_1/\mu} \frac{d\tau'}{\mu}, \qquad (3.4.3.1.4)$$

Term A Term B

where:

$I_\nu(0)$ = monochromatic radiance arriving at satellite

τ = optical depth of each τ' layer, while the atmosphere is τ_1 thick

Term A	= surface energy contribution attenuated to space
Term B	= internal atmospheric contributions attenuated to space
μ	= cosine of angle between radiation stream and local zenith angle
ϕ	= azimuth angle.

The complexity of this calculation lies in the source function term, $J(\tau;\mu,\phi)$, which is given for solar radiation by Equation 3.4.3.1.5.

$$J(\tau;\mu,\phi) = \frac{\tilde{\omega}}{4\pi}\int_0^{2\pi}\int_{-1}^{1} I(\tau;\mu',\phi')P(\mu,\phi;\mu',\phi')d\mu' d\phi' \qquad (3.4.3.1.5)$$

Term C

$$+\frac{\tilde{\omega}}{4\pi}\pi F_0 P(\mu,\phi;-\mu_0,\phi_0)e^{-\tau/\mu_0}$$

Term D

where:

Term C	= multiple scattering of diffuse (scattered) energy
Term D	= single scattering of direct solar irradiance, F_O.

And:

ω	= single scattering albedo
P	= phase function
F_0	= solar irradiance
μ_0	= cosine of solar zenith angle
ϕ_0	= solar azimuth angle

Thus, the capability to manually detect a cloud in visible and near-infrared imagery is enhanced by viewing in spectral bands where contrasts in the reflectivities of the features are known to exist. In reality, monochromatic radiation does not exist because of line broadening from natural, pressure (collision), and Doppler (thermal velocity) effects. Also, since an instrument can distinguish only a finite bandwidth, the upwelling radiance measured by the satellite is integrated over the sensor transmission filter, which is also called the sensor response function, and is given by Equation 3.4.3.1.6.

$$I_\nu(0) = [\int_{\nu 1}^{\nu 2} I_\nu(0)\phi_\nu d\nu] / \int \phi_\nu d\nu \qquad (3.4.3.1.6)$$

where: ϕ_ν = filter (sensor) response function at wavenumber (ν)

ν_1,ν_2 = wavenumber range of filter response

3.4.3.2 Image Processing to Enhance Cloud Detection in Multispectral Imagery

The manual interpretation of clouds and background features in multispectral imagery is facilitated by the use of false color composite images which are made by assigning a different spectral band to each gun of a cathode ray tube (CRT; d'Entremont *et al.*, 1987). The hue of the false color composite emphasizes the gun in which the feature has the strongest signature, i.e., has the larger radiance arriving at the satellite sensor. Equal contributions from each channel in the CRT results in a feature appearing as a (white through black) gray shade in the false color composite, with the shade of gray depending upon the strength of albedos or brightness temperatures of the feature in the spectral bands.

In current operational AVHRR imagery, the signature of vegetated land is more pronounced in the 0.9-µm channel than the 0.6-µm band while water clouds are similar in both the 0.6-µm and 0.9-µm channels as seen in Panels A(1) and A(2) in Figure 19, respectively. Thus, a false color composite of the scene shown in Panel A(3) shows highly vegetated areas in green, less-vegetated areas as brown, and clouds as white (Hutchison *et al.*, 1997). In addition, the land-sea boundary is seen distinctly in the color composite since the land near the ocean's edge is densely vegetated while the ocean has a low albedo in both spectral bands.

Additional false color composites can be created to emphasize other features in the scene. For example, high water clouds may be differentiated from lower-level water clouds by including 3.7-µm and/or the 12.0-µm infrared bands shown in Panels A(1) and A(2), respectively in Figure 20. This process is demonstrated in Panel A(3) where the 0.6-µm image assigned to the blue gun in Figure 19 has been replaced with the 12.0-µm channel. Colder clouds appear bluish in the composite in Panel A(3) of Figure 20 while warmer clouds have a yellow-greenish hue.

Care must be taken using this false color composite to avoid misclassifying optical thin, cirrus clouds as lower-level clouds. This is accomplished using another color composite described in Figure 21.

First, a method is described to differentiate between snow and water clouds in daytime imagery. The contrast between snow and water clouds is greatly enhanced by including the 1.6-µm channel in the false color composite, since water clouds are highly reflective in this band while snow and ice (clouds) reflect poorly (Valovcin, 1978). Alternatively, the reflectively of snow in the 3.7-µm band is also very small and can be used to simulate the signatures in a 1.6-µm channel by removing the thermal component of the radiation from the observed satellite radiances (Hutchison *et al.*, 1997; Allen, Durkee, and Walsh, 1990) to create an image which facilitates the manual distinction between snow and water clouds as shown in Figure 21.

A benefit of using the 3.7-µm albedo channel, rather than the 1.6-µm imagery, to manually discriminate between snow and water clouds is that the former simultaneously enhances the contrast between snow and thin cirrus clouds as well as the contrast between water clouds and snow. In fact, the spectral signature of optically thin cirrus in the derived 3.7-µm albedo image is actually enhanced over that present in the 12.0-µm imagery (Hutchison *et al.*, 1997) as seen in Panels A(1) and A(2) of Figure 22. This stronger signature of cirrus in the 3.7-µm albedo image

over the 12.0-μm imagery results from the methodology used to create the former, which in effect produces a 3.7 minus 12.0-μm brightness temperature difference image that enhances the signature of thin cirrus.

A(1) 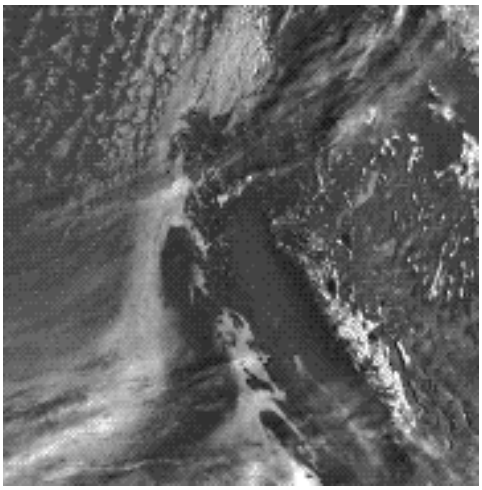 A(2) 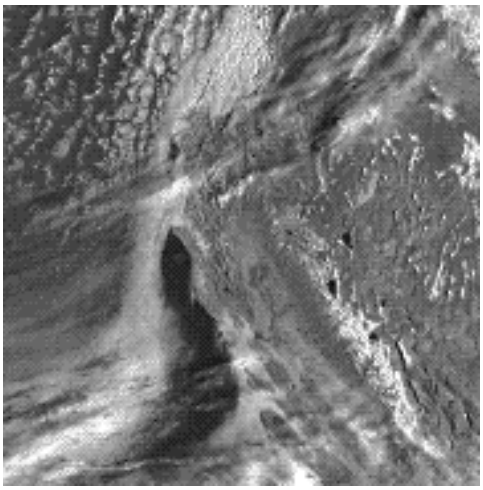

Panels A. Highly reflective snow and water clouds are visible in AVHRR Channel 1, A(1), while coastline and inland lakes become more discernible in Channel 2, A(2). Snow is bright in both channels.

A(3) 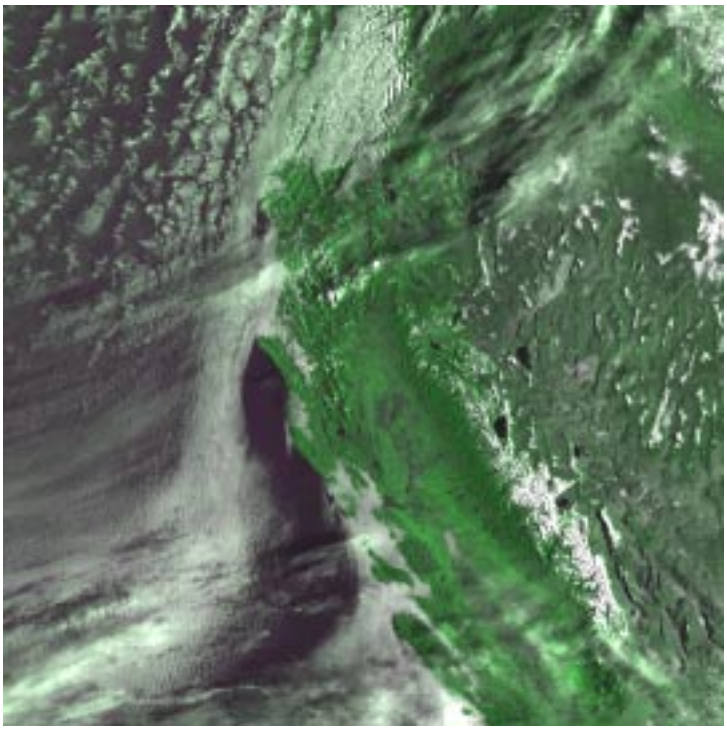

Panel A(3). False color composite of NOAA-12 AVHRR imagery shown was created by assigning Channel 1 to the red and blue guns and Channel 2 to the green gun of a CRT. This false color composite is useful for manually distinguishing between densely vegetated (rich green hue) and more sparsely vegetated (brownish hue) land as well as the water-land boundaries. Snow and clouds both appear bright in this color composite.

Figure 19. NOAA-12 AVHRR Channel 1 and Channel 2 imagery collected over western U.S. at 1505 GMT on March 19, 1996.

A(1) 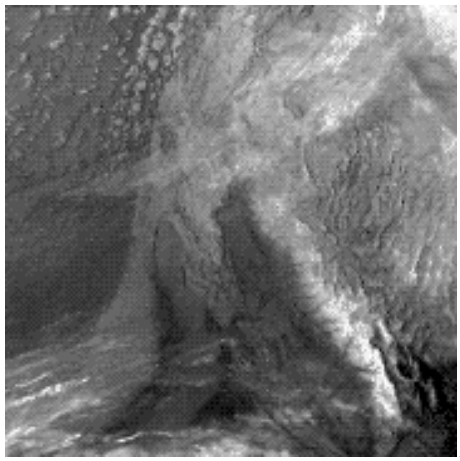 A(2) 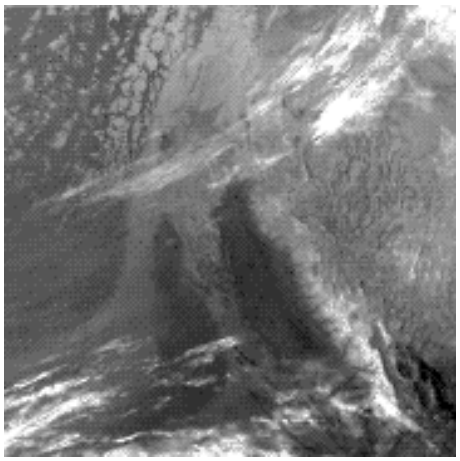

Panels A. Ice clouds and snow along the Sierra Mountain range, lower right quadrant, have a similar (bright) appearance in AVHRR channel 3, A(1), and channel 5, A(2), which makes distinguishing between them difficult.

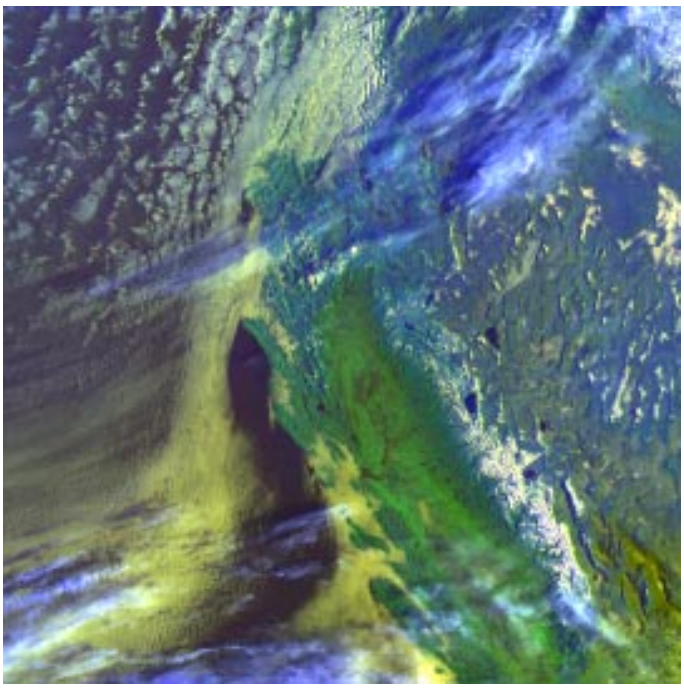

Panel A(3). The false color composite in A(3), created by assigning AVHRR Channel 1 to the red and blue guns and Channel 2 to the green gun of a CRT, is used to manually distinguish between densely (rich green hue) and more sparsely (brownish hue) vegetated land as well as the water-land boundaries. Snow clouds both appear bright in this color composite.

Figure 20. NOAA-12 AVHRR Channel 3 and Channel 5 imagery collected over western U.S. at 1505 GMT on March 19, 1996.

A(1) 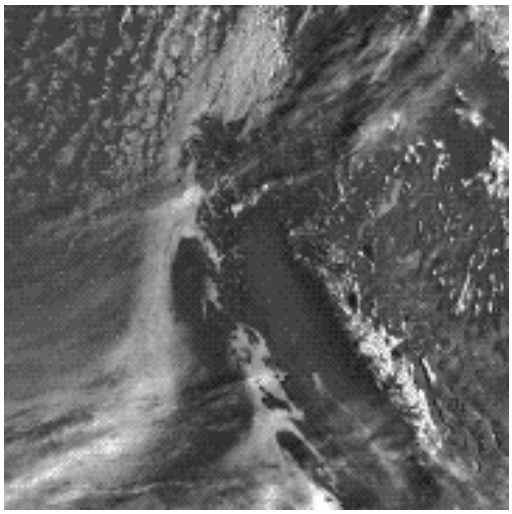 A (2) 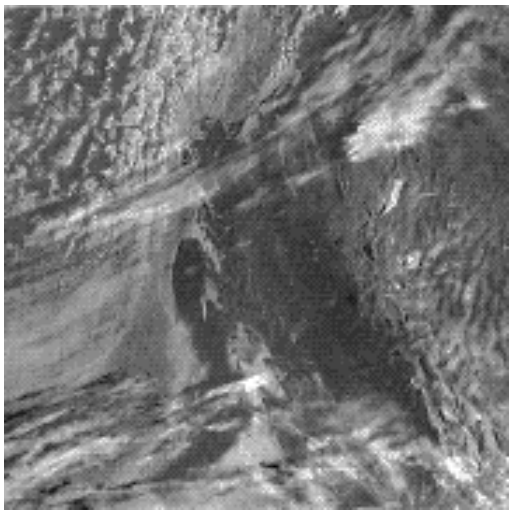

Panels A. The contrast between snow is greatly enhanced by correcting the 3.7-µm band for thermal emissions as seen by comparing the 0.6-µm band, A(1), with the 3.7-micron albedo data in A(2), and the brightness temperature difference image of channel 3 minus channel 5, C(2).

Figure 21. NOAA-12 AVHRR Channel 1 and the derived 3.7-µm (albedo) data for the scene collected 1505 GMT on March 19, 1996.

A(1) 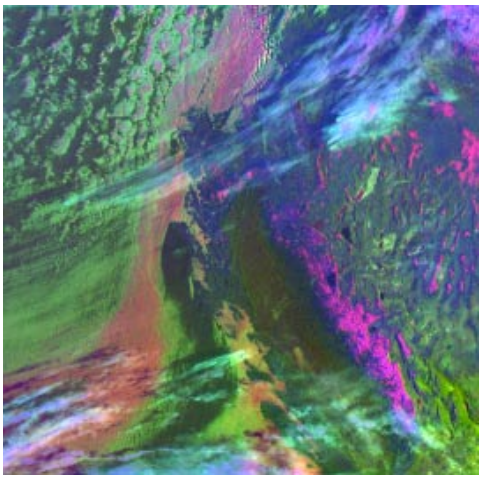 A(2) 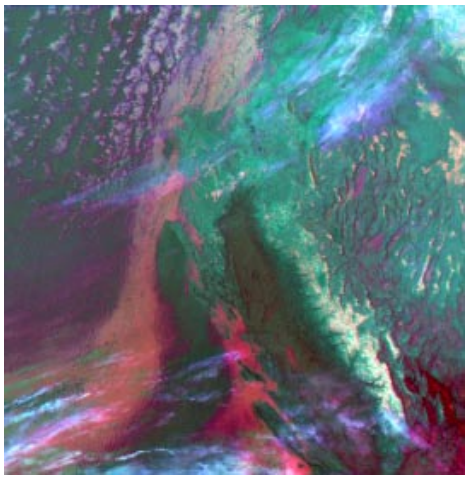

Panels A. The false color composite in A(1), created by assigning AVHRR Channel 1 to the red, the derived Channel 3a (albedo) to the green, and Channel 5 to blue gun of a CRT while Channel 3 replaces Channel 3a in A(2).

Figure 22. Color composite of NOAA-12 AVHRR imagery created by assigning Channels 1, 3, and 5 to the red, green and blue guns of a CRT.

The enhanced spectral signatures in channel 3a (albedo) greatly assist in manually distinguishing between ice clouds (blue) and snow (purple) in Panel A(2) of Figure 22. The clear distinction between thin cirrus and the snow-covered mountains in the lower-right quadrant results from the

spectral signatures of these features being very different in channels 1, 3a, and 5. In fact, it was found that the signature of snow in Panel A(1) of Figure 22 from the red and blue guns was nearly an order-of-magnitude greater than its signature in the green gun; thus, snow appears purple in the false color image, indicating nearly equal energy coming from the red and blue guns (channels 1 and 5). On the other hand, the signature of snow in Panel A(2) from the red, green, and blue guns is nearly the same for channels 1, 3, and 5; since equal contributions from each gun produces a gray shade rather than a color, snow appears white in this figure. Thin cirrus appears bluish in both panels because ice has its strongest signature in channel 5. However, it is important to note that more thin cirrus is evident in Panel A(1) than A(2) because the signature of thin cirrus in the combination of channel 3a and channel 5 is greater than its signature in channel 3 and channel 5. Finally, the large difference in the signature of snow between channel 3a and channel 1, shown in the false color composite of Panel A(1), means it is possible to positively identify snow-covered surfaces using an automated algorithm based upon the bi-spectral reflectance ratio between these two channels. It appears that the low clouds in Panel A(1), shown as red and occurring in the left half of the image, have a similar spectral signature to that of snow and therefore could be misclassified; however, this is not the case. In channel 3a, the spectral signature of snow is much weaker, by a factor of nearly 5, than the signature of low-level water clouds. In addition, the relative signature of warmer, water clouds is only slightly larger in channel 1 (the red gun) than in channel 5 (the blue gun) and this difference becomes smaller as the cloud tops become colder, i.e. the clouds change from low to middle level clouds. On the other hand, while the spectral signature of snow is much lower in channel 3a (the green gun) than the channel 1 (the red gun), it is even lower when compared to channel 5 (the blue gun) since snow-covered surfaces appear cold in channel 5. Thus, the channel 1, 3a, and 5 false color composite is a robust display for the manual identification of snow and thin cirrus in multispectral imagery (Hutchison *et al.*, 1997; Hutchison and Locke, 1997). Therefore, the threshold requirements for manual cloud detection and cloud typing in daytime imagery are satisfied using only the DV, MWIR, and LWIR imagery bands along with image processing techniques. The performance summary is provided in Section 3.4.4.

3.4.3.3 Mathematical Description of the Algorithm

The most important step in creating the manual Cloud-No Cloud (CNC) analysis is the accurate interpretation of all cloudy and cloud-free features in the multispectral images using (1) the principle set forth in Eq. 3.4.3.1.1, (2) image enhancement techniques, and (3) false color composites as previously described while (4) following guidelines that are well documented in the literature (Scorer, 1990). Once these features are identified, the manual cloud-no cloud (CNC) analyses is created from the analysis of individual bands of the multispectral imagery where these features, included edges, are most distinct. The cloud ground truth analysis (CGTA) software allows analysts to compare the spectral signatures of clouds and cloud-free surfaces in all spectral bands and use iterative techniques over subimage regions to create CNC analyses. Individual CNC analyses may be created from a single band or composited from as many as five spectral bands into a total CNC analysis. The operator may draw polygons around areas of interest in each channel and set threshold levels for declaring pixels in that area cloudy; thus, the need for strong contrasts between clouds and background features becomes apparent. Additionally, a composite (total cloud) analysis from one set of five channels for a scene can be updated with CNC analyses of another five bands of the same scene, e.g., if working with

hyperspectral imagery, to extend the total CNC analysis to include all clouds in 10 spectral bands and so forth. Thus, in theory, there is no limit to the number of spectral bands that may be used to create the manual CNC. In practice, only a couple bands are needed for skilled analysts to interpret features in a scene and create the manual CNC analysis with a repeatability of about 1-2 percent. Additionally, the accuracy of the manual CNC analysis is limited by image quality, i.e., clouds smaller than the sensor HSR may not be included in the manual analysis. Cloud Type ground truth (cirrus, stratus, cumulus) analyses are accomplished in a similar manner using only the areas already declared cloudy in the composite CNC mask as described in Hutchison *et al.* (1997).

3.4.3.4 VIIRS Imagery and Imagery Assist Color Composites

The Raytheon VIIRS design calls for a flowdown of imagery "sensing" requirements necessary to meet threshold Application-Related Requirements for the Imagery EDR. A minimum of three imagery channels are required to satisfy threshold requirements for the Manually-Generated Cloud Data (Hutchison, 1998). These are the daytime visible (DV) band, the Mid-Wave Infrared (MWIR) band, and the Long-Wave Infrared (LWIR) band.

Our VIIRS design also calls for imagery assist channels to be used with imagery channels to push toward NPOESS VIIRS Objectives. In the case of the Manually-Generated Cloud Data, this is readily accomplished using (1) false color composites and (2) the CGTA software concepts. The Imagery Risk Reduction Plan identifies the attributes of each Manually-Generated Cloud Data ARP for which pushing toward objective requirements is feasible (Hutchison, 1999). The performance summary for the Manually-Generated Cloud Data Product ARPs is provided in Section 3.4.4.

This section identifies the color composites recommended for the manual analysis of cloud cover and types with VIIRS imagery and imagery assist bands and discusses the colors present in the color composites. The approach assumed is one of "peeling an onion" in which information about the scene is gained incrementally as more VIIRS channels are used in color composites. While this approach may not ultimately be used in the time-constrained environment of a weather central, it is useful for training analysts in the interpretation of multispectral satellite meteorology. Training programs that incorporate imagery and the identification of cloud ARPs in the VIIRS User's Guide are planned, although not included here due to the size of these color imagery files based upon MODIS Airborne Simulator (MAS) data. Information from this section and Section 3.4.3.3 form the basis for the VIIRS User's Guide, which is included as an appendix to this version of the Imagery ATBD.

The generation of these color composites was done with MAS imagery. The methodology was discussed in the Imagery Technical Interchange Meeting (TIM; *[Y4963]*). This methodology is depicted in Figure 23.

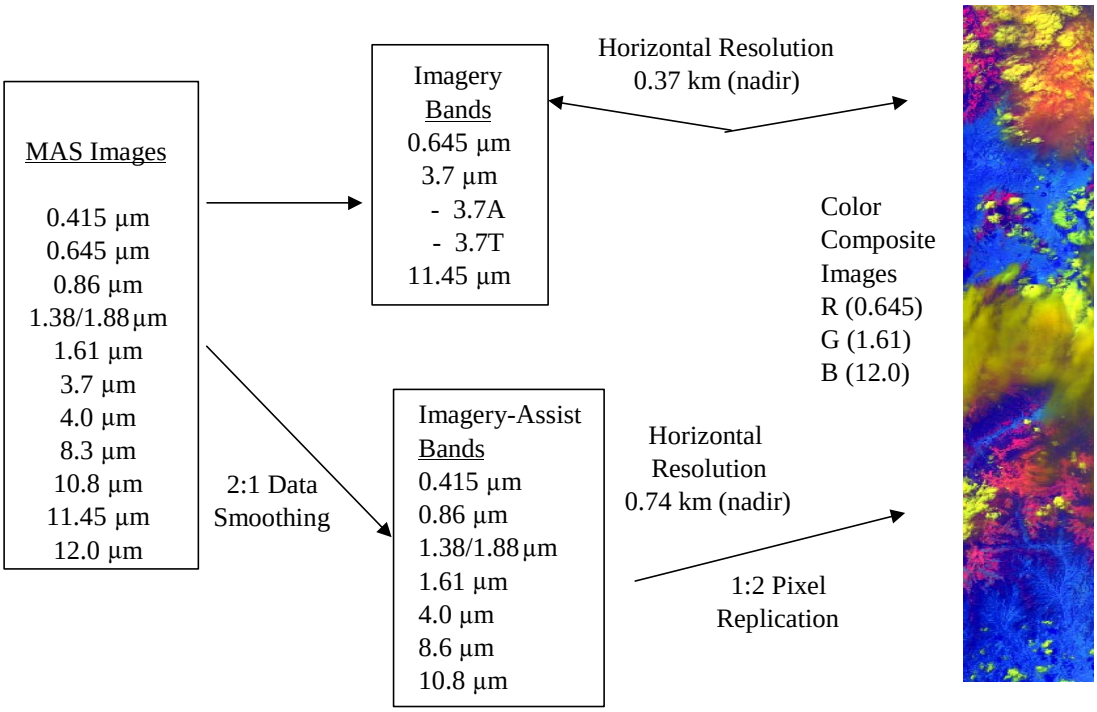

Figure 23. Methodology illustrated in using MAS data to construct Color Composites using Imagery and Imagery Assist bands.

VIIRS bands at 0.86 and 1.6 µm are also available at the resolution of the imagery bands. The analyst can use these with unsmoothed imagery bands to obtain some RGB color composites at imagery resolution.

Initially the MAS bands most spectrally similar to VIIRS were considered with reflectance determined for the Solar and NIR bands and brightness temperatures (BTs) determined for the thermal and crossover region bands. The imagery bands underwent no data smoothing, while the imagery assist bands went through 2:1 data smoothing. The final bandset used in the Color Composite generation was decided based upon the spectral information content of the bands used, and what distinct spectral features the cloud analyst wished to from the imagery. Note, this methodology is usable by VIIRS due to the spectral similarities that exist between the VIIRS and MAS/MODIS band sets.

Eighteen color composites were constructed from the VIIRS bandset after a careful survey of the spectral information content. All 18 Composites are included in the Appendix. Eight of these are discussed in this section.

1. Daytime Composite #1 – RGB (0.64, 1.61, 10.8./11.45): Figure 24

A traditional RGB composite that highlights a rich array of cloud and surface detail.

Feature Identification: Highlight differences between water clouds and snow

–Snow is rose – purple

–Low clouds are yellow;

–Higher (water) clouds range from yellow through green to light blue as the cloud temperature decreases.

Assists in separating low, middle, and high-level water clouds as a cloud typing objective

Ambiguities: Cirrus and snow are similar but can be differentiated

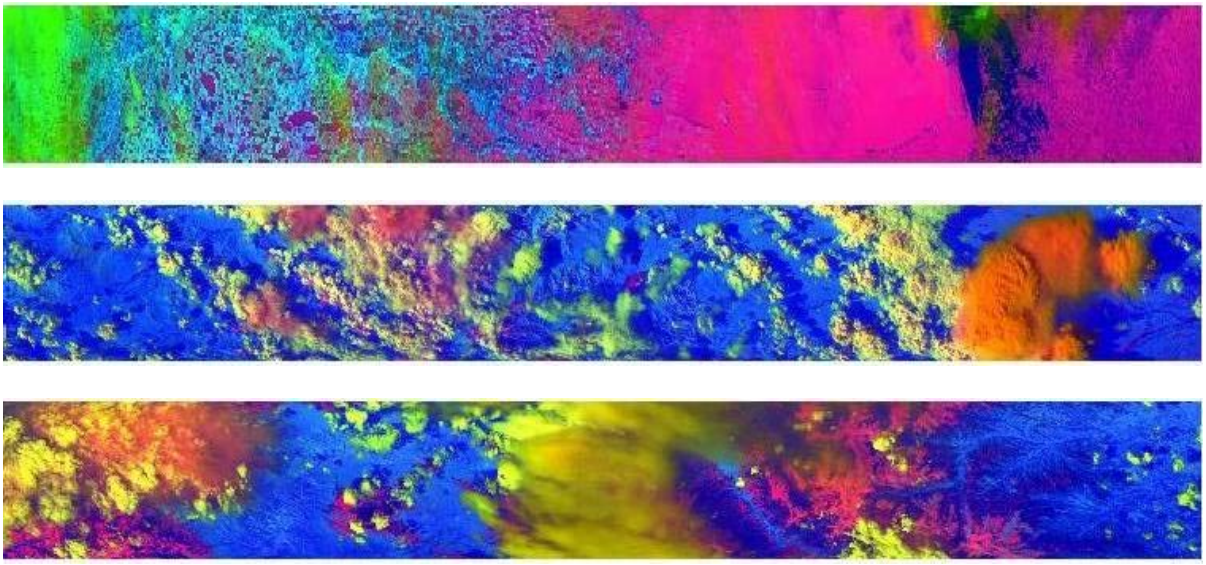

Figure 24. RGB Composites of bands (0.64, 1.61, 10.8./11.45)

2. Daytime Composite #2 - - RGB (1.38[1.88], 1.61, 11.45): Figure 25.

This composite brings out additional detail.

Feature Identification: Clear Distinction between cirrus and snow/ice fields

- Snow/ice fields are masked in 1.38 µm imagery
- The 11.45 µm imagery channel provides useful information on cloud top temperatures, when coupled with the 1.38 µm channel can be used to differentiate between cirrus and other cloud types
- Optically-thin cirrus has a deep bluish hue
- Lower-level water clouds appear greenish
- Optically thick cirrus are more golden and in some cases purple
- Overshooting tops, e.g. thunderstorms, appear orange or white-lavender (objective requirement)

Ambiguities: Little detail on snow and surface features. This composite may not provide great detail on cloud top temperatures, i.e. cloud heights, if large temperature variations exist in the scene.

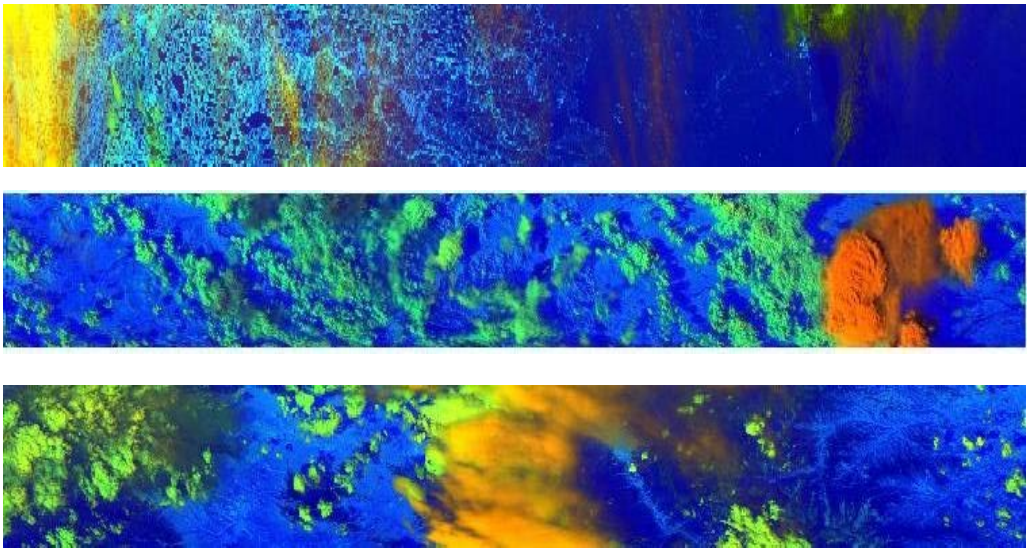

Figure 25. RGB Composites of bands RGB (1.38[1.88], 1.61,11.45)

3. Daytime Composite #3 - - RGB (1.61, Invert BT8.6, 0.64): Figure 26.

This composite brings out additional detail.

Feature Identification: Distinction between lower level Cumulus and upper level Cirrus and snow/ice fields

- Snow/ice fields are blue from 0.64 µm imagery
- Optically-thin cirrus has a greenish – turquoise hue due to contribution emissions at 8.6 µm
- Lower-level water clouds are rose to white
- Overlaying water clouds are darker blue

Ambiguities: Cirrus and snow may in some cases be the same color

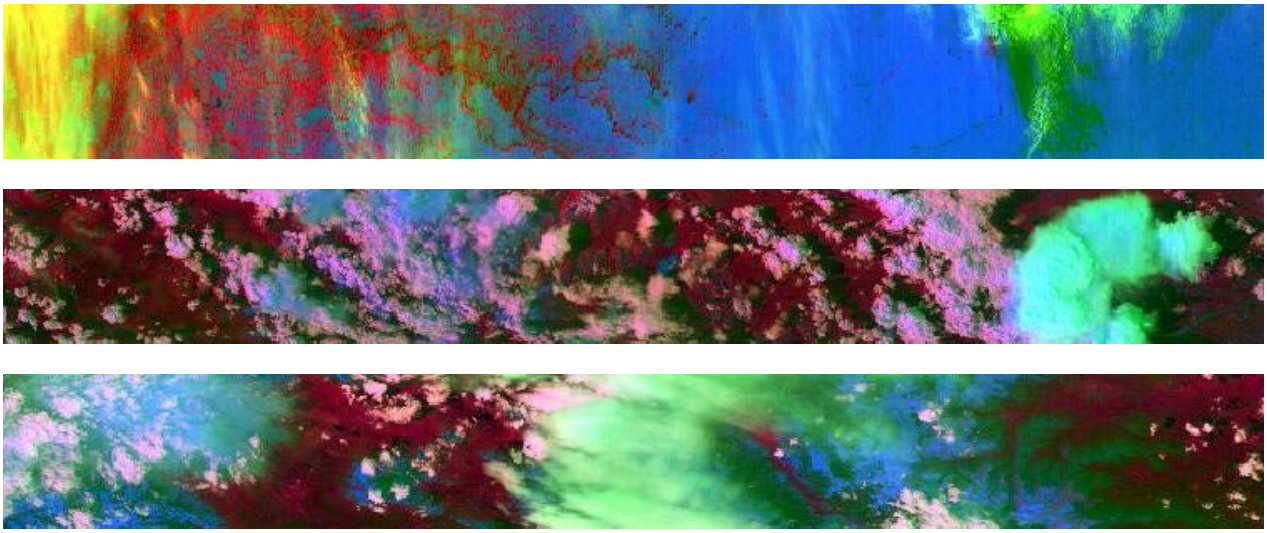

Figure 26. RGB Composites of bands RGB (1.61, Invert BT8.6, 0.64)

4. **Day/Night Composite #4** – RGB (BT11.45, BT8.6, BT3.75): Figure 27

This composite brings out additional detail.

Feature Identification: Distinction between lower level Cumulus and upper level Cirrus and snow/ice fields

- Snow/ice fields are olive-green from Thermal imagery
- Optically-thin cirrus has a deep blue-blackish hue over land and blue over ice
- Lower-level water clouds appear dark blue
- Vegetated regions tend to be white
- Overshooting tops, e.g. thunderstorms, appear black with dark clearly defined boundaries, and cellular structure clearly visible (objective requirement)

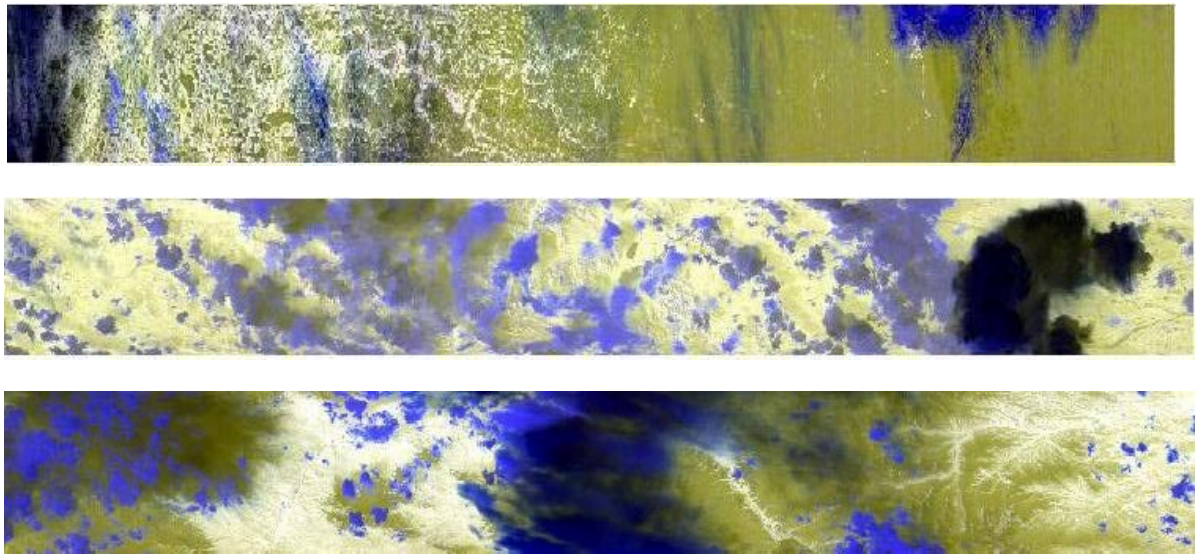

Figure 27. Day/Night Composite #4 – RGB (BT11.45, BT8.6, BT3.75)

5. Daytime Composite #5 – RGB (0.64, 0.858, 0.64), Figure 28.

Feature Identification: This is the well-known color composite design to highlight "vegetation" because vegetated regions are more highly reflective in the longer wavelengths that make these regions appear "green" in the false color composite. Separation of land and water surfaces is also readily accomplished with this composite that uses the 0.64 μm imagery channel with the 0.858 μm imagery assist channel.

Ambiguities: Several features appear gray shaded in this composite and might be ambiguous. For example, snow, water clouds, and non-vegetated regions may all appear as a shade of gray with snow and clouds being particularly difficult to separate.

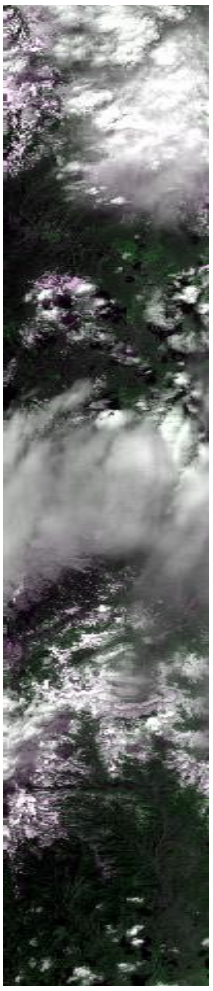

Figure 28. Color composite of MAS data collected over Denver, CO [RGB= (0.64 μm, 0.858 μm, 0.64 μm)].

6. Daytime Composite #6 – RGB (0.64, 1.61, 10.8), Figure 29.

Feature Identification: This is a relatively new color composite designed to highlight differences between water clouds and snow in newly acquired data from NOAA-15. The process renders the snow and ice white and most other surface features in natural colors. Low clouds are yellow; higher clouds range from yellow through green to light blue as the cloud temperature decreases. This composite assists in separating low, middle, and high-level water clouds as a cloud typing objective.

Ambiguities: Differentiation between snow/ice and cirrus clouds may be difficult, especially when they are approximately the same temperature in the 10.8 μm imagery channel, since these clouds are relatively transparent in the 0.64 μm imagery band, and both reflect poorly at 1.61 μm imagery assist channel. (These data were taken from the NOAA website at http://www.osei.noaa.gov/Events/Snow/NOAA15new for the grtlks.jpg example. Cirrus clouds are evident along with snow south of Lake Michigan but both appear white.)

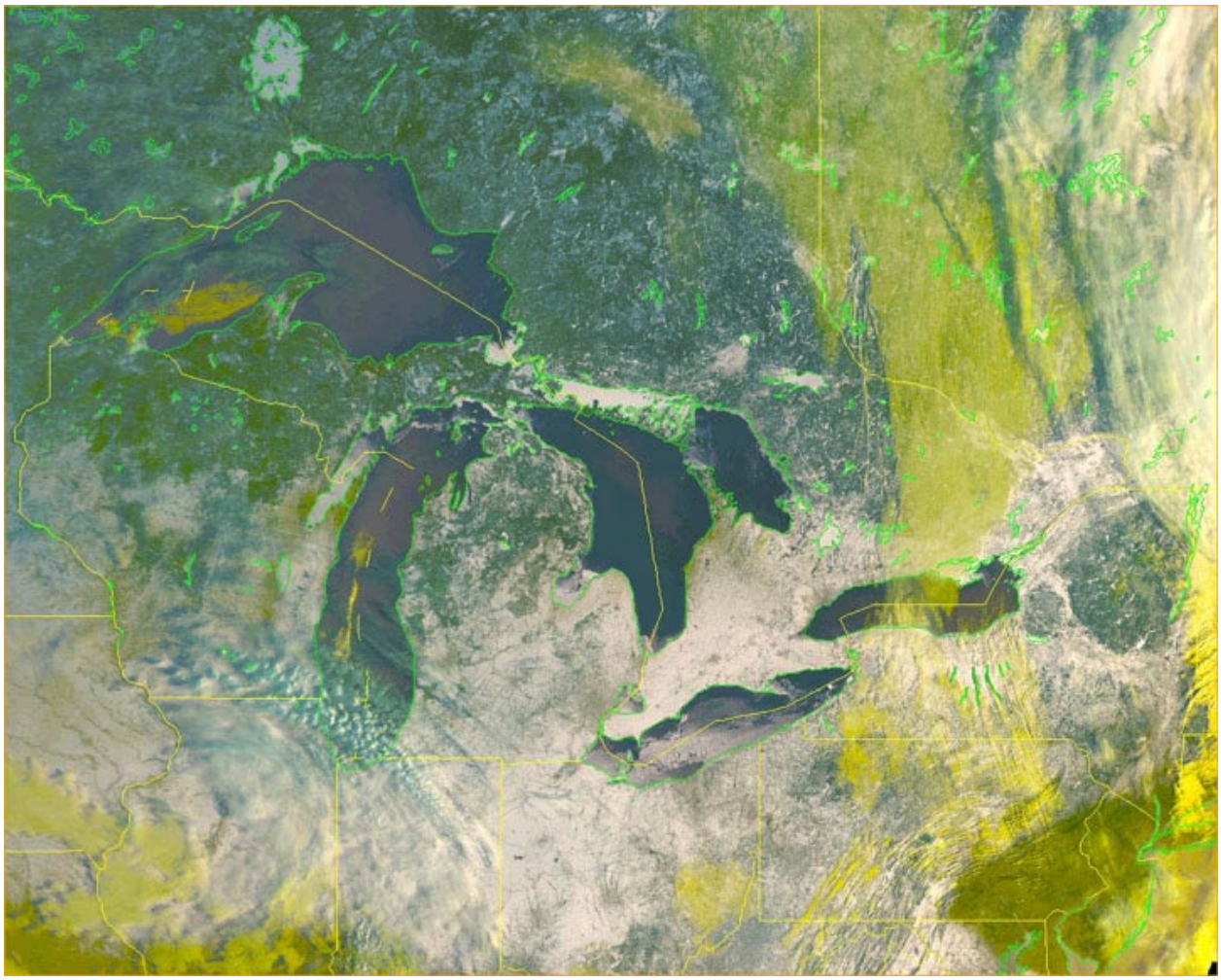

Figure 29. Color composite of NOAA-15 AVHRR imagery created by assigning the 0.64 μm, 1.61 μm, 10.8 μm channels to the red, green and blue guns of a CRT.

7. Daytime Composite #7 alternative – RGB (0.64, 1.61, 3.75 albedo), Figure 30a.

   Feature Identification: This color composite is also designed to highlight differences between water clouds and snow but provides better differentiation between optically-thin cirrus clouds and snow/ice since the 3.75 µm albedo imagery channel has the appearance of a 3.75 µm minus 10.8 µm brightness temperature difference fields. Therefore, the cloud/cloud discrimination is more accurate. Vegetated land appears green, snow fields are red, optically thick clouds appear yellow to white, while optically thin water (edges) clouds appear bluish. Thin cirrus clouds appear a deep orange because their signatures is more strongly suppressed in the 3.75 µm albedo band than in the 1.61 µm imagery assist channel while thick cirrus appears reddish since it is highly reflective in the 0.64 µm imagery channel while nearly equal in the other two channels.

   Ambiguities: This composite provides no information on cloud top temperatures as does the RGB (0.64, 1.61, 3.75) since the process renders the snow and ice white and most other surface features in natural colors. Care must be taken in this composite since the 3.75 µm channel measures optical thickness, not temperatures. Therefore, edges of a stratocumulus cloud, for example, may be a different color than pixels located at center of the cloud.

8. Nighttime Composite #9 – RGB (3.75, 10.8,11.45), Figure 30b.

   Feature Identification: This is the well-known color composite design to highlight stratus clouds (which appear reddish due to their lowest emissivity in the 3.75 µm imagery) and optically-thin cirrus clouds, which appear bluish due to their coldest temperatures in the 11.45 µm imagery channel.

   Ambiguities: This composite may not provide great detail on cloud top temperatures, i.e. cloud heights, if large temperature variations exist in the scene.

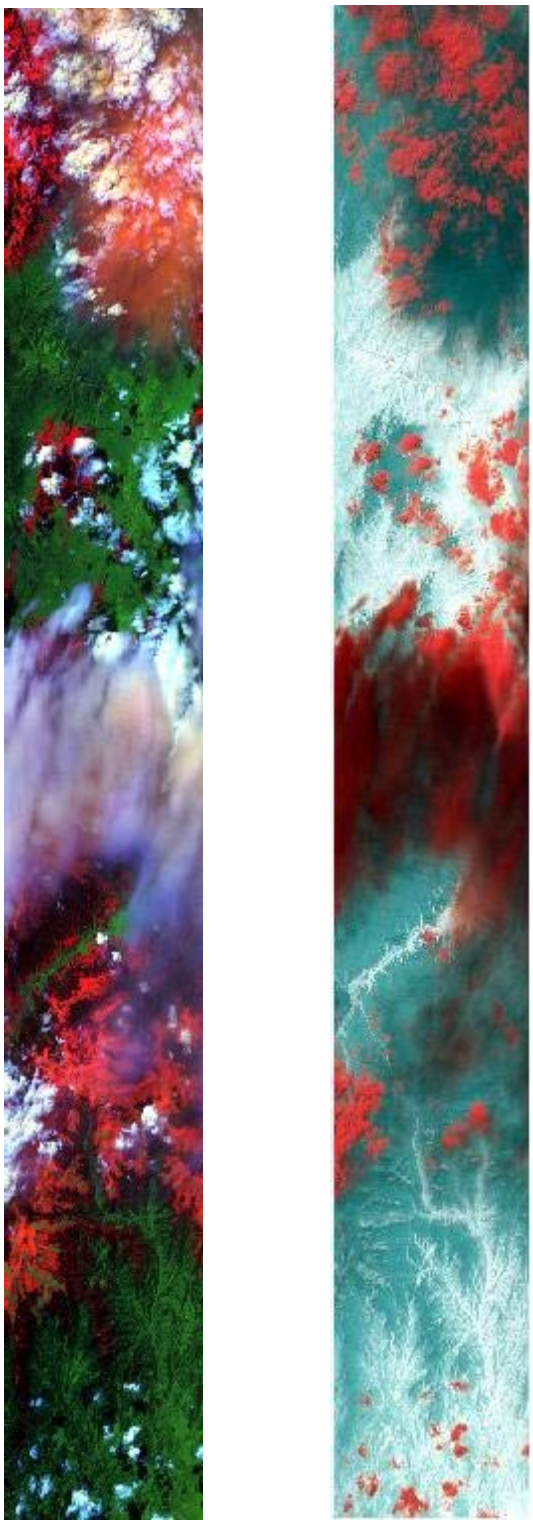

(a) **(b)**

Figure 30 (a.) Color Composite of MAS imagery over Denver, CO [RGB (0.64, 1.61, 3.75 albedo] (b.) [RGB (3.75, 10.8,11.45)]

Generation of these RGB composites greatly assists the manual analyst in determining cloud type and also to increase confidence in the cloud cover determination. Use of RGB composites will result in fewer Quality Control (QC) bogus operations and assist the manual cloud analyst in determining cloud type for many of the objective cloud types. The biggest improvement will be in the fact that the manual analyst will have improvements in meeting critical time schedules by using RGB composites.

The Raytheon VIIRS team has identified the need for a "VIIRS User's Guide" for the interpretation of imagery and has developed the structure of this publication. It is needed because:

Current OLS & AVHRR sensors are spectral content limited. Analysts using these data are accustomed to "seeing" clouds and different backgrounds in only five spectral bands. VIIRS extends MODIS a leap forward into an operational context. MODIS contains 36 spectral bands but these data are only used in a research environment. VIIRS will provide all the value of MODIS for manual cloud analyses in the operational environment within a 20 minute time frame.

Algorithm technology and user knowledge must be brought forward to fully realize value of true multispectral VIIRS measurements. The VIIRS automated cloud analysis algorithms exploited the spectral signatures of these data to generate the cloud cover product. It is therefore essential that those who perform manual quality control of these automated products be expert in the knowledge of spectral signatures in these bands. Thus, it becomes necessary to educate the users of the VIIRS data. A VIIRS User's Guide is the one highly beneficial approach to help facilitate this education process

3.4.3.5 VIIRS Cloud Mask for Imagery

In addition to the Imagery and Imagery assist bands the analyst will also have access to the Cloud Mask Intermediate Product (IP). The Cloud Mask is an automated algorithm done within the VIIRS Data Processing Architecture. The objective of the VIIRS Cloud Mask (VCM) is to determine if a given Field of View (FOV) has a cloud present. The VCM is defined as the pixel level flag that indicates when a line segment extending between the sensor and a given area of the Earth's surface is intersected by a cloud. The cloud mask IP includes a binary cloudy/not cloudy flag operating at the pixel level using VIIRS radiance data. The VCM operates at the moderate resolution (750 m at nadir), and at the imagery resolution (375 m at nadir). Also output by the VCM in addition to the binary cloudy/not cloudy flag are many processing flags and test result indicators, which are available to the imagery analyst to use for assisting in Cloud Cover and Cloud Type assessment.

Imagery Resolution Cloud Mask

The VIIRS imagery resolution pixels 'nest' with the moderate resolution pixels, as depicted in Figure 31.

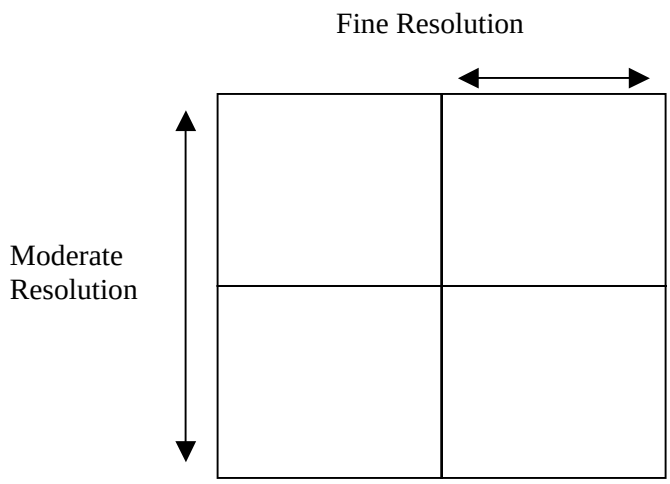

Figure 31. Depiction of the Nesting of the VIIRS Imagery (Fine) Resolution Bands within the VIIRS Moderate Resolution Bands

This nesting allows the inclusion of an imagery resolution cloud mask along with the VCM output. Cloud tests performed with the 0.64, 0.865, 1.6, 3.74, and 11.45 micron bands are reported at the imagery resolution, and have spectral contrast tests performed upon them, along with tests being performed at the finest resolution they offer. These tests performed are based upon BT and Reflectance Thresholds that are MODIS and AVHRR (CLAVR) in heritage. The details of the tests performed to detect clouds from the imagery resolution bands are discussed in the VCM ATBD *[Y2412]*.

The primary benefit to mention to the imagery analyst is that the physical scale of the imagery resolution cloud mask is consistent with that which the analyst will view the imagery. Due to this scale similarity fine details in the imagery being analyzed may be identified. The greatest benefit to the cloud analyst however will be that the Quality Control of the automated analysis will improve analysts capabilities. Cloud edge pixels that are difficult to discern with the moderate resolution cloud mask will be more readily detectable with use of the imagery resolution mask. Pixels containing thin cloud optical depths at subpixel resolution, which the moderate resolution cloud mask might not detect, may be detectable at the imagery resolution. Finally smaller clouds may be detected and small scale cloud features may be brought out to assist in the cloud typing of the analyst.

Cloud Mask Output of Use to the Analyst

Table 10 lists the VCM IP output *[Y2412]*. The output is composed of 64 bits per moderate resolution pixel. Each of these bits, or combination of bits, is used to denote a particular flag or product of use to other EDRs located in the Data Processing Architecture. Most of the bits are at the moderate pixel resolution. The last fifteen bits are reserved to report cloud/no cloud at fine pixel resolution. The data contained within the VCM IP are of use to the cloud analyst as well. Analysts can learn from experience how to use the bits of the Cloud Mask IP to assist them.

Table 10. 64 Bit Intermediate Product output of the VIIRS Cloud Mask

BIT FIELD	FLAG DESCRIPTION KEY	RESULT
0-3	Cloud Mask Quality	0000 = 0% to 1010 = 100% 1011 to 1111 = Spares
4-5	Cloud Detection Result and Confidence Indicator	00 = Confident Cloudy 01 = Probably Cloudy 10 = Probably Clear 11 = Confident Clear
6	Day / Night	0 = Night 1 = Day
7	Snow / Ice Surface	0 = Snow/Ice 1 = No Snow/Ice
8-10	Land / Water Background	000 = Land and Desert 010 = Land no Desert 110 = Inland Water 111 = Sea Water 100 = Coastal
11	Sun Glint Wind Executed	0 = Yes 1 = No
12-13	Sun Glint	00 = Geometry & Wind Speed Based 01 = Geometry Based 10 = Wind Speed Based 11 = No Sun glint
14	Shadow Test Executed	0 = Yes 1 = No
15	Shadow Detected	0 = Yes 1 = No
16	Non Cloud Obstruction Test Executed	0 = Yes 1 = No
17	Non Cloud Obstruction (Heavy Aerosol)	0 = Yes 1 = No
18	Fire Test Executed	0 = Yes 1 = No
19	Fire Detected	0 = Yes 1 = No
20	Thin Cirrus (Solar) Test Executed	0 = Yes 1 = No
21	Thin Cirrus Detection (Solar) ($R_{1.38}$)	0 = Cloud 1 = No Cloud
22	Thin Cirrus (IR) Test Executed	0 = Yes 1 = No

BIT FIELD	FLAG DESCRIPTION KEY	RESULT
23	Thin Cirrus Detection (IR) (BT_{11}- BT_{12})	0 = Cloud 1 = No Cloud
24	IR Threshold Test (BT_{11}) Executed	0 = Yes 1 = No
25	IR Threshold Cloud Test (BT_{11})	0 = Cloud 1 = No Cloud
26	High Cloud Test ($BT_{3.7}$- BT_{12}) Executed	0 = Yes 1 = No
27	High Cloud Test ($BT_{3.7}$- BT_{12})	0 = Cloud 1 = No Cloud
28	IR Temperature Difference Test Executed	0 = Yes 1 = No
29	IR Temperature Difference Test ($BT_{8.6}$- BT_{11} & BT_{11}- BT_{12})	0 = Cloud 1 = No Cloud
30	Temperature Difference Test (BT_{11}-$BT_{3.7}$) Executed	0 = Yes 1 = No
31	Temperature Difference Test (BT_{11}-$BT_{3.7}$)	0 = Cloud 1 = No Cloud
32	Temperature Difference Test ($BT_{3.7}$-$BT_{4.0}$) Executed	0 = Yes 1 = No
33	Temperature Difference Test ($BT_{3.7}$-$BT_{4.0}$)	0 = Cloud 1 = No Cloud
34	Visible Reflectance Test ($R_{.67}$) Executed	0 = Yes 1 = No
35	Visible Reflectance Test ($R_{.67}$)	0 = Cloud 1 = No Cloud
36	NIR Reflectance Test ($R_{.86}$) Executed	0 = Yes 1 = No
37	NIR Reflectance Test ($R_{.86}$)	0 = Cloud 1 = No Cloud
38	Reflectance Test ($R_{.86}$ / $R_{.67}$) Executed	0 = Yes 1 = No
39	Reflectance Test ($R_{.86}$ / $R_{.67}$)	0 = Cloud 1 = No Cloud
40	Cloud Adjacency Execution Flag	0 = Yes 1 = No
41-42	Adjacent Pixel Cloud Confident Value	00 = Confident Cloudy 01 = Probably Cloudy 10 = Confident Clear 11 = Probably Clear
43-44	Cloud Phase	00 = Not Executed 01 = Water 10 = Ice 11 = Mixed

BIT FIELD	FLAG DESCRIPTION KEY	RESULT
45-47	Cloud Phase Path Indicator	001 = path 1 to 111 = path 7
48	Spare	
49	Cloud Imagery Resolution BTD Test Executed (BTD = I5 – I4)	0 = Yes 1 = No
50	Cloud Imagery Resolution R(I1) Test Executed	0 = Yes 1 = No
51	Cloud Imagery Resolution R(I2) Test Executed	0 = Yes 1 = No
52-55	Cloud Imagery Resolution BTD Test	0000 = Cloudy 1111 = Not Cloudy Each bit is a pixel of the 2x2 imagery resolution pixels nested in the radiometric resolution pixel: 0000 = all cloudy, 1111 = all clear
56-59	Cloud Imagery Resolution R(I1) Test	Same as BTD Test Result
60-63	Cloud Imagery Resolution R(I2) Test	Same as BTD Test Result

3.4.4 Performance of Manually-Generated Cloud Data

The performance of manually-generated cloud data with respect to the VIIRS requirements and the system specification (c.f. Tables 3 and 4) is reviewed in this section.

The performance analysis was conducted as part of the SRD requirements flowdown to the sensor, as described in Section 2.5 and documented by Hutchison (1998). A brief overview of the methodology is provided here.

VIIRS sensing requirements were established using a series of simulations. To define these requirements for the manually generated cloud data product, the following simulation scenarios were defined and results of the simulations are shown in the Appendix:

Case 1: Stratus at Night

Case 2: Daytime and Nighttime Cirrus

Case 3: Cloud Typing (Stratus versus Cirrus)

Case 4: Cumulus

Case 5: Daytime Obscurations

All simulations were performed over a variety of surface backgrounds, as shown in Figure 32, including ocean, sand, fresh snow, and mixed vegetation. Values for spectral reflectivities and absorptivities were taken from the data base in the Space-Based Infrared System (SBIRS) toolkit. Later, it was verified that identical values were used in MOSART once this software package was released by the NPOESS IPO to Raytheon. Radiative transfer computations were made within PACEOS™, which can generate imagery scenes using MODTRAN 3.5 and later MODTRAN 3.7, after it was released by the IPO.

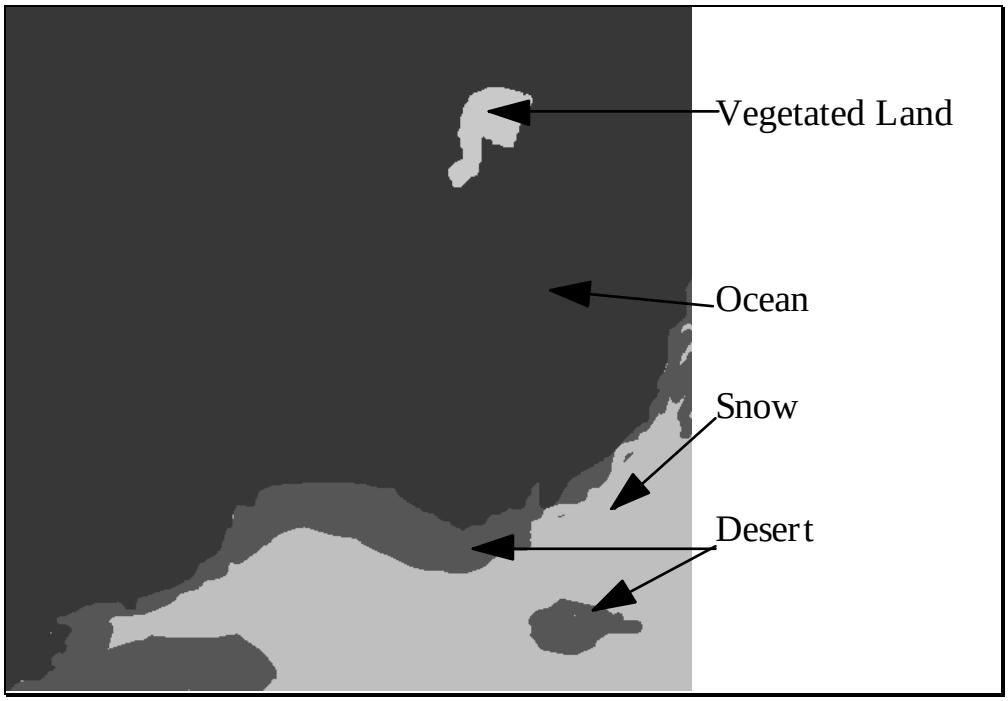

Figure 32. VIIRS sensing requirements were based upon a variety of surface classifications.

Recommended values for TBRs and TBDs were created by running a series of simulations using results of manual cloud analyses on simulated clouds of different optical thickness. Statistics were developed between the manual analyses and the binary cloud maps (ground truth or a priori analyses) input into PACEOS™ at the start of each simulation.

Results are shown for cirrus clouds. The detection and typing of cirrus clouds (Case 2) is a driving requirement for VIIRS imagery. This case was simulated using four different visible optical depths, i.e. 0.003, 0.008, 0.015, and 0.030 along with models for sensor noise generated by Santa Barbara Remote Sensing (SBRS). All analyses were performed using only the simulated 12.0-µm VIIRS imagery channel. Manual cloud cover analyses were created from the synthetic

imagery and compared against the binary cloud map which was input PACEOS™ to generated the simulations. Results were then summarized using definitions of measurement accuracy, precision, and uncertainty as defined in Appendix A of the NPOESS SRD dated April 17, 1997.

Figure 33 illustrates the results of a simulation that satisfies the requirements for cloud cover Measurement Uncertainty.

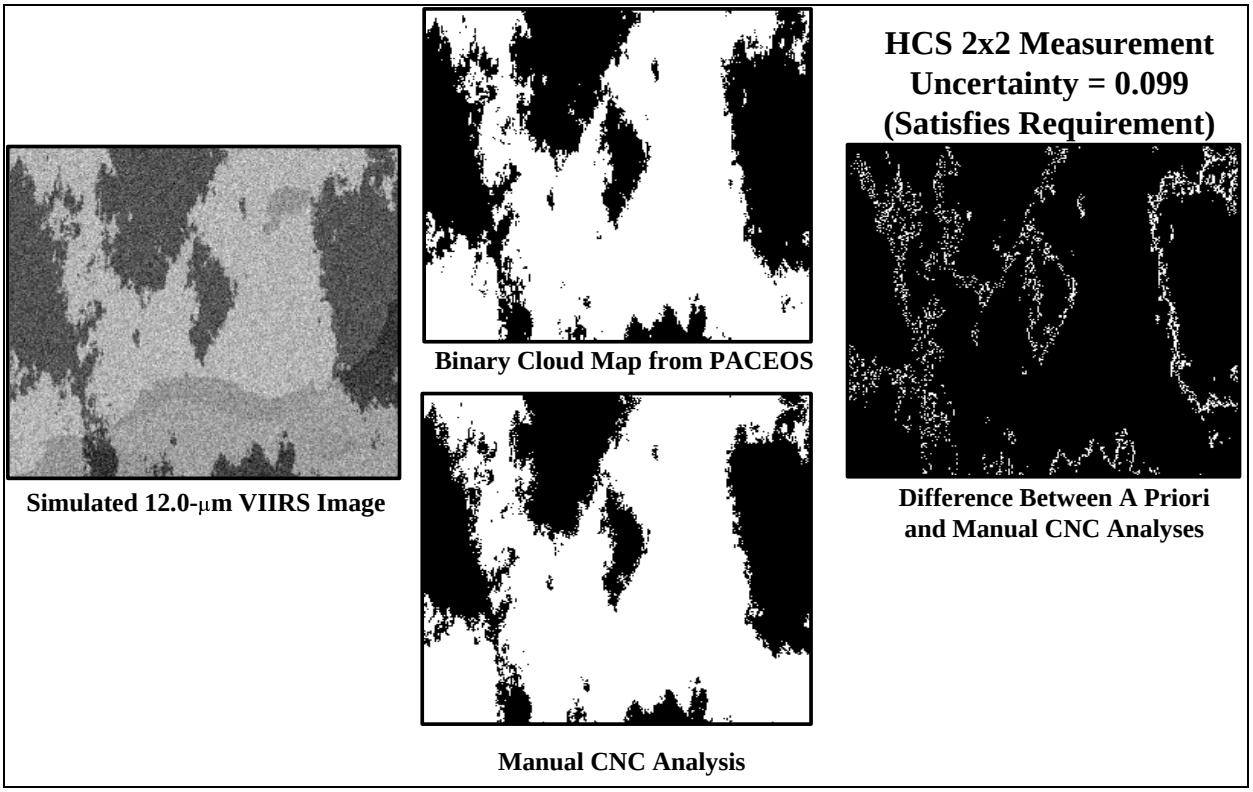

Figure 33. Measurement uncertainty based upon manually-generated cloud analysis of simulated VIIRS 12.0-μm imagery created for cirrus optical depth 0.03.

3.4.4.1 Cloud Cover

The sensor noise model used for the simulation shown in Figure 33 is noisier than the sensor specification. As a result, the specification provides margin against the requirement. Table 11 shows the Cloud Cover measurement uncertainty errors, determined using the procedures

described above, stratified by cloud type. Performance is for a horizontal cell 3 times the imagery HSR, and is based on the sensor noise specification. Actual sensor performance is expected to be better than the specification.

Table 11. Cloud Cover Measurement Uncertainty

Cloud Type	Status (Nighttime)	Cirrus	Cumulus (Daytime)	Obscured Not Cloudy
Measurement Uncertainty	0.027	0.078	0.04	0.041

These results demonstrate that the predicted performance satisfies threshold requirements with margin, even for the driving case of thin cirrus.

Additional analyses were also completed to determine the capability of the human analyst to satisfy VIIRS Objective Requirements for the manually-generated cloud cover ARP. Results are based upon the manual detection of cirrus clouds, which is the worst case scenario. These results are shown in Table 12 and demonstrate that the measurement uncertainty remains below 0.1 for HCS 2 times HSR, which is the only attribute that changes between the VIIRS Threshold Requirement and Objective Requirement for the manually-generated cloud cover ARP. Therefore, the imagery channels selected for the VIIRS sensor also allow the analyst to satisfy the VIIRS Objective Requirements for manually-generated cloud cover, even though there is little margin. (Blue denotes VIIRS Objective Requirements are satisfied for this ARP.)

Table 12. Measurement Uncertainty versus HCS from manual analysis of cirrus with visible optical depth of 0.03.

HCS	NUMBER OF HCS PIXELS IN SIMULATONS			BI-MODAL	UNCERTAINTY
(2 x 2 pixels)	Total	Clear	Overcast	(Percent)	(Fraction)
Truth	16,129	10,363	4677	93.25	n/a
Analysis	16,129	10,124	4969	93.58	0.099
(3 x 3 pixels)					
Truth	7140	4417	1890	88.33	n/a
Analysis	7140	4364	2010	89.27	0.078
(4 x 4 pixels)					
Truth	3969	2389	967	84.56	n/a
Analysis	3969	2373	1049	86.22	0.069
(8 x 8 pixels)					
Truth	961	528	170	72.63	n/a
Analysis	961	529	194	75.23	0.050
(25 x 25 pixels)					
Truth	100	40	3	43.00	n/a
Analysis	100	40	6	46.00	0.032

The threshold HCS requirement, shaded green, is 3 x 3 pixels. The objective HCS requirement, shaded blue, is 2 x 2 pixels. The results shown in Table 12 were obtained with the LWIR band, using a sensor model with more noise than the current specification (c.f. Section 2.2, Table 2).

Table 12 also shows the relationship between HCS and measurement uncertainty of manually-generated cloud cover analyses. (Blue denotes success in meeting Objective Requirements; Green is success in meeting Threshold Requirements.) VIIRS pixels are classified as either completely cloudy or completely cloud-free by the human analyst, which makes the distributions completely bi-modal at the HSR level. As these pixel data are aggregated to the reporting interval, these distributions become less bi-modal as the HCS size increases. Thus, the larger the HCS, the less likely it is be perfectly correct but more important they are also less likely to be completely in error when compared to the a priori cloud map used to build the simulated VIIRS imager. The result is that the Root Mean Square Error (RMSE) measurement uncertainty becomes smaller as the HCS becomes larger. At HCS 2x2 HSR, the measurement uncertainty for the manually-generated analysis of cirrus in simulated VIIRS imagery using only the LWIR band is 0.099. The Objective requirement is 0.1 at this HCS; therefore, the objective requirement is satisfied.

3.4.4.2 Cloud Type

Three characteristics of clouds are considered by the human analyst in creating the Manually-Generated Cloud Type ARP. These characteristics include:

(1) Cloud spectral signatures: in general, stratus clouds are colder in the 3.75 micron band than the 11.45 micron band while the reverse is true for thin cirrus clouds.

(2) Cloud top temperatures: in general, water clouds can be segregated into lower level and higher level clouds based upon their temperatures in the 11.45 micron band. For example, comparison of the cloud top temperature to cloud-free surface temperatures of the neighbor regions allows the analyst to estimate cloud top height, using the general rule that temperature decreases approximately 6 degrees Kelvin for every kilometer in the troposphere. This approach allows stratocumulus (low clouds) to be readily differentiated from altocumulus (middle clouds).

(3) Texture: in general, cumuliform clouds are readily differentiated from stratiform clouds and cirrus clouds are identified by texture. For example, cirrocumulus associated with the jet stream is famous for its “fishbone” appearance.

These characteristics can be combined to identify additional cloud types. For example, texture allows standing lenticular clouds to be identified and cloud top temperatures allow stratocumulus standing lenticular clouds to be separated from altocumulus standing lenticular clouds while spectral signatures allow cirrocumulus standing lenticular clouds to be identified.

Based upon the spectral signatures, cloud top temperatures, and the Raytheon VIIRS imager design, we believe it is possible to positively identify 13 of the 17 cloud types listed as Objective Requirements for the Cloud Type ARP, including all cloud types listed as Threshold

Requirements. This list and techniques used for positive identification are shown in Table 13. Examples of the applications of these techniques are contained in Appendix A.

Table 13. Approach to the positive identification of cloud types by human analysts using VIIRS imagery and imagery assist bands.

Cloud Type	Abbreviation	Approach to Accurate Classification			Comments
		Spectral Signature	Shape/Texture	Temperature Contrast (cloud top vs cloud-free)	
Altocumulus	AC		x	x	
Altocumulus Castellanus	ACCAS				small scale features
Altocumulus (Standing Lenticular)	ACSL		x	x	
Altostratus	AS		x	x	
Cirrocumulus	CC	x	x	x	
Cirrocumulus (Standing Lenticular)	CCSL	x	x	x	
Cirrostratus	CS	x	x	x	
Cirrus	CI	x	x	x	
Cumulonimbus	CB	x	x	x	
Cumulus	CU		x	x	
Cumulus Fractus	CUFRA				small scale features
Towering Cumulus	TCU		x	x	
Stratus Fractus	STFRA				small scale features
Nimbostratus	NS				requires ancillary precipitation data
Stratocumulus	SC		x	x	
Stratocumulus (Standing Lenticular)	SCSL		x	x	
Stratus	ST	x		x	
Obscured/Not Cloudy	OBS	x	x		
Clear	CLR	x			

Cloud types achieved for Threshold Requirements are shaded green. Cloud types achieved for Objective Requirements are shaded blue. Unshaded cloud types are unachieved objective requirements.

The imagery channels chosen to satisfy the requirements for cloud cover also allow the threshold cloud types, listed in the table, to be identified with little or no ambiguity based upon unique spectral signatures, texture, and shape. Therefore, the minimum cloud typing can be completed with very high (>95%) probability of being correct.

The four cloud types that cannot be identified directly with VIIRS imagery and imagery assist bands are nimbostratus, cumulus fractus, stratus fractus, and altocumulus castellanus. Nimbostratus is only differentiated from altostratus by the occurrence of rain, which cannot be positively identified by the VIIRS alone. The other unidentifiable cloud types involve all fractus-type clouds that are identified by small scale features indicative of atmospheric instabilities. The small scale features are observable by the human on the ground but not by a satellite with a 400 meter horizontal spatial resolution at 833 km in space.

3.4.5 Initialization and Validation

Initialization and validation activities can best be accomplished in coordination with the U.S. Air Force Weather Agency (AFWA), which is the primary customer for the manual and automated cloud data product EDRs, as described in Section 2.4.2. The purpose of these activities is to assure that:

(1) VIIRS data products can be incorporated into the automated Cloud Depiction and Forecast System (CDFS)

(2) Human analysts have the necessary skills to fully exploit the VIIRS imagery in the quality control (BOGUS) process. This initialization and validation process assumes that the CDFS program will provide AFWA with the capability to construct color composites (as described in Section 3.4.3.2) within the Satellite Data Handling System (SDHS) and that there exists an interactive environment which allow analysts to exploit these color composites in the quality control process to ensure the benefits of an operational test and evaluation program are fully achieved in an operational setting prior to the launch of the first VIIRS sensor.

While the development such a test and evaluation program will require the participation of numerous agencies (including the NPOESS IPO, AFWA, and Raytheon VIIIRS team), the proposed approach could utilize MODIS imagery and automated cloud data products (i.e. automated cloud cover and cloud top height EDRs) obtained from the Earth Observing System Data and Information System (EOSDIS) as test data sets for initialization of the CDFS software environment. Analysts would be given access to MODIS imagery. Training on the exploitation of these data sources could be based upon the VIIRS User's Guide. The User's Guide, which has been further developed in Phase II, is included as an appendix to this document. This approach to an initialization and verification program is highly desirable since it would leverage existing software at AFWA and the analysts needed to provide an independent assessment of the VIIRS imagery.

The pre-launch characterization and post-launch validation plan for the VIIRS Cloud EDRs will be extended to the Manually Generated Cloud Data. Details are discussed in the VIIRS System Verification and Validation Plan Document *[TP 154640-001]*.

3.5 SEA ICE DATA PRODUCT DESCRIPTION

3.5.1 Processing Outline

The sea ice data products are retrieved by an automated algorithm (ice edge location, ice concentration) and by manual analysis (leads and polynyas, data assimilation). As with cloud data products, the manual analysis is not part of the VIIRS operational system. It will be performed at various ice centers by trained analysts using established techniques. The ice concentration is derived by application of the tie point method, as discussed in Section 3.5.3.2. We retrieve and report the fraction of ice cover for each imagery pixel as the ice concentration product.

The process flow for the automated production of Imagery Sea Ice Data is implemented in three independent testable software units, Ice Quality, Ice Concentration, and Ice Edge Location, as illustrated in Figure 34.

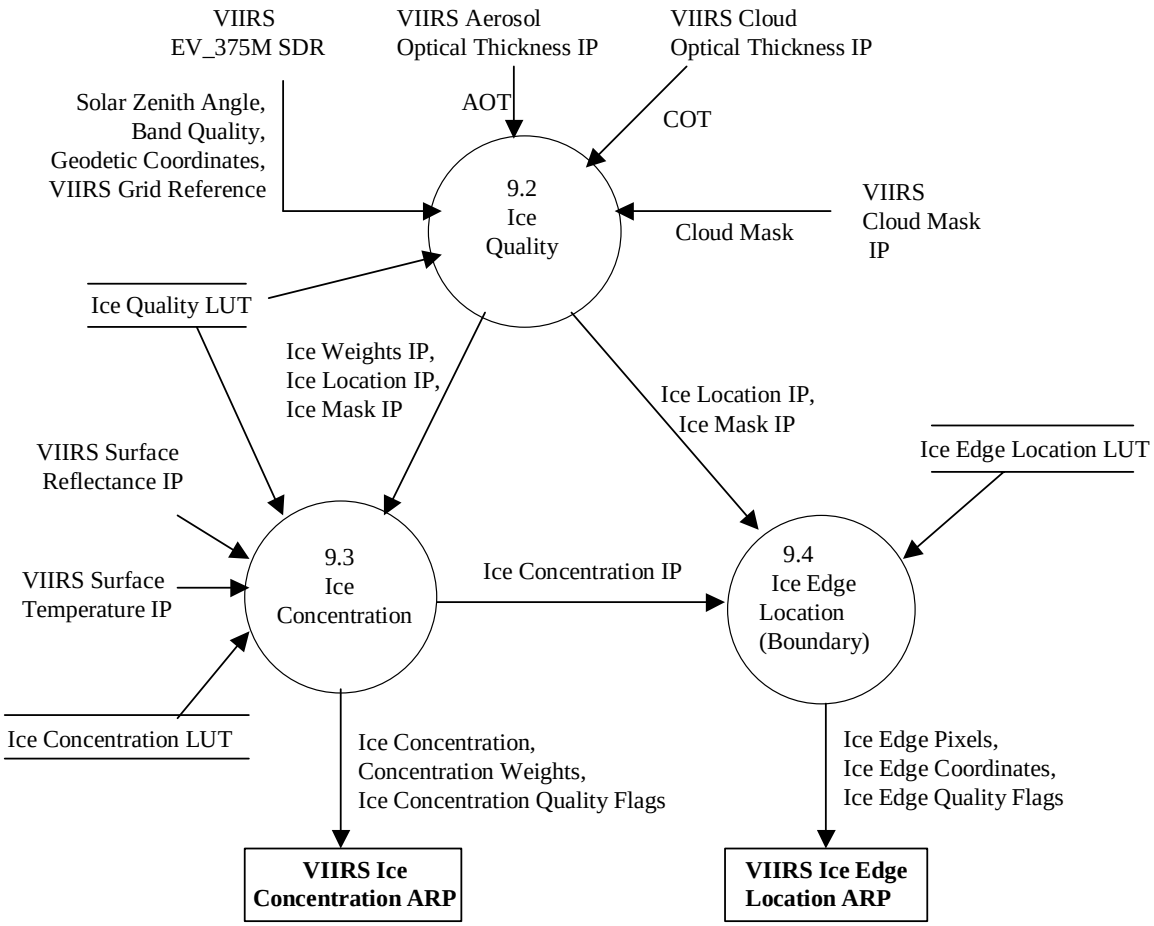

Figure 34. Process flow for the Imagery Sea Ice ARP algorithms.

The process flow for these three units is described in detail in *[Y2477]*. The main steps are as follows:

1) Input data, described in Section 3.5.2, is read in to the module. Pixels within the pre-specified horizontal coverage range are passed into the ice units, beginning with the Ice Quality unit.

2) The Ice Quality unit *[Y11649]* performs pixel masking and pixel weighting, using information in the VIIRS EV_375M SDR *[Y2479]*, VIIRS Aerosol Optical Thickness IP *[Y2471]*, VIIRS Cloud Optical Thickness IP *[Y2479]*, VIIRS Cloud Mask IP *[Y2412]*, and an Ice Quality LUT *[Y11649]*. The unit produces the Ice Location IP, the Ice Mask IP, and the Ice Weights IP. These are described in detail in *[Y11649]*.

3) Two surface reflectance images are passed into the Ice Concentration unit. The images, from VIIRS imagery resolution bands I1 (Visible) and I2 (NIR), are obtained from the VIIRS Surface Reflectance IP *[Y2411]*. Bad pixels are identified from quality information in the Ice Mask IP, Ice Weights IP, and Surface Reflectance IP. Ice concentration is calculated for each good pixel, using the tie point algorithm (Section 3.5.3.2.1).

4) The surface temperature image is passed into the Ice Concentration unit. The image is obtained from the VIIRS Surface Temperature IP, at imagery resolution. Bad pixels are identified from quality information in the Ice Mask IP, Ice Weights IP, and Surface Temperature IP. Ice concentration is calculated for each good pixel, using the tie point algorithm (Section 3.5.3.2.1).

5) The combined ice concentration for each pixel is calculated as the weighted mean of the individual band results. Concentration weights for each pixel are calculated as the sum of the individual band weights. The band weights are obtained from the Ice Weights IP. Ice concentration, concentration weights, and quality flags for each imagery resolution pixel are written to the VIIRS Ice Concentration ARP.

6) The ice concentration is passed into the Ice Edge Location unit. Pixels with no concentration result are masked. The ice edge location algorithm tags each pixel as edge or no edge, and computes edge location coordinates from the coordinates and concentration of each edge pixel and its neighbors. The edge/no edge binary map, edge coordinates, and quality flags are written to the VIIRS Ice Edge Location ARP.

The algorithm uses reflectance and surface temperature data obtained from IPs produced from the Daytime Visible (DV) and Long-Wave Infrared (LWIR) imagery bands to meet the threshold requirements. Performance may be enhanced by the use of the Near Infrared (NIR) imagery resolution band at 0.865 μm. The relative weight assigned to the DV and NIR bands shall be determined by initialization and validation (c.f. Section 3.5.6).

3.5.2 Algorithm Input

3.5.2.1 VIIRS Data

An automated algorithm will retrieve the sea ice concentration from the processed imagery. The input VIIRS data will be in the form of two-dimensional pixelized images of surface temperature, visible surface reflectance, and NIR surface reflectance. A summary of VIIRS bands is presented in Table14. The 0.64 and 11.45 µm imagery bands are sufficient to meet SRD requirements with margin. The 0.865 µm imagery-assist band provides extra margin.

Table 14. Imagery (Sea Ice Data) – Input Data Summary

λ (µm)	Δλ(µm)	GSD (m) at Nadir (Track x Scan)	HCS (m) at Nadir (Track x Scan)	GSD (m) at Edge of Scan (Track x Scan)	HCS (m) at Edge of Scan (Track x Scan)
0.64	0.080	371 x 131	371 x 393	800 x 800	800 x 800
0.865	0.039	371 x 131	371 x 393	800 x 800	800 x 800
11.45	1.90	371 x 131	371 x 393	800 x 800	800 x 800

The VIIRS data presented in Table 15 are required input to the algorithm processing code.

Table 15. VIIRS data for the Imagery (Sea Ice Data) products

Input Data	Source of Data	Reference
Instrument (Band) Quality	VIIRS SDR	*[Y2479]*
Geodetic Coordinates	VIIRS SDR	*[Y2479], [Y3258]*
Solar/Sensor Angles	VIIRS SDR	*[Y2479]*
Aerosol Optical Thickness (AOT)	Aerosol Optical Thickness IP	*[Y2471], [Y3277]*
Cloud Optical Thickness (COT)	Cloud Optical Thickness IP	*[Y2472], [Y3278]*
Visible Surface Reflectance	VIIRS Surface Reflectance IP	*[Y2411]*
Near IR Surface Reflectance	VIIRS Surface Reflectance IP	*[Y2411]*
Surface Temperature	VIIRS Ice Surface Temperature IP	*[Y10880]*
Cloud Mask	VIIRS Cloud Mask IP	*[Y2412]*
Land/Water Mask	VIIRS Cloud Mask IP	*[Y2412]*
Ice Quality Parameters	VIIRS Ice Quality LUT	*[Y11649]*
Ice Concentration Parameters	VIIRS Ice Concentration LUT	*[Y3235]*
Ice Edge Location Parameters	VIIRS Ice Edge Location LUT	*[Y2506]*

Instrument (Band) Quality

The VIIRS EV_375M SDR will contain quality flags for each band at imagery pixel resolution. Pixels with bad quality for a given band will be assigned zero band weight.

Geodetic Coordinates

The VIIRS EV_375M SDR will contain geodetic latitude and longitude of each imagery resolution pixel. The SDR coordinates will be used to report the latitude/longitude coordinate of each pixel in the ice concentration and binary edge/no edge map, and to derive ice edge coordinates. Geodetic coordinates will also be used to exclude pixels outside of the Horizontal Coverage range for the Sea Ice ARPs (c.f. Tables 5 and 6). This exclusion is quite useful in reducing the VIIRS system processing load, as most VIIRS granules will be outside of the range. Granule out of range flags will allow the ground system to bypass all sea ice algorithm processing for those granules.

Solar / Sensor Angles

The solar zenith angle (SZA) will be used to determine the relative weight of the reflectance-based and temperature-based retrievals. Each of the bands (I1, I2, and I5) will have pixel weights. Bands I1 and I2 will be progressively de-weighted as the SZA increases, providing a seamless transition across the terminator. The weighting function will be determined by pre-launch validation, as part of the initialization plan, and will be adjusted off-line by post-launch validation. The weighting function will be obtained from the Ice Quality LUT. Solar/sensor angles may also be used to apply a directional reflectance (BRDF) quality flag, if warranted by pre-launch or post-launch validation. We do not expect BRDF to be a significant error source, as the algorithm uses a local search window to characterize the ice reflectance (c.f. Section 3.5.3.2.1). Within a local search window, BRDF variations should be negligible.

Aerosol Optical Thickness

Aerosol optical thickness (AOT) is obtained at moderate pixel resolution from the Aerosol Optical Thickness IP. It is used in the Ice Quality process to derive pixel quality and pixel weight.

Cloud Optical Thickness

Cloud optical thickness (COT) is obtained at moderate pixel resolution from the Aerosol Optical Thickness IP. It is used in the Ice Quality process to derive pixel quality and pixel weight, as a switchable alternative to the Cloud Mask.

Surface Reflectance

Discrimination of ice from open water can be made on the basis of their reflectance spectra. The VIIRS Surface Reflectance algorithm *[Y2411]* will supply a Surface Reflectance IP for the I1(Visible) and I2 (NIR) bands used by the algorithm. Models of surface reflectance error are used in our error analysis (c.f. Section 3.5.4.2).

Surface Temperature

Surface temperature is needed for ice concentration retrieval at night, and is often useful for daytime retrievals.

The VIIRS Surface Temperature IP algorithm *[Y2405]* will determine the surface temperature for each imaged pixel, which will be supplied as a Surface Temperature IP *[Y10880]*. A model of surface temperature error is used in our error analysis (c.f. Section 3.5.4.2).

Cloud Mask

The VIIRS cloud mask *[Y2412]* is expected to derive a status of confident clear / probably clear / probably cloudy / confident cloudy for each pixel, building on MODIS cloud mask heritage (Ackerman *et al.*, 1997). Pixels classified as “cloudy” will be excluded from further processing. Pixels classified as “probably cloudy” are also expected to be excluded. This determination must depend on an assessment of the cloud mask performance, particularly over snow and ice surfaces. Pixels classified as “probably clear” will be processed. For these pixels, the pixel weight will be reduced by a factor obtained from the Ice Quality LUT, and a pixel quality flag will be written to the output ARP. Pixels classified as “confident clear” will be processed with no weight reduction. It is anticipated that the cloud mask will also flag pixels that are shadowed by clouds. In that case, a cloud shadow weight reduction factor will be assigned to those pixels and a shadow quality flag will be written to the ARP. Ice edges are often associated with cloud edges, increasing the critical need for effective cloud masking. The cloud mask will also supply thin cirrus, sun glint, and active fire flags, which our algorithm will use to assign pixel weight and pixel quality to the data.

Land / Water Mask

Imagery sea ice data will be reported for ocean pixels. Land pixels and pixels outside of the Horizontal Coverage range will be excluded from further processing. Coastline pixel weights will be reduced by a factor obtained from the Ice Quality LUT and reported with a quality flag. Information on Land/Ocean/Inland Water/Coastline status will be obtained from the Cloud mask IP *[Y2412]*, using the best quality land/water map available.

Ice Quality Parameters

A set of input parameters will be obtained from a pre-set VIIRS Ice Quality LUT. The parameters include ranges for sea ice and fresh water ice horizontal coverage. Pixels outside of the horizontal coverage range will be de-weighted. The parameters also include a switch

determining whether to use the Cloud Mask IP or the Cloud Optical Thickness IP for cloud masking, default relative weights for the I1, I2, and I5 bands, and weight reduction factors for various types of clouds, AOT, and SZA. The values of these parameters will be determined by initialization and validation activities (Section 3.6). A detailed description of the parameters can be found in *[Y11649]*.

Ice Concentration Parameters

A set of input parameters will be obtained from a VIIRS Ice Concentration LUT. These parameters direct the implementation of the ice concentration algorithm (Section 3.5.3.2.1) in the Ice Concentration software unit. They include search window pixel size, ice/water thresholds, and histogram bin sizes. The values of these parameters will be determined by initialization and validation activities (Section 3.6). A detailed description of the parameters can be found in *[Y3235]*.

Ice Edge Location Parameters

A set of input parameters will be obtained from a VIIRS Ice Edge Location LUT. These parameters direct the implementation of the ice edge location algorithm (Section 3.5.3.2.2) in the Ice Edge Location software unit. Primarily, they include parameters used to determine spatial smoothing scales appropriate for the diffuseness of the ice edge in a given vicinity. The values of these parameters will be determined by initialization and validation activities (Section 3.6). A detailed description of the parameters can be found in *[Y2506]*.

3.5.2.2 Non-VIIRS Data

The algorithms for Imagery (Sea Ice Data) require no ancillary data from outside of the VIIRS system.

3.5.3 Theoretical Description of the Retrieval

In the following sections, the mathematical background of the processes outlined in Section 3.5.1 is described.

3.5.3.1 Physics of the Problem

Ice reflectance

Remote sensing and *in situ* studies of sea ice are relatively widespread and are of significant potential benefit. The wide range in spectral albedo observed in sea ice of various types and thickness is a well-established characteristic of sea ice.

Spectral reflectance curves differ for different ice type. Each ice type has its own characteristic spectral signature. Spectral albedo of sea ice at various bands undergoes significant changes depending upon ice thickness, structure, and the state of the ice surface.

Reflectance from ice surfaces differs from snow reflectance because the ice consists of sheets rather than grains. Clear ice slabs are highly transmitting (Bolsenga, 1983). Reflectance occurs by scattering from impurities, such as brine pockets and air bubbles. Therefore, the reflectance observed from natural ice surfaces is highly variable, depending on the condition of impurities for a given ice sheet. Given the wide variety of ice conditions in nature, ice reflectance is not as well determined as snow reflectance. Snow reflectance is amenable to the Mie scattering theory (Warren, 1982). In contrast, studies of ice reflectance tend to be empirical.

One well-established characteristic of sea ice is the wide range in albedos observed in first-year ice of various types and thickness (Grenfell and Maykutt, 1977; Grenfell and Perovich, 1984). This characteristic is an important limiting factor in reflectance-based retrieval of ice concentration in the absence of snow cover (Massom and Comiso, 1994). Our search window technique (Section 3.3.5.2.1) handles this problem by characterizing the local ice reflectance empirically.

Visible and NIR reflectance is a useful ice/water discriminator, as water reflectance in this spectral range is lower than the reflectance from all but the thinnest ice surfaces.

Snow reflectance

The reflectance characteristics of sea ice surfaces are influenced by accumulated snow cover. Pure snow is a distinctive target across a part of the solar spectrum. It is among the brightest of natural substances in the visible and near-infrared part of the spectrum, but it is also often the darkest in the shortwave infrared (Dozier, 1989). The spectral albedo of snow depends on wavelength, and this dependency is controlled by the imaginary part *(k)* of the complex refractive index. This reaches a minimum at a wavelength of about 0.46 microns, and increases by a factor of 10^6 - 10^7 as wavelength increases out to 2.5 microns (Warren, 1982; Dozier, 1989). Light transmission decays exponentially in snow across a distance (d) as $\exp(-4\pi kd/\lambda)$. The *e*-folding distance for snow (the distance over which transmittance is reduced to 1/e) decreases from more than 20 m in the 0.4 – 0.5 micron range to less than 1 mm at 1.6 microns.

Light in snow is scattered primarily by refraction through, not reflection from, the ice grains. Photons are scattered at the grain surfaces, but absorbed while traversing the grain interiors. Only about 3 percent of the light scattered by an ice grain is reflected from the external surface. Nearly 89 percent is refracted through the grain, and 8 percent is scattered after internal reflections (Bohren and Barkstrom, 1974). Because ice is so transparent to visible radiation, snow reflectance is insensitive to grain size in bands below 0.7 microns, but sensitive to absorbing impurities in the snow (Wiscombe and Warren, 1980; Grenfell *et al.*, 1981). Because absorption by ice is much stronger in bands above 1.4 microns, reflectance at these wavelengths is insensitive to absorbing impurities, but sensitive to grain size. Absorbing particulates affect snow reflectance out to 0.9 microns (Grenfell *et al.*, 1981; Warren and Wiscombe, 1980), so the 0.86 micron band is sensitive to both absorbing impurities and grain size. All aforementioned values in this paragraph are determined from geometric optics for a sphere.

The spectral signature of snow is unique among common substances. Clouds and snow are both bright across the visible and near-infrared region, but clouds are much brighter than snow in the

shortwave infrared. This is because the smaller size of the scatterers in clouds decreases the probability of absorption in this spectral region where ice and water are moderately absorptive (Crane and Anderson, 1984; Dozier, 1984, 1989). Conversely, bodies of open water are dark at all wavelengths.

Visible and NIR reflectance is a useful ice/water discriminator when there is snow cover on the ice, as water reflectance in this spectral range is lower than snow reflectance.

The physical basis of snow reflectance is also discussed in the VIIRS Snow Cover/Depth ATBD *[Y2401]*.

Surface temperature

During a great part of the seasonal cycle, infrared bands will be the only available information to retrieve ice fraction. Infrared radiance allows us to calculate surface temperature.

Ice surface temperature is a good indicator of ice state for ice with thickness less than 1 meter. The surface temperature varies in a large range of magnitude depending on the stage of ice development or ice age (thickness). Thus, surface temperature is an indicator of ice age.

Changes in sea ice surface temperature are governed by the joint influence of vertical heat fluxes of different origin. The intensity of turbulent exchange by heat between the atmosphere and underlying ice surface, as well as the surface balance of long-wave radiation, directly depend on ice surface temperature. Vertical heat flux through ice cover is an explicit function of the vertical ice temperature profile, which depends on ice surface temperature. Thus, all main components of heat exchange between the atmosphere and the underlying ice surface (except short-wave radiation fluxes) are explicit functions of ice surface temperature.

In wintertime, heat flux between the atmosphere and ice is compensated by ice growth at the underside of the ice. There are no vertical changes in heat flux at the boundary between air and ice surface. At the same time, many components of heat flux depend on ice surface temperature. Therefore, conditions of conservation of vertical heat flux at the surface can be fulfilled only if ice surface temperature is adjusted to varying influencing environmental conditions.

Ice thickness is the main factor determining vertical heat flux through the ice under specified atmospheric conditions. Thus, a general conclusion about the relation between ice surface temperature and thermodynamic processes in ice cover and atmospheric boundary layer can be formulated. Ice surface temperature is determined by the processes of vertical heat exchange and is a distinctive indicator of ice thickness.

Surface temperature is a useful ice/water discriminator, as water temperature is higher than the temperature of all but the thinnest ice surfaces.

Physical Hypotheses

A. Both surface temperature and reflectance measured on the basis of satellite data vary in a large range of magnitude depending on ice fraction and ice age. Thus, surface temperature and reflectance are a valuable source of information on ice fraction and age, as the surface temperature and reflectance of a mixed ice/water pixel will depend on ice fraction as well as ice type. To separate the influence of ice fraction and ice type, we need to use an additional assumption about these two influencing parameters.

   Our approach is based on a consideration of processes forming ice distribution. Spatial changes in the predominant ice type (age) and its properties are governed by freezing and melting and can be considered as smooth. This hypothesis, which is certainly correct in most cases, is used to develop the algorithm of ice concentration retrieval.

B. Sea ice cover in polar regions consists of different floating ice forms (ice floe sizes). The sizes of ice floes depend upon season and region, decreasing during melting. A predominant ice floe size also decreases with decrease in ice concentration. But even in the summertime in the areas of open ice, at least 25% of ice floes have an average diameter greater than 500 m. In addition, ice floes of smaller size tend to gather in belts or spots of very close ice. As a result, we can state that in almost all cases, data of satellite observations even for relatively small areas of ocean surface will include pure pixels corresponding to ice.

   Our approach takes advantage of the overwhelming probability that an ice scene will contain pure ice pixels in a region localized near any pixel that contains some ice. In that case, the condition of the predominant ice type in the area under consideration can be approximated as the reflectance (or temperature) peak of the distribution (histogram) of reflectance (or temperature). Our approach adopts the derived condition of the predominant ice type as the ice tie point for a given pixel.

C. Tie point analysis determines the fraction of ice. The tie point analysis is based on the assumption that the spectral fraction of ice is equal to the horizontal fraction of the pixel covered by ice. The ice tie point is reflectance (or temperature) of ice in various stages of development. These ice tie points are not predetermined but vary in a large range depending on time and space. The tie points are scene specific and calculated by an automated algorithm, promising global operational capability.

D. Ice concentration is derived independently from three bands (visible reflectance from the DV band, near IR reflectance form the NIR band, and temperature from the LWIR band). We use the reflectance tie points if the SZA is smaller than a threshold value. We use the temperature tie point if it is colder than a threshold value. If all tie points are useful, we calculate a weighted average ice fraction. The relative weights of the three bands are determined automatically for each pixel from the conditions of a specific scene. Optimized band weights reduce error and provide a seamless day/night transition.

3.5.3.2 Mathematical Description of the Sea Ice Algorithms

3.5.3.2.1 Ice Concentration from Tie Points

Under conditions where there is a predominant ice type in a local area, ice fraction for each imaged pixel can be retrieved by the direct application of a tie point method. The tie point is a special case of spectral mixture analysis, restricted to two endmembers. The endmember signatures are derived from identifying pure pixels in the scene.

The ice fraction for a mixed pixel is:

$$f(p) = (b_p - b_{water}) / (b_{ice} - b_{water}) \qquad (3.5.3.2.1.1)$$

where: *f(p) is the calculated sea ice fraction*

b_{ice} *is the brightness value of a pure ice pixel*

b_{water} *is the brightness value of a pure water pixel*

b_p *is the brightness value of the pixel*

Our algorithm acquires three independent brightness values for each pixel. These are a visible reflectance, a near IR reflectance, and a temperature.

To take advantage of all of the available information, our algorithm generalizes the tie-point equation to three dimensions. We assume that the locus of equal ice fraction in multi-dimensional space corresponds to planes perpendicular to the line connecting ice and water tie points. In that case:

$$f(p) = \Sigma_j (b_{jice} - b_{jwater})(b_{jp} - b_{jwater}) \ / \ \Sigma_j (b_{jice} - b_{jwater})^2 \qquad (3.5.3.2.1.2)$$

where: *f(p) is the calculated ice fraction*

b_{jice} *is the jth brightness value of a pure ice pixel*

b_{jwater} *is the jth brightness value of a pure water pixel*

b_{jp} *is the jth brightness value of the pixel*

and the brightness values in Equation 3.5.3.2.1.2 have been normalized to their root mean square deviations on the scene. In that case, equation 3.5.3.2.1.2 is equivalent to:

$$f(p) = (\Sigma_j (w_j)(b_{jp} - b_{jwater}) / (b_{jice} - b_{jwater})) / \ \Sigma_j w_j \qquad (3.5.3.2.1.3)$$

or:

$$f(p) = \Sigma_j (w_j \; f_j(p)) / \; \Sigma_j \, w_j \qquad (3.5.3.2.1.4)$$

where: *$f(p)$ is the calculated ice fraction*

w_j is the relative weight in band j

b_{jice} is the jth brightness value of a pure ice pixel

b_{jwater} is the jth brightness value of a pure water pixel

b_{jp} is the jth brightness value of the pixel

$f_j(p)$ is the ice fraction calculated from band j

and: $$w_j = E_j \, (b_{jice} - b_{jwater})^2 \qquad (3.5.3.2.1.5)$$

We see that the relative weights of the bands scale as the square of the difference in ice and water tie points relative to the RMS deviation of the scene. The factor E_j, included to allow for other band-dependent factors, is obtained from the Ice Weights IP. This IP, produced by the Ice Quality process *[Y11649]*, contains pixel weights for each band, determined by clouds, SZA, AOT, etc.

Our approach is to calculate ice fraction for each band, according to equation 3.5.3.2.1.1, and derive a band-weighted ice fraction, according to equation 3.5.3.2.1.4, with band weights determined by equation 3.5.3.2.1.5.

Errors in deriving b_{ice} *and* b_{water} have been an obstacle to achieving global operational ice concentration retrieval. Our algorithm greatly reduces these errors by deriving tie points from the scene.

An ice/water threshold is derived to select the pixels used for the water distribution for scenes containing open water. We assume that a scene-corrected threshold corresponds to the minimum probability of reflectance and/or temperature located between values associated with water and ice. Location of the minimum is found by use of a sliding integral taken over the probability density of the parameter (reflectance or temperature). The range of measured parameter values is divided into a specified number of histogram bins. The number is obtained from the Ice Concentration LUT. The histogram of the distribution for the scene is computed. The histogram is smoothed by a running boxcar filter of specified width, producing a sliding integral of the parameter distribution. The width of the filter is also obtained from the Ice Concentration LUT. The lowest value of the sliding integral is adopted as the ice/water threshold.

The water tie point is selected as the maximum in probability density distribution corresponding to the maximum of the sliding integral over water reflectance (temperature). We analyze water characteristics only in the immediate vicinity of the ice zone. It allows us to improve the accuracy of water tie point determination as it eliminates water characteristics for areas far away from ice cover. Those characteristics can differ from open water properties in the vicinity of the ice zone.

A scene-corrected ice threshold is derived as the first minimum of the sliding integral of the parameter distribution. The water tie point is selected as the maximum of the sliding integral below the ice/water threshold. Figure 35 illustrates the process.

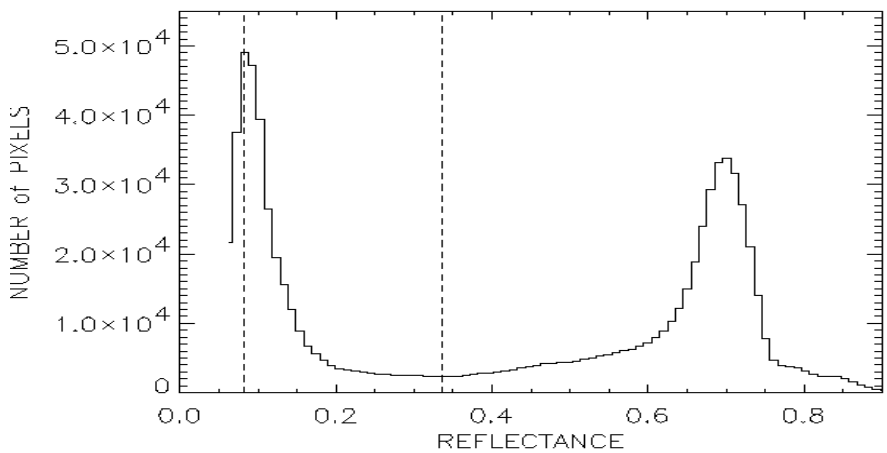

Figure 35. Distribution of 640 nm reflectance for an ice/water scene. The ice/water threshold reflectance (0.336) and the water tie point (0.083) are indicated.

For every imaged pixel, ice reflectance and/or surface temperature corresponding to an ice tie point (pure pixel) is calculated as the most probable reflectance and/or ice surface temperature in the vicinity of the pixel under consideration.

The ice tie point is derived locally for each pixel whose parameter value is on the ice side of the ice/water threshold. The distribution of parameter values in a local search window is acquired. The ice tie point is selected as the maximum value for a sliding integral of the local parameter distribution. Figure 36 illustrates the process.

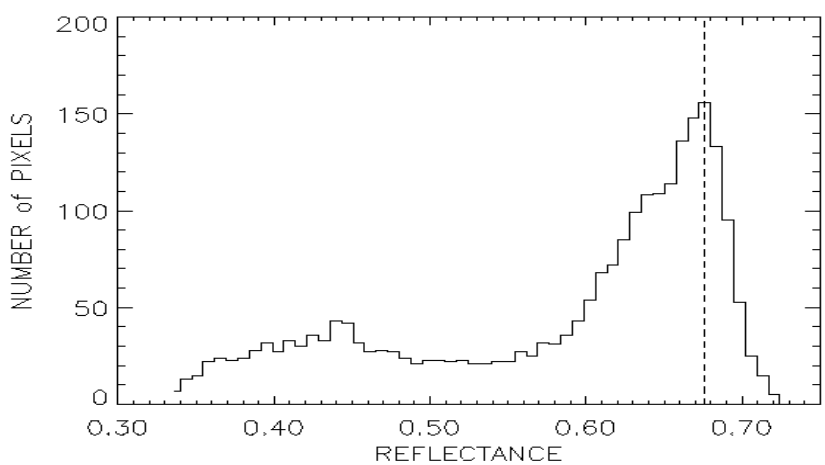

Figure 36. Distribution of 640 nm reflectance for a local search window centered on a single pixel of the scene.

For each pixel, a search window is used to establish the ice tie points from the local distribution of reflectance and/or surface temperature at the spatial scale of the window. The ice tie point is selected as the maximum value for a sliding integral of the local parameter distribution within the search window. For the example presented in Figure 36, the ice tie point for the pixel is equal to 0.676. The accuracy of the ice tie point selection depends on the size of the local search window, which is obtained from the Ice Concentration LUT. A larger search window will contain more pixels, thereby increasing the statistical robustness of the distribution. This is achieved at the expense of greater intrinsic variation in the condition of the ice within the search window, leading to an increased bias between the true ice condition of the central pixel and the derived ice condition of the search window. The optimum search window size will balance these competing effects to minimize error. Optimization of the search window size, which will therefore improve algorithm performance, is a primary goal of algorithm initialization and validation.

Having selected the ice and water tie points appropriate to a given pixel, the algorithm applies equation 3.5.3.2.1.1 to retrieve the ice fraction for each pixel. Ice concentration is reported as the ice fraction of each pixel. Concentrations less than 0.0 are set to 0.0. Concentrations greater than 1.0 are set to 1.0.

3.5.3.2.2 Ice Edge Location

Gridded ice fraction at imagery resolution is used to calculate ice edge location. A pixel is tagged as a possible ice edge pixel if one of the following conditions are met:

(1) It has ice concentration greater than 0.1 and at least one neighboring pixel has ice concentration less than 0.1

(2) It has ice concentration less than 0.1 and at least one neighboring pixel has ice concentration greater than 0.1

The set of tagged pixels are examined to derive a binary edge/no edge map and ice edge coordinates. Each neighboring pair of tagged pixels will produce an edge coordinate and an edge pixel. The edge pixel will be that member of the pair whose concentration is closer to the 0.1 edge value. The edge latitude/longitude coordinate is derived by a weighted linear interpolation of the pixel coordinates:

$$Lat = (Lat)_2 + (((Lat)_1 - (Lat)_2) \times (0.1 - C_2) / (C_1 - C_2)) \qquad (3.5.3.2.2.1)$$

$$Lon = (Lon)_2 + (((Lon)_1 - (Lon)_2) \times (0.1 - C_2) / (C_1 - C_2)) \qquad (3.5.3.2.2.2)$$

where : $C_{1,2}$ are the ice concentrations for pixels 1 and 2

and the coordinates apply to the pixel centers, as supplied by the geo-location algorithm *[Y3258]*.

Our algorithm also provides the option to retrieve the location of a diffusive ice edge by smoothing the ice concentration on an appropriate spatial scale. Different applications require different spatial scales of smoothing. Our algorithm allows for a flexible choice of smoothing kernel. Our baseline approach is to determine the spatial scale of smoothing on the scene, using

the autocorrelation of the ice concentration distribution. The granule is sub-divided into a set of granule sub-regions. The size of the sub-regions is determined from a parameter in the Ice Edge Location LUT. For each sub-region, a spatial smoothing scale is determined from the first zero-crossing pixel offset of the autocorrelation function (ACF) of the ice concentration image. A vector mapping the zero-crossing pixel offset to the spatial smoothing scale (in pixels) is obtained from the Ice Edge Location LUT. Determination of sub-region size and the mapping vector is a primary goal of algorithm initialization and validation. The spatial smoothing kernel is currently a boxcar filter with the derived pixel size. For example, the smallest kernel would be a 3x3 matrix with each element = 1/9. Future development could include the determination of a more structured filter, with pixels closer to the central pixel having greater weight.

3.5.3.3 Archived Algorithm Output

Ice concentration will be archived at imagery pixel resolution. It will be stored as a field in the Ice Concentration ARP HDF file, along with associated quality flags, as described in the Ice Concentration Unit Level Detailed Design document *[Y3235]*.

Ice edge location will be archived as a binary edge/no edge map, at imagery pixel resolution, and as a set of latitude/longitude coordinates. Each will be stored as a field in the Ice Edge Location ARP HDF file, along with associated quality flags, as described in the Ice Edge Location Unit Level Detailed Design document *[Y2506]*.

3.5.3.4 Algorithm Watch List

Following its review of the Version 3 ATBDs, the VIIRS Operational Algorithm Team (VOAT) produced a list of items requiring attention. One of these, item 8, directly affects the Imagery Sea Ice ARPs:

> 8) *IMPACT OF CLOUD MASK – "Impact of Cloud Mask (clear, cloudy, aerosol distinction) for EDR production and performance."*

In our response to the watch list, we stated that "Raytheon agrees that the interplay between the Cloud mask and the rest of the VIIRS system is a central issue leading into CDR. Within the scope of Phase II, Raytheon will further refine the definitions of 'probably cloudy' and 'probably clear'."

We recognize that effective cloud masking is essential to the production of an operational sea ice product from Vis-IR data. We have addressed this matter in Sections 3.5.4.4 and 4.2. We are sensitive to the concern in the user community that very aggressive cloud masking can result in the unnecessary exclusion of useful surface data observable through thin clouds. We have been working with the VIIRS Cloud IPT to provide a Cloud Mask IP that will enable us to process and report the Imagery Sea Ice ARPs for surfaces observable through thin cloud cover. Our plan is to identify three regions in the "Cloud Optical Thickness" phase space. In the "Green" region (small τ), the ARPs will be reported to meet or exceed specification. In the "Red" region (large τ), the pixel will be masked and the ARPs will not be reported. We plan to define a "Yellow" transition

region, where the ARPs will be reported with a quality warning attached. In this region, we expect the algorithm performance to be degraded below specification, but still to provide useful information. Pixels in the "Yellow" region will have their weight reduced by a factor obtained from the Ice Quality LUT. Weight reduction factors will be determined from initialization activity, using MODIS data, and will be refined with NPP/VIIRS data. The cloud optical thickness thresholds that identify the three regions are TBD, and will require validation with MODIS and NPP/VIIRS data. We note that it is important to mask and exclude "Red" region pixels, as our algorithm uses search windows. We have modified our algorithm design to also exclude "Yellow" region pixels from search windows, based on our hypothesis that cloud contaminated pixels add more noise than information to the ice condition distribution. We will test this hypothesis as part of our validation plan.

We will continue to work with the Cloud IPT and the VOAT to ensure that the VIIRS Cloud Mask algorithm provides a product of sufficient quality for us to meet our specification for the Imagery Sea Ice ARPs.

3.5.4 Performance of Sea Ice Data

The performance of the algorithms with respect to the VIIRS requirements and the System Specification (c.f. Tables 5 and 6) is reviewed in this section.

3.5.4.1 Stratification

During Phase I of the NPOESS project, performance was verified by analysis, modeling, and/or simulation based on the instrument design and performance characteristics and the algorithms. The analysis, modeling, and/or simulation was sufficiently extensive in scope to verify that EDR requirements are met under a broad range of conditions that are representative of those occurring in nature, including both typical and extreme conditions.

3.5.4.1.1 Ice Concentration

We identify the following stratifications for ice concentration:

1) Ice concentration "truth"

2) Ice "type"

3) Day/Night

Performance of the ice concentration algorithm is expected to depend on ice concentration "truth". A sensible stratification must then include ice concentration "truth" as a parameter. We have selected 4 ranges of ice concentration, 0.0-0.35, 0.35-0.65, 0.65-0.85, and 0.85-1.0. These ranges correspond to the following ice concentration zones: very open floating ice, open floating ice, close floating ice, very close floating ice.

Ice conditions are widely variable, depending on its stage of development. The contrast between ice and water tie points is generally larger for ice in later stages of development. Algorithm performance is very sensitive to tie point contrast. Analytically, the error in concentration derived from a tie point equation scales inversely with the tie point contrast. A sensible stratification should include ice "type" as a parameter. We have selected 2 ice types, "Young", and "First-Year or Older". Young ice is characterized by a thickness of 0.1 – 0.3 meters. We select 0.3 meters as our boundary between ice types. Our specification for ice concentration measurement uncertainty (c.f. Table 6) excludes ice with characteristic thickness less than 0.1 meter ("New Ice" and "Nilas").

We include a third stratification by type, which we call "Typical Scene", to illustrate expected performance for a typical probability of ice types.

The requirements are specified at nadir. Our stratification of sensor view angle is restricted to nadir view.

Nighttime and daytime retrievals are distinct. Daytime retrievals can use reflectance data as well as temperature data. Because thermal contrast between ice and water is smaller during the daytime, a daytime retrieval will rely more heavily on reflectance data. Nighttime retrievals, on the other hand, must rely solely on temperature data.

We have used SZA = 60 degrees in our simulations to date. Our stratification of solar zenith angle is restricted to this value. A wider range of SZAs will be simulated in the future.

We report performance estimates for a representative sample of geophysical conditions:

Case 1: Clear, Nadir, Solar Zenith Angle = 60 degrees

Case 2: Clear, Nadir, Night, Air Temperature = -5 degrees Celsius

Case 3: Clear, Nadir, Night, Air Temperature = -10 degrees Celsius

Daytime performance will depend on SZA, as surface reflectance errors increase with decreasing sunlight and increased atmospheric path length. We have modeled surface reflectance error for a solar zenith angle of 60 degrees to represent a typical solar elevation in sub-arctic regions during summertime.

Nighttime performance will depend on the surface air temperature. The thermal contrast between ice and open water increases as air temperature decreases. For an air temperature of 0 Celsius, the thermal contrast between most first year ice types and water is negligible. For an air temperature of –5 Celsius, the thermal contrast between most first year ice types and water is 3 – 4 degrees. For air temperatures colder than –10 Celsius, the thermal contrast between most first year ice types and water is greater than 8 – 10 degrees. We have selected two cases of nighttime air temperature (-5 Celsius and –10 Celsius) to illustrate the relative effect on performance. Typical nighttime air temperatures vary with latitude and season, but are usually colder than –10 Celsius in polar regions. We have found that performance at colder temperatures is similar to the performance at –10 Celsius.

3.5.4.1.2 Ice Edge Location

Ice edge location is derived directly from ice concentration. For this reason, its stratification is similar to that of ice concentration. We identify the following stratifications for the ice edge location:

1) Ice "type"

2) Sensor view angle

3) Day/Night

Note that the ice concentration "truth" is not included as a stratification, because by definition the retrieval occurs at ice edges only.

The rationales for our stratifications are identical to the ice concentration stratification rationales discussed in Section 3.5.4.1.1, with the exception of ice concentration "truth".

3.5.4.2 Stratified Performance Analysis

3.5.4.2.1 Ice Concentration

Ice Concentration is derived by a tie point equation:

$$C = (P-W) / (I-W) \qquad (3.5.4.2.1.1)$$

Where: P = measured parameter (either surface temperature or surface reflectance)

W = water parameter value (tie point)

I = ice parameter value (tie point)

Errors in P, W, and I contribute to the measurement uncertainty:

$$\sigma^2_C = (\sigma^2_P + C^2 \sigma^2_I + (1-C)^2 \sigma^2_w) / (I-W)^2 \qquad (3.5.4.2.1.2)$$

Errors in P are derived from sensor and algorithm, and are taken from the stratified performances of the Surface Reflectance and Surface Temperature IPs. These are documented in the VIIRS System Specification *[SS 154640-001]* and in the VIIRS Imagery Technical Interchange Meeting (TIM) *[Y4963]*. Precision and accuracy errors were applied to our test data sets.

I and W are derived from a scene, using search windows. Errors in I and W, caused by deviations of the derived ice and water tie points from the "true" pixel tie points, have been an obstacle to achieving global operational ice concentration retrieval. Our algorithm greatly reduces these errors by deriving tie points from the scene.

Our analysis of ice concentration measurement uncertainty was performed as follows:

We applied our algorithm to MODIS Airborne Simulator (MAS) scenes at a 50 meter pixel resolution. The test scenes are discussed in the VIIRS Test Data Set Specification Document. Reflectances in MAS band 3 (648 nm) and 7 (866 nm) were calculated from the TOA radiances. Brightness temperatures in MAS bands 45 (11 μm) and 46 (12 μm) were calculated from the TOA radiances. Surface temperature was computed by the Surface Temperature IP algorithm *[Y2405]*. The surface reflectances and surface temperature at 50 meter resolution were used as input data for our algorithm. The retrieved ice concentration was adopted as "truth". The 50 meter truth was aggregated to a VIIRS pixel size at nadir (8 x 8 aggregation to 0.4 km pixels) and adopted as VIIRS "true" concentration at nadir.

A model MTF with HSR = 0.4 km was then applied to the surface reflectance and surface temperature images to simulate VIIRS imagery at nadir.

We then perturbed the MTF-smeared reflectances, using our model errors for the Surface Reflectance IP in the VIIRS DV band (640 nm). The errors depend on surface reflectance truth, which is correlated with ice concentration. Accuracy and precision errors were applied. Accuracy errors include a 2% calibration bias and an aerosol optical thickness bias of 0.05. Precision errors are derived from the sensor noise. Reflectance errors were calculated for a solar zenith angle of 60 degrees. We note that the VIIRS NIR band I2 (865 nm) is also available as a performance enhancement band. The daytime performance reported here is from VIIRS DV only.

We perturbed the aggregated temperatures, using model errors for the Surface Temperature IP. Surface Temperature IP performance was derived as follows:

The split-window Ice Surface Temperature algorithm *[Y2405]* was applied to MAS scenes at a 50 meter pixel resolution. Brightness temperatures in MAS bands 45 (11 μm) and 46 (12 μm) were calculated from the unperturbed TOA radiances in those bands, and used as input data to the algorithm. The retrieved surface temperatures were adopted as "truth". The 50 meter truth was aggregated to VIIRS imagery pixel sizes at nadir (8 x 8 aggregation to 0.4 km pixels). The aggregated temperatures were adopted as VIIRS "truth".

The MAS TOA radiances were then aggregated to VIIRS pixel size. A proxy for the VIIRS Long-Wave Infrared (LWIR) imagery band radiance was made from the average of the band 45 and 46 radiances. The VIIRS model radiances were then perturbed by our models for sensor noise and calibration bias. A 0.5% calibration bias was applied to all radiances. Sensor noise models for VIIRS bands M15 (11 μm), M16 (12 μm), and LWIR were applied to the corresponding radiances. The perturbed radiances were converted to brightness temperature, and used as input data to the Surface Temperature IP algorithm.

Surface Temperature IP accuracy, precision, and uncertainty errors were calculated from comparison of the retrieved surface temperature to the "truth". At nadir, these errors are 0.278 K in accuracy and 0.378 K in precision.

We applied the algorithm to the perturbed VIIRS scenes to retrieve ice concentration, and computed measurement uncertainty by comparing the retrieved concentration to the "VIIRS truth". The pixel deviations between retrieved and true concentration were aggregated 2 x 2 to a

horizontal cell of 0.8 km. The aggregated deviations were sorted into the four truth stratification bins. For each bin, the RMS of the deviations was computed as the measurement uncertainty for that bin.

We applied the algorithm to the perturbed VIIRS scenes to retrieve ice concentration, and computed measurement uncertainty by comparing the retrieved concentration to the "VIIRS truth". We did this for three sea ice daytime scenes:

> A Bering Sea scene in early April (AK_74_14) from the Alaska-April 95 campaign.
>
> Two Beaufort Sea scenes in late May (ACE_65_3 and ACE_65_8) from the FIRE-ACE campaign.

And for a lake ice daytime scene:

> A Lake Superior scene in February (WIN_46_16) from the WINCE campaign).

An example of the procedure is illustrated for scene ACE_65_3 in Figure 37.

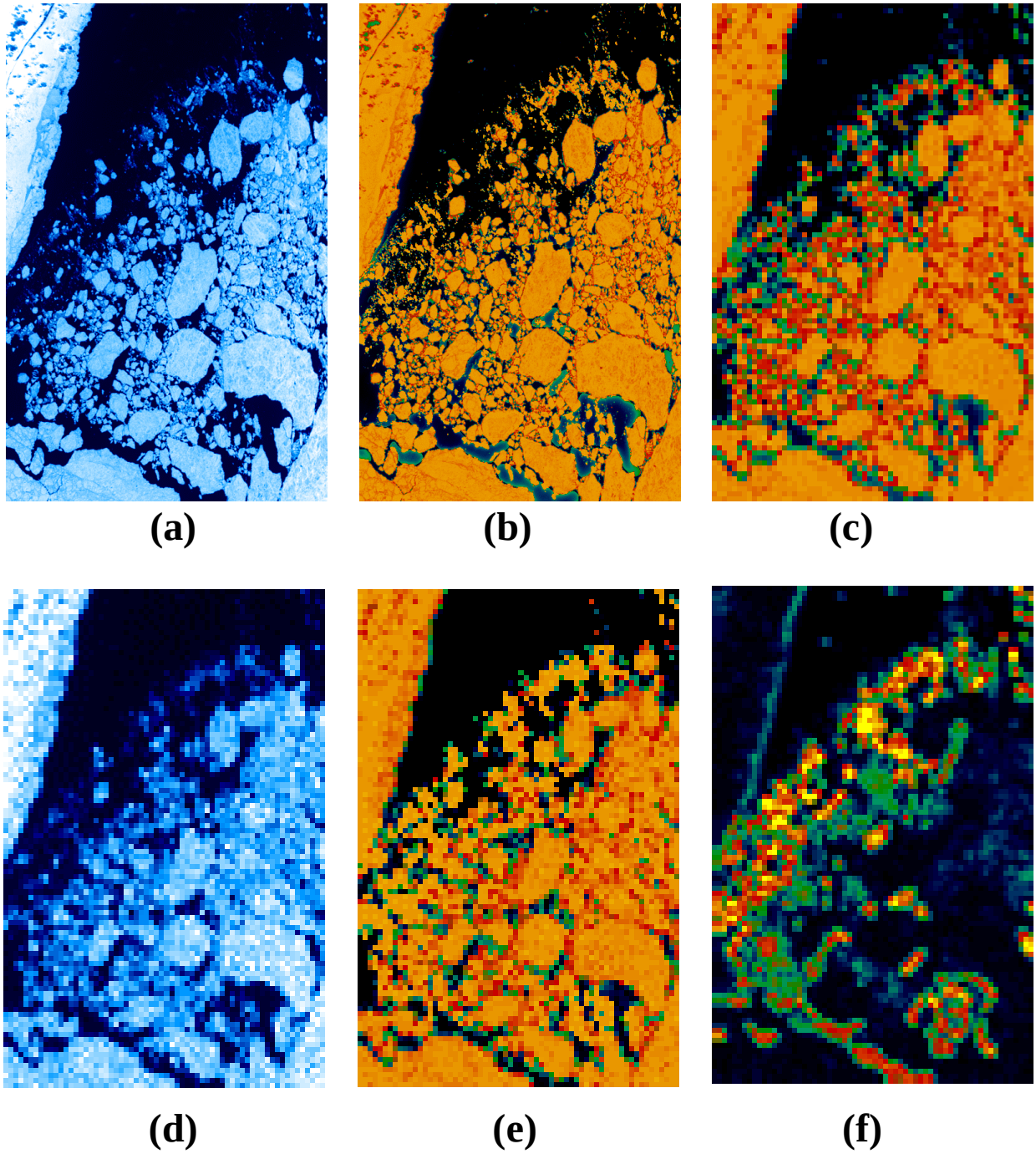

Figure 37. Illustration of the ice concentration performance analysis methodology. The scene is from the FIRE-ACE campaign of the MODIS Airborne Simulator (ACE_65_3).

The original MAS scene (a), is used as input to the ice concentration algorithm, which derives ice concentration at the 50 meter MAS resolution (b). The concentration is aggregated to the VIIRS pixel size of 0.4 km to produce VIIRS truth (c). Scene (a) is then perturbed by our model for the sensor effects to simulate expected VIIRS imagery at nadir (d). Scene (d) is used as input to the ice concentration algorithm, which derives the simulated VIIRS ice concentration (e). A comparison of result (e) with truth (c) produces an error estimate (f).

For daytime performance analysis, we use the reflectance data. For nighttime performance analysis, we use the surface temperature data, adjusted to simulate conditions when air temperature is –5 Celsius and –10 Celsius. The adjustment is necessary, because the nighttime thermal contrast between ice and water scales linearly with the thermal contrast between air and water:

$$T_W - T_I = 16.2\ H\ (\ 3.61 + 0.049\ T_W + (T_W - T_A\ ))\ /\ (1.5 + 17\ H) \qquad (3.5.4.2.1.3)$$

where: T_W = Water Temperature (Celsius)

T_I = Ice Temperature (Celsius)

T_A = Air Temperature (Celsius)

H = Ice Thickness (meters)

Equation 3.5.4.2.1.3 is derived from energy balance, and is approximately correct for ice thickness less than 1 meter and for typical winter conditions.

An illustration of the process is shown as Figure 38. The MAS scene AK_74_14 was processed to create simulated nighttime surface temperature imagery for conditions where surface air temperature = 0^0 Celsius, -5^0 Celsius, -10^0 Celsius, and -20^0 Celsius.

(a) **(b)** **(c)**

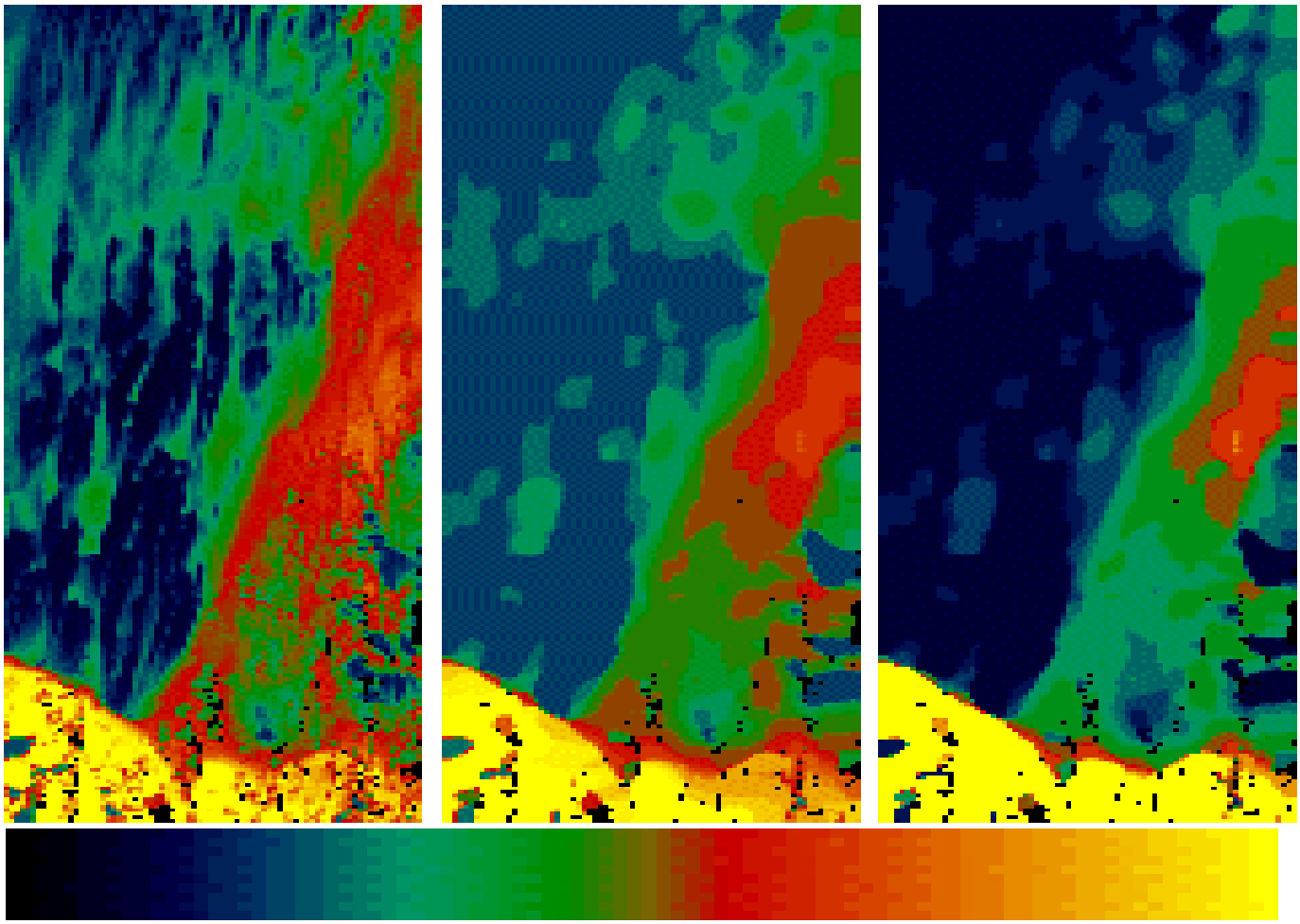

Figure 38. (a) Simulated VIIRS daytime visible band imagery of the Bering Sea scene AK_74_14. (b) Retrieved ice reflectance tie points. (c) Ice thickness, derived from the reflectance tie points.

The color table displays a reflectance range of 0.0 (blue) to 0.7 (yellow) and a thickness range of 0.0 (blue) to 0.2 meters (yellow). The ice thickness, shown in Figure 38c, is calculated from a fourth order polynomial thickness-reflectance relation, which was determined empirically by matching temperature and reflectance distributions from a number of ice scenes.

The ice temperature was then calculated from equation 3.5.4.2.1.3, for a given air temperature. The surface temperature was computed as:

$$T_S = T_I * C + T_W * (1-C) \qquad (3.5.4.2.1.4)$$

Sensor perturbations were added as a precision error of 0.378 K and an accuracy error of 0.278 K. The resulting images are illustrated in Figure 39.

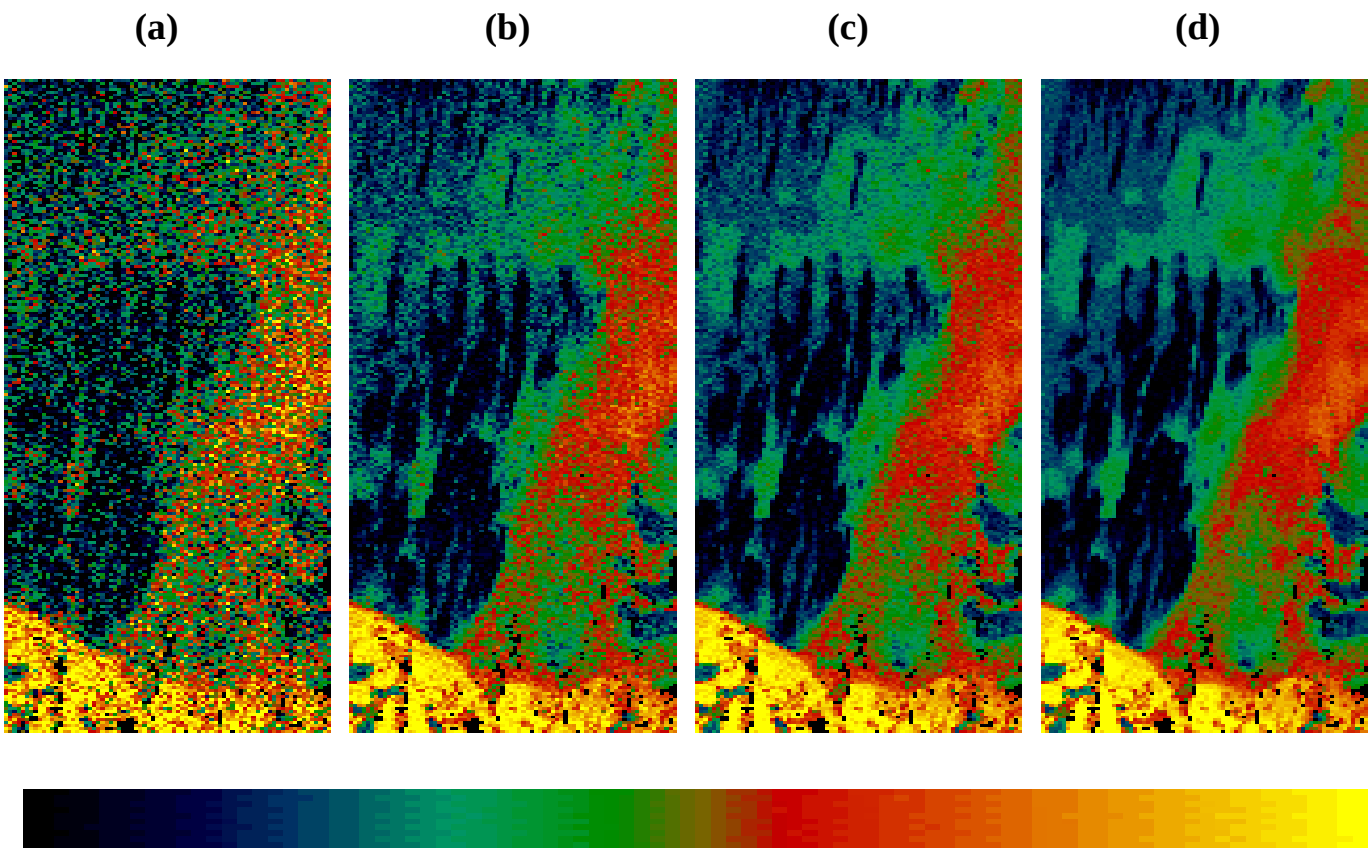

Figure 39. Simulated VIIRS nighttime imagery of the Bering Sea scene AK74_14, for air temperatures of 0 degrees Celsius (a), -5 degrees Celsius (b), -10 degrees Celsius (c), and -20 degrees Celsius (d).

Figure 39 shows how lower air temperatures increase the thermal contrast between ice and open water, resulting in smaller ice concentration measurement uncertainty. We will specify nighttime performance for the –5 and –10 cases.

Measurement uncertainties were computed from the scenes for each stratification of ice concentration truth. To assign these measurement uncertainties to an ice type bin, the mean tie point difference for each truth bin was computed. The truth / type bin error was then derived as:

$$\sigma_{mn} = \sigma_m (I\text{-}W) / (I\text{-}W)_n \qquad (3.5.4.2.1.5)$$

where: σ_{mn} = measurement uncertainty for (truth,type) bin (m,n)

σ_m = observed measurement uncertainty for truth bin (m = 1,4)

(I-W) = observed mean difference in ice/water tie points

$(I\text{-}W)_n$ = mean difference in ice/water tie points for ice type (n = 1,2)

and the scaling factor (1 / (I-W)) is based on equation 3.5.4.2.1.5. The third row of the table is derived as a weighted mean of the first two rows to represent a typical distribution of sea ice thickness.

The following tables show the errors stratified by ice concentration and ice type. The errors are for a horizontal cell of 0.8 km at nadir under clear conditions.

Table 16. Ice Concentration Measurement Uncertainty, Case 1 (Clear, Nadir, SZA=60 degrees)

Ice Type	Ice Concentration Truth			
	0.00 – 0.35	**0.35 – 0.65**	**0.65 – 0.85**	**0.85 – 1.00**
Young	.0537	.0755	.0769	.0844
First-Year/Multi-Year	.0265	.0373	.0380	.0417
Typical Scene	.0321	.0451	.0460	.0504

Table 17. Ice Concentration Measurement Uncertainty, Case 2 (Clear, Nadir, Night, Air Temperature = -5 Celsius)

Ice Type	Ice Concentration Truth			
	0.00 – 0.35	0.35 – 0.65	0.65 – 0.85	0.85 – 1.00
Young	.0301	.0593	.0548	.0574
First-Year/Multi-Year	.0232	.0457	.0423	.0443
Typical Scene	.0244	.0480	.0444	.0465

Table 18. Ice Concentration Measurement Uncertainty, Case 3 (Clear, Nadir, Night, Air Temperature = -10 Celsius)

Ice Type	Ice Concentration Truth			
	0.00 – 0.35	0.35 – 0.65	0.65 – 0.85	0.85 – 1.00
Young	.0277	.0546	.0505	.0529
First-Year/Multi-Year	.0214	.0421	.0389	.0408
Typical Scene	.0225	.0442	.0409	.0428

Typical performances are better than 0.06, compared with our specification of 0.1.

It should be noted that the (1 / (I-W)) factor in the equation for ice concentration measurement uncertainty is the primary determinant of performance. As the contrast between ice and water (I-W) decreases, errors increase inversely. Our simulations indicate that we do not attain our specification when the thermal contrast between ice and water is less than 2.2 K and the visible reflectance contrast is less than 0.14. The effect of reducing all of our system errors by a factor of 2, for example, would allow us to attain our specification for an additional range of 1.1 K in ice temperature. Performance is limited more by the geophysical conditions of the scene than by the sensor/algorithm limitations.

3.5.4.2.2 Ice Edge Location

Ice edge location is computed by linear interpolation of the measured ice concentrations between neighboring pixels. Neighboring pixel pairs are selected when their measured concentrations are on different sides of the 0.1 concentration threshold defining an ice edge.

$$Lat = ((C_1 - 0.1) \times (Lat)_2 + (0.1 - C_2) \times (Lat)_1) / (C_1 - C_2) \qquad (3.5.4.2.2.1)$$

where: C_1 = measured ice concentration for pixel with greater concentration

$(Lat)_1$ = latitude for pixel with greater concentration

C_2 = measured ice concentration for pixel with lesser concentration

$(Lat)_2$ = latitude for pixel with lesser concentration

A similar equation is applied for edge longitude.

Errors in C_1 , C_2 , $(Lat)_1$, $(Lon)_1$, $(Lat)_2$, and $(Lon)_2$ contribute to the measurement uncertainty:

$$\sigma^2_{Lat} = (A ((Lat)_1 - (Lat)_2)^2 \ \sigma^2_C) / (C_1 - C_2)^2) + \sigma^2_G \qquad (3.5.4.2.2.2)$$

where: A = factor depending on separation of C1 and C2 from 0.1.

σ_G = Geo-location error in latitude.

and $\sigma^2_C = \sigma^2_{C1} = \sigma^2_{C2}$ is assumed.

A similar equation applies to longitude error.

The combined edge location error therefore has the form:

$$\sigma^2_{Edge} = B \; P^2 \; \sigma^2_C + \sigma^2_G \qquad (3.5.4.2.2.3)$$

where: P = separation of pixel centers (km)

σ_G = Geo-location error of the pixel centers (km)

and:

$$B = A / (C_1 - C_2)^2 \qquad (3.5.4.2.2.4)$$

Our analysis of ice edge location measurement uncertainty was performed as follows:

We applied our algorithm to the same MODIS Airborne Simulator (MAS) scenes we used for ice concentrastion (c.f. Section 3.5.4.2.1) at a 50 meter pixel resolution. Reflectances in MAS bands 3 (648 nm) and 7 (866 nm) were calculated from the TOA radiances. Brightness temperatures in MAS bands 45 (11 μm) and 46 (12 μm) were calculated from the TOA radiances. Surface temperature was computed by the Ice Surface Temperature algorithm. The surface reflectances and surface temperature were used as input data for our algorithm. Our ice concentration algorithm was applied. The retrieved ice concentration was used as input data to our ice edge algorithm. The latitude/longitude coordinates for compact edges were adopted as edge location "truth".

We applied the ice concentration algorithm to the perturbed VIIRS scenes. The retrieved ice concentration was used as input data to our ice edge algorithm. We calculated the distance between each retrieved compact ice edge location and the nearest "true" ice edge, converting degrees latitude and longitude to km. The conversion accounts for the cosine of the latitude reduction in longitude degree to km conversion.

An example is shown as Figure 40.

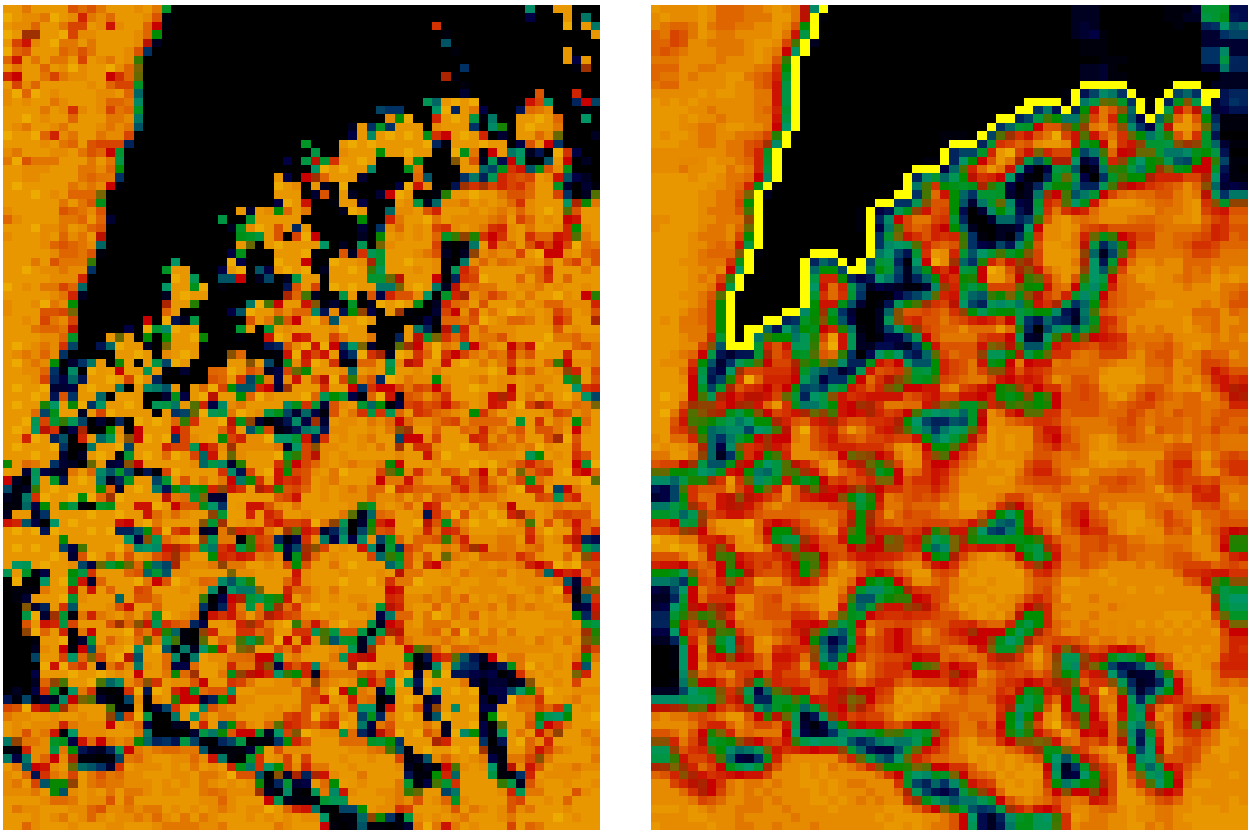

Figure 40. Illustration of ice edge location retrieval. The scene is from the FIRE-ACE campaign of the MODIS Airborne Simulator (ACE_65_3).

The ice concentration retrieval at nadir (Figure 40 left) is input to the algorithm, which produces an ice edge/no edge binary map (Figure 40 right). In the figure, the binary map is shown superimposed on the smoothed ice concentration map used by the algorithm to derive diffuse ice edge location.

The algorithm output is also a set of latitude/longitude coordinates, derived in the vicinity of the edge pixels by equations 3.5.3.2.2.1 and 3.5.3.2.2.2. Ice edge location measurement uncertainty is calculated from the deviation of the retrieved edge coordinates from the coordinates of the nearest true ice edge. The mean location error for the compact edge is 0.134 km.

The error is assumed to scale with ice concentration measurement error, from equation 3.5.4.2.2.3. We therefore scaled our derived edge location measurement errors by the corresponding ice concentration measurement uncertainties for the different ice types, as indicated in Section 3.5.4.2.1. That is, we use the observed errors in ice concentration and ice edge location to determine the B factor for the scene, which we adopt as typical for a compact ice edge.

Geo-location errors (one sigma) of 0.133 km at nadir and 0.5 km at edge of scan were then applied, following our system specification for geo-location error *[SS154640-001]*.

The following tables show the errors stratified by scan angle and ice type. These apply to compact ice edges only. Errors for diffuse ice edges will depend on the spatial scale of ice concentration gradient.

Table 19. Ice Edge Location Measurement Uncertainty (km), Case 1 (Clear, Nadir, SZA=60 degrees)

Ice Type	Scan Angle	
	Nadir	Edge of Scan
Young	0.290	0.820
First-Year/Multi-Year	0.184	0.594
Typical Scene	0.204	0.633

Table 20. Ice Edge Location Measurement Uncertainty (km), Case 2 (Clear, Nadir, Night, Air Temperature = -5 Celsius)

Ice Type	Scan Angle	
	Nadir	Edge of Scan
Young	0.240	0.719
First-Year/Multi-Year	0.204	0.639
Typical Scene	0.210	0.652

Table 21. Ice Edge Location Measurement Uncertainty (km), Case 3 (Clear, Nadir, Night, Air Temperature = -10 Celsius)

Ice Type	Scan Angle	
	Nadir	Edge of Scan
Young	0.224	0.708
First-Year/Multi-Year	0.192	0.632
Typical Scene	0.197	0.644

Typical performances at nadir are better than 0.3 km, compared with our specification of 0.4 km.

Typical performances at edge of scan are better than 0.85 km, compared with our specification of 1.0 km.

As ice edge location is derived from ice concentration, the error is similarly sensitive to the contrast between ice and water.

3.5.4.3 Error Budgets

We identify the following factors as possibly contributing to the total error budget for ice concentration:

- Tie Point errors
- Sensor noise
- Calibration
- MTF
- Band Registration

Tie Point Errors: The real variation in ice and water tie points can not be entirely accounted for with a data set of finite spatial resolution. We model these errors by comparing the retrieval of ice concentration at VIIRS resolution with the retrieval at MAS resolution. We make the reasonable assumption that the tie point errors at a resolution of 50 meters are negligible compared with the errors at a resolution of 0.4 km.

Sensor Noise: The dominant source of error in measured reflectance and/or temperature is expected to be the precision error. This error is due to sensor noise and to variations in atmospheric condition on the spatial scale of the VIIRS pixel. Our analysis shows that sensor noise will be the dominant precision error for most cases. We therefore model these errors by perturbing our "true" reflectances and temperatures by adding sensor noise to the radiances.

Calibration: Our algorithm is not expected to be sensitive to accuracy errors in reflectance and temperature, since the measured parameter, the ice tie point, and the water tie point will all be shifted by the same error. To test this hypothesis, we applied a calibration bias of 2% to the reflectance and 0.5% to the temperature.

MTF: MTF smearing of the radiances will alias real horizontal variability into errors in measured reflectance and/or temperature for a given pixel. We model these errors on our scenes by applying the sensor MTF specification to the images.

Band Registration: Band-to-band registration errors will also alias horizontal variability into measurement error. These errors only apply to a retrieval which uses more than one band. Since our performance analysis is based on single band retrieval, band registration errors were not simulated. If the retrieval were to use more than one band to enhance performance, band registration error must be considered. For now, we note that the current performance analysis can always be achieved with a single band. If a multi-band result is worse, due to the effects of band registration or non-optimum band weighting, we always have the option of using the single band.

An error budget for ice concentration is shown in Table 22.

Table 22. Error Budget for Ice Concentration

IMAGERY (ICE CONCENTRATION) Specification v5 (CDR)	Case: Measurement Uncertainty	Clear, Nadir, SZA = 60 degrees, Truth = 0.85-1.00, Typical Scene Reference
Threshold	0.1000	VIIRS SRD
Objective	0.1000	VIIRS SRD
System Specification	0.1000	Raytheon VIIRS Specification v3
System Performance	0.0504	This document
System Margin	0.0864	RSS Difference of Specification and Performance
Algorithm Performance	0.0475	This document
Sensor Performance	0.0170	This document

We identify the following factors as contributing to the total error budget for ice edge location:

- Ice Concentration
- Horizontal Spatial Resolution (HSR)
- Geo-location

Ice Concentration: The algorithm uses the ice concentration image as input data. Errors in ice concentration will result in ice edge location measurement error, as can be seen from Equation 3.5.15. We model these errors by comparing ice edge location retrievals from "true" ice concentration with retrievals from ice concentration perturbed by our various error models, as described in Section 3.5.4.2.1.

Horizontal Spatial Resolution: The coarseness of the VIIRS pixel size (P in equation 3.5.15) will limit the accuracy of the interpolation of pixelized ice concentration to ice edge coordinates.

Geo-location: Errors in geo-location of the VIIRS reflectances and temperatures input to the ice concentration algorithm will propagate into error in the ice edge location derived from ice concentration.

The B factor in equation 3.5.16 is scene dependent, and depends on the compactness of the ice edge. Our errors are derived from analysis of compact edges only. The error due to non-zero P combines with the ice concentration error, so is not budgeted separately. The combined pixel resolution/ice concentration error is budgeted as "ice concentration/resolution". The error is allocated to the algorithm subsystem, as the ice concentration algorithm error is larger than the ice concentration sensor error.

Error budgets for ice edge location are shown in Tables 23 and 24.

Table 23. Error Budget for Ice Edge Location (Nadir)

IMAGERY (ICE EDGE LOCATION) Specification v5 (CDR)	Case: Measurement Uncertainty (km)	Clear, Night, Air Temperature = -5 Celsius, Nadir, Typical Scene Reference
Threshold	TBD	VIIRS SRD
Objective	TBD	VIIRS SRD
System Specification	0.400	Raytheon VIIRS Specification v3
System Performance	0.210	This document
System Margin	0.340	RSS Difference of Specification and Performance
Concentration/Resolution	0.162	This document
Geo-location	0.133	Raytheon VIIRS Specification v3

Table 24. Error Budget for Ice Edge Location (Edge of Scan)

IMAGERY (ICE EDGE LOCATION) Specification v5 (CDR)	Case: Measurement Uncertainty (km)	Clear, Night, Air Temperature = -5 Celsius, Edge of Scan, Typical Scene Reference
Threshold	TBD	VIIRS SRD
Objective	TBD	VIIRS SRD
System Specification	1.000	Raytheon VIIRS Specification v3
System Performance	0.652	This document
System Margin	0.758	RSS Difference of Specification and Performance
Concentration / Resolution	0.418	This document
Geo-location	0.500	Raytheon VIIRS Specification v3

3.5.4.4 Limits of Applicability

In this section, we discuss the conditions under which our specified performance can not be attained.

Cloudy: Imagery Sea Ice Data are required under clear conditions only, with clear defined as a cloud optical thickness less than 0.03. Our specification is for clear scenes only. The standard approach to minimize errors caused by clouds is to mask pixels where clouds are likely to be present in the radiance path. The VIIRS Cloud Mask *[Y2412]* will perform this function. Because no cloud mask is perfect, there will be some source of error caused by the effects of

unmasked clouds. Thin clouds will perturb the upwelling surface radiance by absorption and scattering, and will also be a source of reflected radiance unrelated to the surface. There will also be error due to incorrect classification of cloud contaminated pixels as clear. There will also be effects from cloud shadows. Cloud error assessment will require an analysis of cloud masking performance over ice surfaces. It is desirable to perform tests to determine the expected size of the retrieval errors under various conditions of cloud optical thickness and phase. Thin cirrus clouds are a particularly important case of cloud error, because they are particularly difficult for the cloud mask to detect over snow. These tests require the simulation of TOA radiances from snow surfaces with a variety of overlying cloud layers. In the absence of these tests, we cannot quantify the effect of clouds. The conditions under which the specification can not be attained may include a range of cloud optical thickness. The range will be determined by a balance between the increasing effect of clouds on the signal and the increasing probability of correct masking. The specification of this range has been deferred to future verification activity. It is expected that the VIIRS Cloud Mask, which will build on MODIS heritage and experience, will perform well enough to allow for effective operational retrieval of sea ice data from VIIRS.

Low Contrast Between Ice and Water Tie Points: The error in ice concentration scales inversely with the difference between the ice and water tie points. As this difference approaches a critical point, performance degrades rapidly. Our simulations indicate that we do not attain our specification for ice concentration measurement uncertainty when the thermal contrast between ice and water is less than 2.2 K and when the reflectance differences are less than 0.14. In general, we will then not attain our specification for ice edge location measurement uncertainty. This occurs under the following conditions:

Low light or nighttime during summer: The thermal contrast between ice and open water is too low during part of the summer to allow for ice concentration derivations from thermal bands. A reliance on solar reflectance bands suffers from limitations during low light conditions.

”New” ice: Temperature and reflectance contrasts are strongly dependent on ice thickness. The contrasts are generally too low for ice with a thickness less than 0.05 to 0.1 meters, depending upon local conditions. Our specification and performance result therefore excludes “New” ice.

3.5.5 Practical Considerations

3.5.5.1 Numerical Computation Considerations

Paragraph SRDV3.2.1.5.4-1 of the VIIRS SRD states the following:

> *“The scientific SDR and EDR algorithms delivered by the VIIRS contractor shall be convertible into operational code that is compatible with a 20 minute maximum processing time at either the DoD Centrals or DoD field terminals for the conversion of all pertinent RDRs into all required EDRs for the site or terminal, including those based wholly or in part on data from other sensor suites.”*

RDR here stands for Raw Data Record. This essentially means that any and all EDRs must be completely processed from VIIRS raw data, including calibration and geolocation, within 20

minutes from the time the raw data are available. This requirement is a strong reminder that VIIRS is an operational instrument.

For the Imagery EDR products, the challenges posed by the SRD time requirement are minimal. The geolocation and calibration algorithms used to produce Explicit Imagery are not computationally intensive in nature. NCC Imagery requires the use of pre-generated lookup tables that are simple and straightforward to apply, as has been demonstrated by the operational OLS product. Manual cloud ARPs are generated in real time by analysts. The sea ice ARPs do not involve any kind of iteration or inversion of physically-based models. We optimized our scheme of choosing parameters in the sliding search window. As a result of this improvement, the requirement to retrieve ice products on a global, operational basis in a 20 minute time frame places no constraints on our algorithms.

3.5.5.2 Programming and Procedural Considerations

VIIRS Phase II efforts are largely software-focused, and the methodology for this development work is based on sound and proven principles, as discussed in the VIIRS Algorithm Software Development Plan *[Y6635]*. The present maturity of the VIIRS software is detailed in the VIIRS Algorithm Software Maturity Assessment document *[Y6661]*. The maturity and remaining Phase II tasks for the algorithms themselves is summarized in the VIIRS Algorithm/Data Processing Technical Report *[Y7040]*.

Except for manual cloud analysis, all procedures are automatic, to perform in the operational environment. The Imagery EDR products are produced in an integrated software system within the VIIRS Ground Segment of the IDPS. The software is composed of a set of independent testable units. These include the Imagery Unit, which produces the Explicit Imagery and the NCC Imagery, and the Ice Quality, Ice Concentration, and Ice Edge Location Units, which produce the Sea Ice ARPs. The software designs relevant to these units are summarized in the VIIRS Context Level Software Architecture *[Y2469]*, Build SDR Module Level Software Architecture *[Y2479]*, Snow Ice Module Level Software Architecture *[Y2477]*, Imagery Unit Level Detailed Design *[Y3273]*, Ice Quality Unit Level Detailed Design *[Y11649]*, Ice Concentration Unit Level Detailed Design *[Y3235]*, and Ice Edge Location Unit Level Detailed Design *[Y2506]*. These designs will be tested at the system level as described in the most recent versions of the VIIRS Software Integration and Test Plan *[Y3236]*, Algorithm Verification and Validation Plan *[Y3237]*, and System Verification and Validation Plan *[Y3270]*. A summary of the ultimate strategy for operational application of the system of VIIRS algorithms is provided in the VIIRS Operations Concept document *[Y2468]*. The VIIRS Interface Control Document (ICD *[Y2470]*) provides more detail on the specifics of ancillary data requirements for VIIRS EDR products.

3.5.5.3 Configuration of Retrievals

The Imagery algorithms require the availability of input data from a variety of sources, including VIIRS SDRs, VIIRS IPs, and a number of LUTs. A detailed list of these sources can be found in the Build SDR Module Level Software Architecture *[Y2479]*, Snow Ice Module Level Software Architecture *[Y2477]*, Imagery Unit Level Detailed Design *[Y3273]*, Ice Quality Unit Level

Detailed Design *[Y11649]*, Ice Concentration Unit Level Detailed Design *[Y3235]*, and Ice Edge Location Unit Level Detailed Design *[Y2506]*. The imagery ice product output is needed as input ancillary data by the VIIRS Sea Ice Age/Edge Motion algorithm. The NPOESS/VIIRS processing configuration is designed to satisfy these expectations *[Y2469]*.

3.5.5.4 Quality Assessment and Diagnostics

Quality flags will be attached to each Imagery EDR product. A description of the quality flags can be found in the detailed design documents.

3.5.5.5 Exception Handling

The software is designed to handle a wide variety of processing problems, including bad and missing data and fatal errors. In the event that processing problems prevent the production of useful EDR data, error flag information will be written to the output EDR file as metadata.

3.6 ALGORITHM VALIDATION

Validation of the Imagery EDR and the Imagery Application-Related Products will be conducted as part of the VIIRS System Verification and Validation Plan *[Y3270]*.

Verification of calibration and geolocation will be conducted for the VIIRS SDRs. TOA radiances, TOA reflectances, and EBBTs in the Imagery EDR will be verified by inspection, by comparison with the equivalent fields in the VIIRS SDR. Degrading characteristics of the imagery (e.g. striping) will be checked by manual inspection. If necessary, either pre-calibration or post-calibration corrections may be applied to minimize these characteristics.

Verification that bow tie deletion has not caused a gap in coverage will be made by manual inspection of imagery obtained from the same region for different orbits. All surface features present in nadir-viewing imagery should also be present when the same region is observed at edge of scan.

Verification of NCC Imagery will be by inspection. A trained analyst viewing the terminator imagery will be able to observe whether or not a near constant contrast is preserved across the terminator.

Verification of manual cloud analysis products will be made by a comparison of the products obtained from a number of qualified analysts. The variation in the cloud cover and cloud type results obtained by the different analysts will provide a quantitative error estimate. If warranted, independent lidar measurements can be made to provide a VIIRS-independent source of “truth”.

Initialization and validation of the sea ice algorithms will be coordinated with the National Ice Center, with the purpose of assuring that the VIIRS data products can be incorporated into their strategic product.

Radiative transfer models will be applied to large solar zenith angle data to optimize the models for polar conditions. MODIS data taken at solar zenith angles greater than 70 degrees will be

studied to assist in determining the reflectance band weighting function. The limiting factor is believed to be the reliability of atmospheric correction at larger solar zenith angles. Plane parallel radiative transfer algorithms are inaccurate for angles greater than 70-75 degrees. Development of improved radiative transfer models at larger angles will allow us to relax this constraint. To solve the Radiative Transfer Equation appropriately one would have to take into account the spherical shell atmosphere geometry (Thomas and Stamnes, 1998). It is expected that "truth" can be established from *in situ* data obtained from MODIS validation campaigns.

The pre-launch plan includes sensitivity studies, analysis of simulated VIIRS data, and verification using MODIS data. Observations from AVIRIS, MAS, MODIS, GLI, and NPP/VIIRS will be used in the pre-launch phase to study the error characteristics and optimum techniques for the algorithm. It is expected that MODIS validation data will be of great value. The NPP/VIIRS will be critical in adjusting and verifying the values of the parameters in our LUTs. This process will be essential in making the sea ice algorithms operational prior to the NPOESS mission. We recommend an NPP/VIIRS validation campaign that includes *in situ* field measurements, ER-2 underflights (AVIRIS and MAS), and low level aircraft measurements at spatial resolutions as fine as 10 meters (e.g. RC-10 camera data). NPP/VIIRS data can be re-processed many times with various combinations of band weight functions and search window parameters, and resulting ice concentration and edge location can be compared to "truth" established from the auxiliary data. In this way, optimum band weight functions and search window parameters can be selected.

Our plan is designed to interface smoothly with post-launch validation activity. The availability of NPP/VIIRS data prior to the NPOESS mission will be of enormous benefit. We would propose to conduct an NPP/VIIRS validation campaign similar to the MODIS validation activity, and use it as a model for the post-launch NPOESS/VIIRS validation campaign. In this sense, post-launch validation will already have been simulated by the pre-launch validation activity. Following launch, we would substitute real VIIRS data for the pre-launch simulated data. Cross-validation with NPOESS/CMIS provide a valuable extra capability.

4.0 ASSUMPTIONS AND LIMITATIONS

4.1 ASSUMPTIONS

The following assumptions apply to the algorithms described in this document:

- The reflectivities and emissivities for materials classifications used in the VIIRS simulations represent the real world.
- An effective cloud mask over snow and ice surfaces will be available from the VIIRS Cloud Mask IP *[Y2412]*.
- Directional surface reflectance will be derived from TOA radiances as a Surface Reflectance IP, with errors as specified in the VIIRS System Specification *[SS154640-001]*.
- A Surface Temperature IP will be provided, with errors as specified in the VIIRS System Specification *[SS154640-001]*.

4.2 LIMITATIONS

The following limitations apply to the algorithms described in this document:

- The accuracy of cloud analysis in the manually generated cloud products of the Imagery EDR are limited to cloud features which can be detected by the VIIRS horizontal spatial resolution. The VIIRS design may not detect all sub-pixel clouds.
- The accuracy of manual analyses generated from simulated VIIRS imagery is limited by the analysts ability to create cloud, no cloud analyses with the Cloud Ground Truth Analysis (CGTA) software. Cloud edges represent the greatest challenge. However, experienced image interpreters agree within about 1-2 percent in total cloud, no cloud analyses of complex scenes.
- The capability to recommend TBD values for “obscured/not cloudy if the LOS extinction optical thickness is = 0.03 (TBD)” is limited by the standard profiles and atmospheric conditions available within MODTRAN 4.0. The software does not support small, incremental changes in aerosol LOS conditions, e.g., say stratospheric aerosol optical depths in the range of 0.010 to 0.050 at 0.005 increments.

Limitations applying specifically to the automated sea ice retrieval are:

- Clear conditions only. The definition of "clear" will be developed in coordination with the development of the VIIRS Cloud Mask IP *[Y2412]*. It will depend upon the capability of the cloud mask over snow and ice surfaces and upon the capability of radiative transfer modeling through thin clouds.

5.0 REFERENCES

Ackerman, S. A., K. Strabala, P. Menzel, R. Frey, C. Moeller, L. Gumley, B. Baum, C. Schaaf, and G. Riggs (1997). Discriminating Clear-Sky From Cloud With MODIS Algorithm Theoretical Basis Document (MOD35). Version 3.2

Allen, R. C., P. A. Durkee, and C. H. Wash (1990). Snow/cloud discrimination with multispectral satellite measurements. *J. Appl. Met.*, 29, 994-1004.

Bohren, C.F., and B.R. Barkstrom (1974). Theory of the optical properties of snow. J. Geophys. Res., 79, 4527-4535.

Bolsenga, S.J. (1983). Spectral reflectances of snow and fresh-water ice from 340 through 1100 nm. J. Glaciology, 29(102), 296-305.

Crane, R.G. and M.R. Anderson (1984). Satellite discrimination of snow/cloud surfaces. Intl. J. Remote Sens., 5(1), 213-223.

Dozier, J. (1984). Snow reflectance from Landsat-4 Thematic Mapper. IEEE Trans. Geosci. Remote Sens., 22(3), 323-328.

d'Entremont, R. P., Thomason, L. W. and J. T. Bunting, 1987: "Color composite image, processing for multispectral meteorological satellite data, *Proceedings of SPIE - The International Society for Optical Engineering*, pp. 96-106, Cambridge, MA.

Dozier, J. (1989). Spectral signature of alpine snow cover from the Landsat Thematic Mapper. Remote Sens. Environ., 28, 9-22.

Grenfell, T.C., and G.A. Maykutt (1977). The optical properties of ice and snow in the Arctic Basin. *J. Glaciology*, 18(80), 445-463.

Grenfell, T.C., and D.K. Perovich (1984). Spectral albedos of sea ice and incident solar irradiance in the southern Beaufort Sea. *J. Geophys.Res.*, 89(C3), 3573-3580.

Grenfell, T.C., D.K. Perovich, and J.A. Ogren (1981). Spectral albedos of an alpine snowpack. Cold Regions Sci. Technol., 4, 121-127.

Hutchison, K. D., VIIRS Risk Reduction Plan for Manually-Generated Cloud Products, Raytheon Information and Technical Systems, Version 1.0, Revision 0.1, May, 1999.

Hutchison, K. D., VIIRS Imagery Flowdown Results , EDR: Manually-Generated Cloud Products from Imagery, October, 1998.

Hutchison, K., and P. Janota, "Cloud Models Enhancement Project Phase 1 Report," The Analytic Sciences Corporation (TASC), Technical Report TR-5773-1, August, 1989.

Hutchison, K., Peterson, R., and P. Janota, "Cloud Models Enhancement Project Phase 2 Report," The Analytic Sciences Corporation (TASC) Technical Report TR-5773-2, August, 1990.

Hutchison, K. D., and J. K. Locke (1997). Snow identification through cirrus cloudy atmospheres using AVHRR daytime imagery," Geophysical Research Letters, 24, 1791-1794

Hutchison, K. D., B. J. Etherton, and P. C. Topping (1997). Validation of automated cloud top phase algorithms: distinguishing between cirrus clouds and snow in a-priori analyses of AVHRR imagery. Optical Engineering, 36, 1727-1737

IORD-I. Integrated Operational Requirements Document – NPOESS.

Liou, K-N. (1980). An Introduction to Atmospheric Radiation. Academic Press.

Mannen, J. T. (1996). Cost and Operational Benefits Requirements Analysis Report (COBRA), NPOESS Integrated Program Office, June 12, 1996.

Massom, R., and J.C. Comiso (1994). The classification of Arctic sea ice types and the determination of surface temperature using AVHRR data. *J. Geophys. Res.*, 99(C3), 5201-5218.

Planet, W.G. (ed.), (1988). Data extraction and calibration of TIROS-N/NOAA radiometers. NOAA Technical Memorandum NESS 107 – Rev. 1, Oct. 1988. 130 pp.

Scorer, R. S. (1990). Satellite as Microscope. Ellis Horwood Limited.

Thomas, G., and K. Stamnes (1998). Radiative transfer in the atmosphere and ocean. Textbook, Cambridge Atmospheric and Space Sciences Series.

Valovcin, F. R. (1978). Spectral radiance of snow and clouds in the near infrared spectral region, AFGL-TR-78-0289, Air Force Geophysics Laboratory, Hanscom AFB, MA.

Warren, S.G. (1982). Optical properties of snow. Rev. Geophys. Space Phys., 20(1), 67-89.

Warren, S.G., and W.J.Wiscombe (1980). A model for the spectral albedo of snow.II. Snow containing atmospheric aerosols, J. Atmos. Sci., 37(12), 2734-2745.

Westinghouse Electric Corp. (1993). Technical Operating Report for Block 5D-3 Operational Linescan System (OLS) OLS 17-21.

Wiscombe, W.J., and S.G. Warren (1980). A model for the spectral albedo of snow,1,pure snow. J. Atmos. Sci., 37(12), 2712-2733.